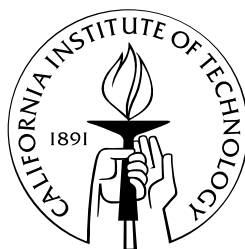


Rational Design of Zinc Phosphide Heterojunction Photovoltaics

Thesis by
Jeffrey Paul Bosco

In Partial Fulfillment of the Requirements
for the Degree of
Doctor of Philosophy



California Institute of Technology
Pasadena, California

2014

(Defended May 30, 2014)

© 2014
Jeffrey Paul Bosco
All Rights Reserved

Approval of Thesis

I have examined the candidate's thesis, and recommend its acceptance.

Date 5/30/14

Signed 
Member of Examining Committee


Date _____

Signed _____
Member of Examining Committee

Date _____

Signed _____
Member of Examining Committee

Date 5/30/14

Signed 
Member of Examining Committee

Date 5/30/14

Signed 
Member of Examining Committee

Date 5/30/14

Signed 
Chair of Examining Committee

Date _____

Signed 
Division Chair

“Look here, I have succeeded at last in fetching some gold from the sun.”

– Gustav Kirchhoff

(After his banker questioned the value of investigating gold in the Fraunhofer lines of the sun and Kirchhoff handing him over a medal he was awarded for his investigations.)

Acknowledgements

First and foremost I would like to thank my research advisor, Prof. Harry Atwater, for the tremendous amount of support he has provided during my tenure at Caltech. I first met Harry during a chemical engineering recruiting trip. He handed me a copy of *Scientific American*, blasted me with energy and excitement over the future of plasmonics (of course I had never even heard of a surface plasmon at that point), and rushed off! Little did I know that I would be working in the Atwater labs only six months later and Harry would meet me with the same energy and enthusiasm regarding the topic of zinc phosphide photovoltaics. Five years later and he is still an incredible source of support, advice, and interesting scientific ideas. Thank you Harry.

I am also indebted to the members of my thesis committee, Prof. Nathan Lewis, Prof. Kostantinos Giapis, and Prof. Richard Flagan. In particular, Nate has been an excellent scientific resource over the past couple of years. I clearly remember handing Nate a draft of my first (and in my eyes perfectly rigorous) scientific manuscript, only to have it returned a week later, so thoroughly plastered with corrections written in red ink that it looked like someone had literally ripped an artery right out of the paper. Lesson learned and my next manuscript draft came back from Nate with only a couple of scratches.

It is common that one's thesis work is built upon the previous discoveries of others. Dr. Greg Kimball initially started the zinc phosphide solar project and the knowledge he contributed to the field of earth-abundant photovoltaics has been indispensable to my work. Greg also made a great mentor, laboratory accomplice, and friend. I worked alongside of several other individuals on the Zn_3P_2 project, including Dr. Seokmin Jeon (Seokmin's STM work is featured in Chapter 3), Faisal Tajdar, and Andrew Gong. Some of this work depended heavily on the theoretical calculations made by Dr. Steve Demers and Prof. David Scanlon. David not only made a productive theoretical collaborator, but also a great late-night drinking partner at various conferences. Finally,

Dr. Steve Rozeveld of The DOW Chemical Company provided countless TEM images (and presumably countless hours of his time) of epitaxial Zn_3P_2 films for which I have received many compliments on their stunning clarity. Zn_3P_2 is also not the only “earth-abundant” solar material that the Atwater group studies, and therefore I have not been the only person burdened with the challenge of working with an unstudied semiconductor. I am thankful to have worked alongside of Samantha Wilson, Naomi Coronel, Yulia Tolstova, and Amanda Shing, who have shared many of the same trials and tribulations (and inevitable headaches) regarding the material science and device physics of novel materials.

There are a number of individuals in charge of the instruments that I used heavily during my thesis work. I know that training for and maintenance of any piece of scientific equipment is a completely thankless task. Therefore, I would like to directly acknowledge the following for their extreme patience and commitment: Joseph Beardsley (Kratos XPS), Emily Warmman (HRXRD), Bruce Brunswig (MMRC), Ryan Briggs and Stan Berkos (ellipsometer), Carissa Eisler (sputterer), John Lloyd, Cris Flowers, and Rob Corridan (e-beam evaporators), Michael Deceglie, Michael Kelzenberg (solar simulator), Hal Emmer and Chris Chen (various laboratory responsibilities). I owe a special thanks to Lise Lahourcade, who caused an abrupt increase in my productivity when she taught me how to use a RHEED gun as well as Marina Leite for introducing me to single-crystal x-ray diffraction. Of course, a laboratory functions beyond the efforts of any one individual and I owe many thanks to the collaborative nature of the entire Atwater and Lewis groups. Without their ideas and support, this thesis would not have been possible.

The funding for my thesis project came from two distinct sources: the NSF graduate research fellowship and the DOW Chemical Company. I had a number of fruitful interactions with members of The DOW Chemical Company’s solar research team. Many thanks to Dr. James Stevens, Dr. Marty DeGroot, Dr. Rebekah Feist, Dr. Robert Wright, Dr. Melissa Mushrush, and Dr.

Manish Sharma for their professional and scientific mentoring.

The social landscape of graduate school can be a difficult terrain to traverse. I am indebted to a number of individuals who have made the entire PhD process a rich experience. To my first year Chemical Engineering classmates, who quickly became a second family as we spent tireless nights in Spalding Laboratory slaving away at pages of index notation, vehemently arguing about thermodynamic systems, and imbibing our fair share of margaritas and mind erasers at Amigos. They helped me survive John Brady's four hour transport exams and the notorious ChemE qualifier and somehow made this whole process a total a blast! Thanks again, guys (and Amy!). I thank my office mates, Seyoon Kim and Nick Batara, with whom I had countless conversations about food, beer, and any number of pointless topics. There is also nothing like escaping to Santa Monica on weekend mornings to vent one's frustrations in an intense game of doubles beach volleyball. Thanks to Prof. Nick Strandewitz, Morgan Putnam, Dan Turner-Evans, Rob Usiskin and many others for being such excellent (well, at least enthusiastic) players. Whether it was camping in the deserts of Nevada, climbing the rocky switchbacks of Mount Fuji, or playing a heated game of Risk with too many glasses of wine, Vanessa Heckman and Brett Babin were always fantastic partners in crime. And, I owe many thanks to Mikhail Hanewich-Hollatz, Amanda Jee-young Mock, Luke Urban, Samantha Wilson, Dan Lin, and Naeem Hussain for being excellent close friends and maintaining my sanity throughout the last few years.

Finally, the members of my family, Colleen, Paul, and Kate Bosco, have been incredibly supportive throughout this entire process, despite my uncanny ability to forget to return telephone calls. And Michelle Lukiman, who has challenged me in so many ways that even the PhD process has failed to do. Thank you all.

Jeffrey P. Bosco
May 30th, 2014
Pasadena, CA

Abstract

The prospect of terawatt-scale electricity generation using a photovoltaic (PV) device places strict requirements on the active semiconductor optoelectronic properties and elemental abundance. After reviewing the constraints placed on an “earth-abundant” solar absorber, we find zinc phosphide (α - Zn_3P_2) to be an ideal candidate. In addition to its near-optimal direct band gap of 1.5 eV, high visible-light absorption coefficient ($>10^4 \text{ cm}^{-1}$), and long minority-carrier diffusion length ($>5 \text{ }\mu\text{m}$), Zn_3P_2 is composed of abundant Zn and P elements and has excellent physical properties for scalable thin-film deposition. However, to date, a Zn_3P_2 device of sufficient efficiency for commercial applications has not been demonstrated. Record efficiencies of 6.0% for multicrystalline and 4.3% for thin-film cells have been reported, respectively. Performance has been limited by the intrinsic p-type conductivity of Zn_3P_2 which restricts us to Schottky and heterojunction device designs. Due to our poor understanding of Zn_3P_2 interfaces, an ideal heterojunction partner has not yet been found.

The goal of this thesis is to explore the upper limit of solar conversion efficiency achievable with a Zn_3P_2 absorber through the design of an optimal heterojunction PV device. To do so, we investigate three key aspects of material growth, interface energetics, and device design. First, the growth of Zn_3P_2 on GaAs(001) is studied using compound-source molecular-beam epitaxy (MBE). We successfully demonstrate the pseudomorphic growth of Zn_3P_2 epilayers of controlled orientation and optoelectronic properties. Next, the energy-band alignments of epitaxial Zn_3P_2 and II-VI and III-V semiconductor interfaces are measured via high-resolution x-ray photoelectron spectroscopy in order to determine the most appropriate heterojunction partner. From this work, we identify ZnSe as a nearly ideal n-type emitter for a Zn_3P_2 PV device. Finally, various II-VI/ Zn_3P_2 heterojunction solar cells designs are fabricated, including substrate and superstrate architectures, and evaluated based on their solar conversion efficiency.

Contents

Acknowledgements	iv
Abstract	vii
List of Figures	xii
List of Tables	xvi
List of Publications	xvii
1 Introduction to earth-abundant photovoltaics	1
1.1 Thin film PV	5
1.1.1 Physics of thin film solar cells	5
1.1.2 Current thin film PV technologies	8
1.2 Properties of zinc phosphide (α -Zn ₃ P ₂)	10
1.2.1 Physical properties	10
1.2.2 Optical properties	12
1.2.3 Electronic properties	14
1.2.4 Materials challenges	15
1.3 Review of prior Zn ₃ P ₂ photovoltaic device studies	16
1.3.1 Mg/Zn ₃ P ₂ Schottky diodes	16
1.3.2 Heterojunction Zn ₃ P ₂ solar cells	18
1.4 Scope of this thesis	19

2	Growth of Zn_3P_2 by molecular-beam epitaxy	21
2.1	Introduction	21
2.2	Fundamentals of molecular-beam epitaxy	24
2.3	Zn_3P_2 compound source	27
2.3.1	Synthesis of Zn_3P_2 from the elements	27
2.3.2	Zn_3P_2 compound effusion source	29
2.4	Epilayer growth	31
2.4.1	Heteroepitaxial substrate	32
2.4.2	Initial growth results	34
2.4.3	Two-dimensional growth	37
2.5	Conclusions	37
3	Ex situ characterization of Zn_3P_2 epilayers	39
3.1	Growth rate and film morphology	39
3.2	Surface and interface characterization	44
3.3	Optical properties	46
3.4	Electrical properties	47
3.4.1	Intrinsic doping	48
3.4.2	Extrinsic p-type doping	50
3.4.3	Extrinsic n-type doping	52
3.5	Conclusions	54
4	Growth and characterization of II-VI materials	57
4.1	Zinc sulfide (ZnS) growth	59
4.2	Zinc selenide (ZnSe) growth	64
4.3	Cadmium sulfide (CdS) growth	66
4.4	Zinc oxide (ZnO) sputter deposition	67
4.5	Alternative: $\text{Zn}_x\text{Mg}_{1-x}\text{S}_y\text{Se}_{1-y}$ quaternary alloy	68
4.6	Conclusions	69

5	Band energetics of II-VI/Zn_3P_2 heterostructures	71
5.1	Introduction to energy-band alignments	71
5.1.1	Anderson energy-band alignment	72
5.1.2	Effective dipole model	72
5.1.3	Advanced methods	76
5.2	Experimental determination of ΔE_V and ΔE_C	76
5.2.1	X-ray photoelectron spectroscopy measurement	78
5.2.2	DFT determination of the E_{VBM} position	80
5.3	Band alignment results	83
5.3.1	Bulk semiconductor valence-band region	83
5.3.2	$\text{ZnS}/\text{Zn}_3\text{P}_2$ band alignment	86
5.3.3	$\text{ZnSe}/\text{Zn}_3\text{P}_2$ band alignment	88
5.3.4	$\text{CdS}/\text{Zn}_3\text{P}_2$ band alignment	90
5.3.5	$\text{ZnO}/\text{Zn}_3\text{P}_2$ band alignment	91
5.4	Discussion	92
5.4.1	II-VI/ Zn_3P_2 band offsets – measurement vs. prediction	92
5.4.2	Band alignment and photovoltaic device performance	95
5.5	Conclusions	97
6	Zn_3P_2 photovoltaic devices	99
6.1	Substrate devices	99
6.1.1	$\text{ZnS}/\text{Zn}_3\text{P}_2$ heterojunction solar cell	100
6.1.2	$\text{ZnSe}/\text{Zn}_3\text{P}_2$ solar cells	103
6.2	Superstrate ZnSe devices	105
6.2.1	$\text{Zn}_3\text{P}_2/\text{ZnSe}$ film characterization	106
6.2.2	Contact measurements	108
6.2.3	Mesa device characterization	110
6.3	Alternative: Graphene/ Zn_3P_2 Field-effect solar cell	113
6.4	Conclusions	115
7	Final remarks	117

Bibliography	119
Appendix A	136
A.1 Comparison of potential heteroepitaxial templates	136
A.2 E_g and χ calculations for $\text{Zn}_x\text{Mg}_{1-x}\text{S}_y\text{Se}_{1-y}$ quaternary alloys .	136
A.3 Calculated DFT band structures for II-VI semiconductors . . .	138
A.4 X-ray photoionization cross sections for group II, V, and VI elements	141
A.5 XPS data for II-VI/ Zn_3P_2 heterojunctions	142

List of Figures

1.1	Estimated area of installed PV required to meet the current U.S. total energy and electricity consumption.	2
1.2	World annual production vs. abundance for elements available in the Earth's crust.	4
1.3	Schematic diagram and ideal current-voltage characteristics of a p-n junction photovoltaic device.	6
1.4	The Zn–P binary phase diagram and unit cell for the α -Zn ₃ P ₂ tetragonal crystal structure.	11
1.5	Electronic band structure of α -Zn ₃ P ₂ calculated by hybrid DFT.	13
1.6	Process flow for the design and optimization of Zn ₃ P ₂ solar cells.	19
2.1	Schematics of a standard Knudsen effusion cell and the reflection high-energy electron diffraction (RHEED) measurement. .	25
2.2	Synthesis process and furnace setup for lab-scale production of phase pure Zn ₃ P ₂ from the elements.	28
2.3	Zn ₃ P ₂ compound source beam pressure and vapor composition.	30
2.4	RHEED images of the GaAs(001) surface after exposure to different surface preparation techniques.	34
2.5	RHEED images of the Zn ₃ P ₂ growth surface on GaAs(001) under increasing additional Zn flux.	35
2.6	Comparison of RHEED and simulated SAED patterns collected on three-dimensional Zn ₃ P ₂ surfaces.	36

2.7	RHEED images collected on Zn_3P_2 epilayers grown at varying substrate temperatures.	38
3.1	Zn_3P_2 growth rate as a function of substrate temperature. . . .	40
3.2	AFM topography images of Zn_3P_2 surfaces for films grown at increasing substrate temperatures.	41
3.3	Symmetric HRXRD and rocking curves of Zn_3P_2 epilayers. . . .	42
3.4	Reciprocal space maps collected on thin Zn_3P_2 epilayers.	43
3.5	Transmission electron micrographs of pseudomorphic Zn_3P_2 layers with thicknesses of 50 nm and 150 nm	44
3.6	HR-TEM of the $\text{Zn}_3\text{P}_2/\text{GaAs}$ interface showing the presence of a strained GaP layer.	46
3.7	STM images and the proposed growth mechanism of Zn_3P_2 on the Ga-rich GaAs(001) surface.	47
3.8	Refractive index and extinction coefficient collected on an optically thick Zn_3P_2 epilayer.	48
3.9	Film resistivity and hole density and mobility measured for Zn_3P_2 epilayers as a function of thickness.	49
3.10	RHEED images of Zn_3P_2 surfaces grown with Ag, Al, and S impurity incorporation.	51
3.11	Thin-film resistivity and hole mobility of annealed Ag-doped Zn_3P_2 epilayers.	53
3.12	Symmetric HRXRD of zinc sulfide-phosphide epilayers.	55
4.1	RHEED images of ZnS epilayers grown on GaAs(001).	60
4.2	High-resolution XRD and TEM of ZnS grown on GaAs(001). . .	61
4.3	Hall effect and SIMS measurements of Al-doped ZnS epilayers. . .	63
4.4	High-resolution XRD of ZnSe epilayers grown on GaAs(001). . .	65
4.5	TEM and SAED collected on a 300 nm thick, pseudomorphic ZnSe film grown on GaAs(001).	66

4.6	Van der Pauw resistivity vs. Hall carrier concentration of Al-doped ZnSe epilayers grown on GaAs(001).	67
4.7	a_o , χ , and E_g calculated for a $\text{Zn}_x\text{Mg}_{1-x}\text{S}_y\text{Se}_{1-y}$ quaternary alloy.	69
5.1	Original Anderson energy-band diagrams for an ideal semiconductor heterojunction.	73
5.2	Schematic of the heterojunction effective dipole calculation proposed by Ruan and Ching.	75
5.3	Schematic of the Kraut method for determining ΔE_V using photoemission measurements.	78
5.4	The Au 4 <i>f</i> core level x-ray photoelectron spectrum.	83
5.5	Comparison x-ray photoelectron spectra and the calculated VB-DOS for the valence-band region of bulk Zn_3P_2	84
5.6	X-ray photoelectron spectra and DFT calculations for the valence-band regions of bulk II-VI films.	85
5.7	XPS survey scans of ZnS/ Zn_3P_2 heterojunction interfaces.	86
5.8	Fitted XPS data and the calculated energy-band diagram of the ZnS/ Zn_3P_2 heterojunction.	87
5.9	Fitted XPS data and the calculated energy-band diagram of the ZnSe/ Zn_3P_2 heterojunction.	89
5.10	Fitted XPS data and the calculated energy-band diagram of the CdS/ Zn_3P_2 heterojunction.	90
5.11	Fitted XPS data and the calculated energy-band diagram of the ZnO/ Zn_3P_2 heterojunction.	92
5.12	Comparison of predicted and measured II-VI/ Zn_3P_2 heterojunction band offsets.	93
6.1	Schematic of a substrate II-VI/ Zn_3P_2 heterojunction solar cell.	100
6.2	Dark and illuminated I-V response of a ZnS/ Zn_3P_2 heterojunction photovoltaic device.	101
6.3	Schematic and I-V response of the Mg/ZnS/ Zn_3P_2 MIS device.	102

6.4	Dark and illuminated I-V response of a ZnSe/Zn ₃ P ₂ heterojunction photovoltaic device.	104
6.5	High-resolution TEM and XPS of the untreated ZnSe/Zn ₃ P ₂ heterojunction interface.	105
6.6	Alternative growth strategies for improving the ZnSe emitter.	106
6.7	High-resolution XRD and TEM of a superstrate Zn ₃ P ₂ /ZnSe heterojunction interface.	107
6.8	Transmission line data and contact resistances for n-GaAs.	109
6.9	Transmission line data and contact resistance for n-ZnSe.	110
6.10	I-V measurements for estimating the contact resistance at n-ZnSe/n-GaAs interfaces.	111
6.11	Schematic of the mesa architecture for a superstrate Zn ₃ P ₂ /ZnSe photovoltaic device.	112
6.12	Dark and illuminated I-V curves of etch-thru and masked Zn ₃ P ₂ /ZnSe mesa devices.	113
6.13	Cross-sectional schematic of the Field-effect gated graphene/Zn ₃ P ₂ Schottky device.	114
6.14	Ideal and measured band diagrams for a graphene/Zn ₃ P ₂ device under non-equilibrium, equilibrium, and forward-bias conditions.	115
6.15	Top-view image and I-V data of a graphene/Zn ₃ P ₂ device under bias.	116
A.1	Thermal expansivity vs. lattice mismatch for a large number of potential crystalline substrate materials.	137
A.2	Band diagrams for Zn ₃ P ₂ and II-VI compound semiconductors.	139

List of Tables

1.1	Properties of champion Zn_3P_2 solar cells.	17
3.1	Tabulated data of XRD, van der Pauw, and Hall effect measurements.	56
5.1	X-ray photoelectron spectroscopy core-level fitting parameters.	81
A.1	Calculated effective mass values (m_h/m_o) for the first three valence bands of Zn_3P_2	140
A.2	Electronic properties of Zn_3P_2 used in the dipole calculations. .	140
A.3	X-ray photoionization cross sections of group II, V, and VI elements.	141
A.4	XPS binding energies for $\text{ZnS}/\text{Zn}_3\text{P}_2$ heterointerface samples .	143
A.5	XPS binding energies for $\text{ZnSe}/\text{Zn}_3\text{P}_2$ heterointerface samples .	144
A.6	XPS binding energies for $\text{CdS}/\text{Zn}_3\text{P}_2$ heterointerface samples .	145
A.7	XPS binding energies for $\text{ZnO}/\text{Zn}_3\text{P}_2$ heterointerface samples .	146

List of Publications

The work in this thesis was primarily drawn from the following publications:

- J.P. Bosco, S.J. Rozeveld, and H.A. Atwater. “Growth and morphology of ZnSe/Zn₃P₂ heterojunction solar cells.” *Submitted to IEEE J. Photovolt.*, (2014).
- J.P. Bosco, G.M. Kimball, N.S. Lewis, and H.A. Atwater. “Pseudomorphic growth and strain relaxation of α -Zn₃P₂ on GaAs(001) by molecular-beam epitaxy.” *J. Cryst. Growth*, **363** (2013) 205-210.
- J.P. Bosco, D.O. Scanlon, G.W. Watson, N.S. Lewis, and H.A. Atwater. “Energy-band alignment of II-VI/Zn₃P₂ heterojunctions from X-ray photoemission spectroscopy.” *J. Appl. Phys.*, **113** (2013) 203705.
- J.P. Bosco, S.B. Demers, G.M. Kimball, N.S. Lewis, and H.A. Atwater. “Band alignment of epitaxial ZnS/Zn₃P₂ heterojunctions.” *J. Appl. Phys.*, **112** (2012) 093703.
- J.P. Bosco, S.F. Tajdar, and H.A. Atwater. “Molecular-beam epitaxy of n-type ZnS: A wide band gap emitter for heterojunction PV devices.” *Proc. 18th IEEE Photovolt. Spec. Conf.*, Austin, June 3-8 2012 (IEEE, New York, 2012).
- G.M. Kimball, J.P. Bosco, A.M. Muller, S.F. Tajdar, B.S. Brunschwig, H.A. Atwater, and N.S. Lewis. “Passivation of Zn₃P₂ substrates by

aqueous chemical etching and air oxidation.” *J. Appl. Phys.*, **112** (2012) 106101.

- S. Jeon, J.P. Bosco, S.S. Wilson, S.J. Rozeveld, H. Kim, and H.A. Atwater. “Growth mechanism and electronic structure of Zn_3P_2 on the Ga-rich GaAs(001) surface.” *Accepted, J. Phys. Chem. C*, (2014).
- O. Vazquez-Mena, J.P. Bosco, O. Ergen, H.I. Rasool, A. Fathalizadeh, M. Tosun, M. Crommie, A. Javey, H. Atwater, A. Zettl. “Performance enhancement using the field-effect in a graphene-zinc phosphide junction solar cell.” *Accepted, Nano Lett.*, (2014).
- S.S. Wilson, J.P. Bosco, Y. Tolstova, D.O. Scanlon, G.W. Watson, and H.A. Atwater. “Interface stoichiometry control to improve device performance in $\text{ZnO}/\text{Cu}_2\text{O}$ heterojunction solar cells.” *Submitted to Energy Environ. Sci.*, (2014).

CHAPTER 1

Introduction to earth-abundant photovoltaics

In 2011, the United States consumed a total of 97.5 *quadrillion* BTU of energy.^{1*†} This is an average of 3.26 terawatts (TW) of continuous energy usage. Of that total, electricity consumption contributed roughly 14 qBTU (0.46 TW average). Unfortunately, only 9% of the total US consumption in 2011 was generated from renewable sources and only 0.2%, or 0.2 qBTU (6.7 GW ave.), was generated from solar energy conversion; the rest being provided by fossil fuels and nuclear energy. On the other hand, in the US alone roughly 1365 qBTU (45.7 TW) of solar insolation is available for collection and direct conversion to electricity by a photovoltaic (PV) device,² greater than 10× our total annual energy consumption and 100× our annual electricity consumption. *The photovoltaic effect refers to the generation and separation of charge carriers (electrons and holes) created by the interaction of a semiconductor material with a photon. This separation usually occurs by means of a built-in electric field produced in solid state devices such as p-n junctions and metal-*

*quadrillion = 10^{15} , designated as “q” from here forward.

†BTU = British Thermal Unit, equivalent to 1.055 kJ of energy. Brewing a standard pot of coffee consumes roughly 300 ~ 500 BTU.

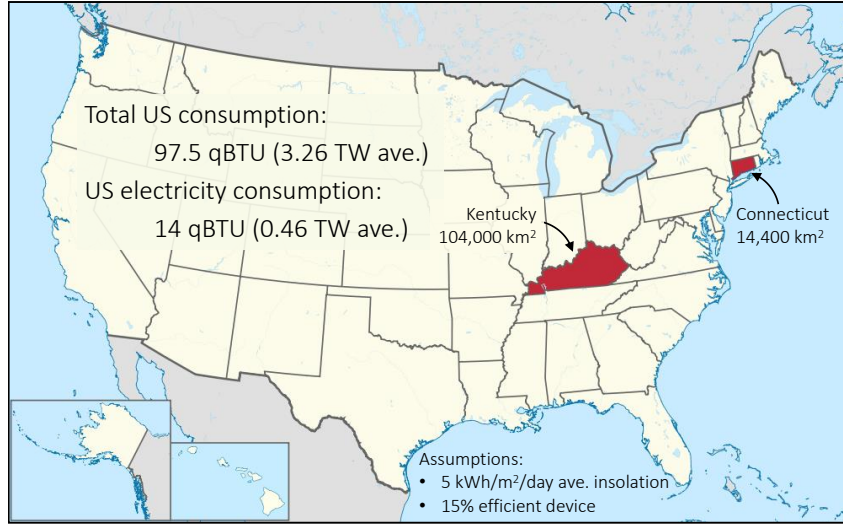


Figure 1.1: Area of PV installation at 15% efficiency necessary to meet either the US electricity (Connecticut) or total US energy consumption (Kentucky). Image of United States obtained from the Wikimedia Commons, http://commons.wikimedia.org/wiki/Main_Page..

semiconductor “Schottky” diodes.

An interesting thought experiment is to estimate the land area that would be required to provide the annual energy consumed by the US using only photovoltaic conversion. Assuming a 15% conversion efficiency (which is easily achieved using current silicon PV modules) and an average solar insolation of 5 kWh/m², approximately 14,900 km² of PV modules are required to meet our electricity consumption and 104,300 km² to meet our total energy consumption. These values are roughly equivalent to the land area of the states of Connecticut and Kentucky, respectively (see Figure 1.1). If the active semiconducting material in the PV modules has a thickness of 10 μm, this equates to $\sim 1 \times 10^6$ m³ of semiconductor, or on the order of 5×10^6 tons (given an typical semiconductor density of ~ 5 g cm⁻³).

The enormous volume of active photovoltaic material required for TW-scale photovoltaics introduces several challenges regarding the choice of semiconductor material:

- (1) **Material scarcity:** Many of the common PV materials are not abundant enough in the Earth’s crust to meet the area required for TW-scale solar generation. A plot of the World’s annual production versus abundance for elements available in the Earth’s crust is shown in Figure 1.2. The vertical red dashed line represents our approximate lower limit of ~ 1 ppm concentration necessary for a 1 TW solar installation. A second constraint is that the global production of a given material can meet the volume demand for ~ 20 GW yr^{-1} of solar installation, represented by the horizontal red dashed line. Elements including In, Te, Se, Cd, Ge, and Ga do not meet one or both of these criteria. It is important to note that Si, the most commonly deployed semiconductor for PV, does not suffer from either material scarcity or low production volume. The purpose of our work is to explore alternative material systems that could potentially meet the demands of TW-scale PV, from the perspective of both abundance and production capacity.
- (2) **Energy input:** Material purification and semiconductor growth is typically extremely energy intensive, increasing the energy payback period of the module. For example, a Si PV module requires $\sim 9,000$ kWh/kW-peak equating to a > 3 year energy payback period.³ On the other hand, a thin-film technology like CdTe requires only $\sim 3,500$ kWh/kW-peak equating to a payback period of < 1 year. A goal of this work is to deviate from traditional bulk wafer PV technologies, like Si, and explore lower-energy input thin-film technologies.
- (3) **Efficiency:** Cost of PV deployment is proportional to $1/\eta$. An efficiency of $\eta \sim 10\%$ is required for a zero-cost cell!⁴ Achieving a high solar conversion efficiency is important for any PV technology and a major challenge for the development of novel absorber materials.
- (4) **Toxicity:** PV modules are deployed for 20+ years in a variety of different outdoor environments. The potential risk of exposure of the environment

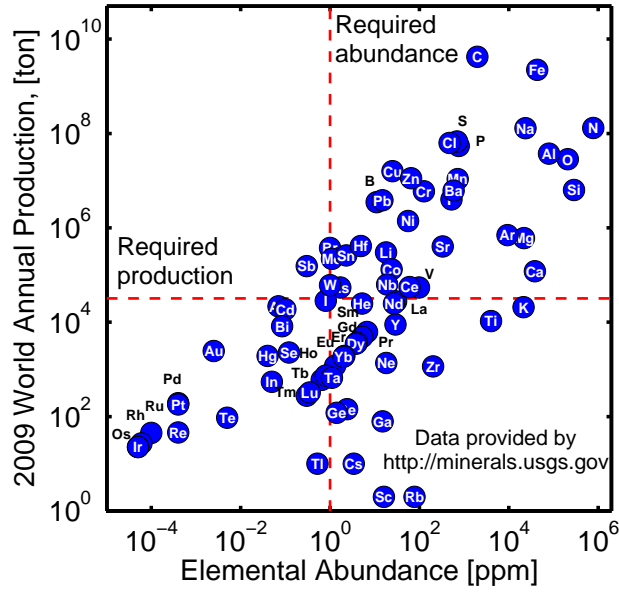


Figure 1.2: World annual production versus abundance for elements available in the Earth’s crust. The vertical red dashed line represents the lower limit of ~ 1 ppm for 1 TW-scale. The horizontal red dashed line represents the estimated lower limit of material production necessary for 20 GW yr⁻¹ solar installation. Mineral data was provided by the US Geological Survey - Mineral Information: <http://minerals.usgs.gov/>

to large quantities of semiconductor material in the event that the encapsulant in the module fails requires that the active semiconductor be relatively environmentally benign.

The above challenges outline what we have deemed the main criteria for an “earth-abundant” photovoltaic material. Such a material must not only be abundant enough for TW-scale PV deployment, but must also meet the production volume, energy-input, efficiency, and environmental restrictions that coincide with such large-scale implementation.

1.1 Thin film PV

In order to motivate our particular choice of “earth-abundant” photovoltaic semiconductor, it is necessary to explain the basic physics and properties of a typical p-n junction solar cell device. It is also useful to discuss the pros and cons of the most common commercially-available PV materials.

1.1.1 Physics of thin film solar cells

A p-n junction solar cell acts as a simple separator of electrons and holes using an electric field. The device is composed of two semiconductor layers: a p-type layer, where there is an excess of hole carriers at thermal equilibrium, and an n-type layer, where there is an excess of electrons. The electric field is generated due to the potential difference between the p-type and n-type semiconductors, resulting in a depletion region (also known as the space-charge region). There are four main fundamental processes that contribute to the current generation and collection in such a device:⁵

- (1) **Generation:** Incoming photons with energy above the band gap (i.e. $h\nu > E_g$) are absorbed in the semiconductor layer according to the Beer-Lambert law, generating electron-hole (e^- - h^+) pairs.
- (2) **Diffusion:** Both holes and electrons diffuse through the absorber layer according to Fick’s second law until they approach the depletion region.
- (3) **Drift:** In the depletion region the carriers experience drift due to the E field that is incurred between the n-type and p-type layers of the junction. Electrons are accelerated towards the n-type layer and holes towards the p-type layer.
- (4) **Recombination:** Carriers can also recombine either in the bulk or near an interface, resulting in the release of a photon with energy of the band gap of the semiconductor, or a phonon (i.e. heat). This process

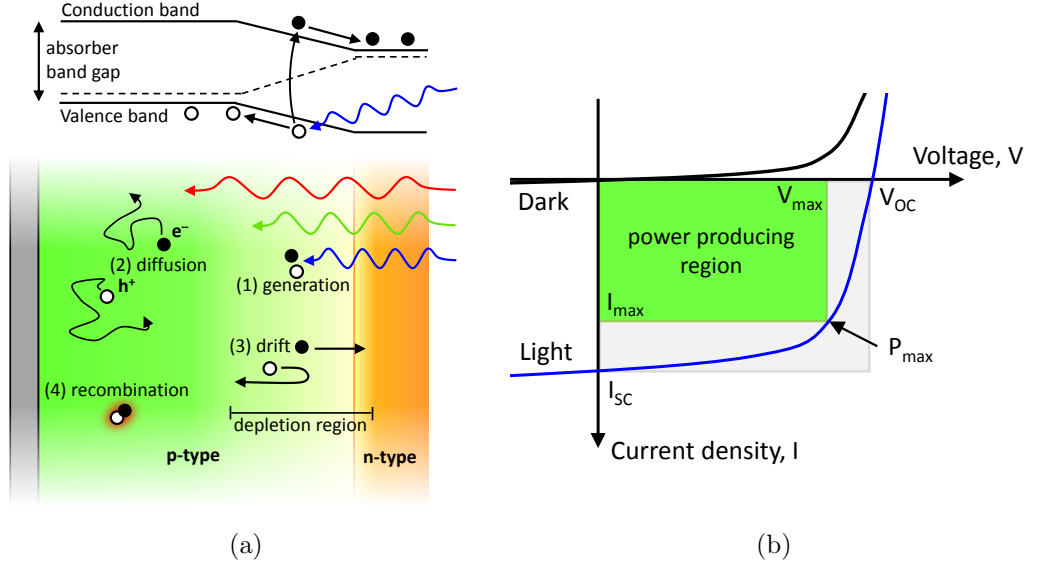


Figure 1.3: (a) Illustration of the four main charge carrier processes in a semiconductor junction and (b) the current-voltage (I-V) characteristics of a p-n junction diode under both dark and illuminated conditions.

occurs according to first-order rate kinetics since one carrier type (either electron or hole) is typically in great excess.

These four processes are illustrated schematically in Figure 1.3a. The electric field in the photovoltaic device can be generated between p-type and n-type semiconductor layers of the same material (i.e. a homojunction), layers of differing composition (i.e. a heterojunction), or possibly even a metal layer in combination with one n-type or p-type semiconductor layer* (i.e. a Schottky diode).

The behavior of charged particles in a semiconducting solid can be described mathematically with the continuity equation, which includes terms from each of the four processes described above:

$$\frac{dn}{dt} = \left. \frac{dn}{dt} \right|_{\text{generation}} + \left. \frac{dn}{dt} \right|_{\text{diffusion}} + \left. \frac{dn}{dt} \right|_{\text{drift}} + \left. \frac{dn}{dt} \right|_{\text{recombination}}, \quad (1.1)$$

* A Schottky diode is no longer a p-n junction in the strict sense, however, many of the basic fundamental processes occur in the same way as in a semiconductor p-n junction

where the quantity n represents the density of a given charge particle, which varies with both time and spacial position within the semiconductor. For minority carrier electrons in a p-type material in 1-dimension, the following equation can be derived (an identical expression is used to describe holes in an n-type material):⁵

$$\frac{\partial n_p}{\partial t} = \left[G_o e^{-\alpha(\lambda)x} \right]_{\text{gen.}} + \left[D_n \frac{\partial^2 n_p}{\partial x^2} \right]_{\text{diff.}} + \left[n_p \mu_p \frac{\partial E}{\partial x} + \mu_p E \frac{\partial n_p}{\partial x} \right]_{\text{drift}} - \left[\frac{\Delta n_p}{\tau_n} \right]_{\text{rec.}}. \quad (1.2)$$

The important physical parameters found in the above expression which are material dependent are: the wavelength-dependent semiconductor absorption coefficient, $\alpha(\lambda)$, the diffusivity, D_n (which is further dependent on the electron mobility, $D_n = \mu_n k_B T / q$), and the minority carrier lifetime, τ_n . Solving the 1-D continuity equation, one can eventually derive a simple expression for the ideal diode equation:

$$I = I_o \left[\exp \left(\frac{qV}{nk_B T} \right) - 1 \right] - I_L. \quad (1.3)$$

The above expression describes the current-voltage (I-V) characteristics of an ideal semiconductor p-n junction under illuminated conditions. The first term in the equation represents the “dark” response of the diode which is then superimposed with the photogenerated current under light conditions, I_L . The I-V characteristics of a diode under both dark and illuminated conditions are demonstrated in Figure 1.3b. Under light, a power-producing region is observed in the diode behavior. The maximum power density generated, P_{max} , is equivalent to the product of the current and voltage ($P_{\text{max}} = I_{\text{max}} \times V_{\text{max}}$). From the maximum power generated, a solar conversion efficiency, η , can be calculated as the ratio of the generated power density to the incoming radiant power density: $\eta = P_{\text{max}} / P_L$. The radiant power density is dependent on the light source. In this work we used the simulated AM1.5 1-sun solar spectrum

which has a power density of $P_L = 100 \text{ mW cm}^{-2}$.

In addition to photovoltaic conversion efficiency, there are three other important device parameters used to describe the performance of a solar cell. The open-circuit voltage, V_{oc} , is an indication of the barrier height of the device and one of the best measures of the quality of the bulk and junction interface. Intrinsic voltage losses occur for any PV device due to entropy generation of re-emitted photons. However, other voltage losses can be incurred due to bulk and surface recombination processes. The short-circuit current density, I_{sc} , represents how efficiently the device is able to generate and collect carriers and is a strong function of the band gap of the absorber layer as well as material quality and device design. Finally, the fill factor, FF , is an empirical parameter that represents the ratio of the maximum power to the product of the V_{oc} and J_{sc} ($FF = (I_{max} \times V_{max}) / (I_{sc} \times V_{oc})$). The FF is affected by both fundamental variables like the V_{oc} , as well as by sources of loss like series resistance and shunt resistance. Thus, the FF is an indication of the quality of the overall device design. The V_{oc} , I_{sc} , and FF , in addition to η , will be used to evaluate solar cell performance in later sections of this work.

1.1.2 Current thin film PV technologies

Crystalline silicon (c-Si) solar cells currently dominate the PV market. While Si is clearly abundant, both its purification and processing are very energy intensive and are therefore not easily scaled. Thin film devices use roughly $1/100^{\text{th}}$ of the material compared to crystalline cells, hence their potential for lower material and manufacturing costs and easier scale-up. On the other hand, thin films generally lack efficiency when compared to crystalline cells which makes integration more expensive. Only by increasing efficiency while maintaining low-cost fabrication will thin-film solar cell technologies become widely competitive. Current thin-film materials that have gained the attention of both academic and industrial communities include amorphous silicon (a-Si), cadmium telluride (CdTe), copper-indium-gallium diselenide (CIGS), copper-

zinc-tin-sulfide (CZTS), and gallium arsenide (GaAs). A brief summary of the advantages and disadvantages of each of these absorbers is provided below:

- **a-Si** has a *pseudo*-direct band gap of 1.7 eV which makes it a relatively good solar absorber. Due to poor electronic qualities, a-Si cells are made using intrinsic layers that must be extremely thin. Unfortunately, at such small thicknesses the films are not able to absorb light completely, limiting the cell efficiency to $\sim 10\%$.⁶ a-Si cells also tend to degrade rapidly with time, losing 30% of their peak efficiency in the first 1000 hours of operation.⁷
- **CdTe** is an ideal solar material with a direct band gap of 1.44 eV - the optimal value for a single-junction terrestrial device. CdTe sublimes congruently, simplifying the process of thin-film fabrication. To date, CdTe is the only commercially “successful” thin film technology, with submodule efficiencies up to 16%.⁶ However, there is concern that Te may not be abundant enough for TW-scale PV and Cd is extremely toxic.
- **CIGS** ($\text{CuIn}_x\text{Ga}_{1-x}\text{Se}_2$) is a flexible solar material, with a band gap tunable between 1.0 and 1.7 eV. Laboratory efficiencies as high as $\sim 20\%$ have been obtained for CIGS cells.⁶ However, large-scale production has been difficult due to the complexity of the composition. Furthermore, In is a rather expensive material and neither In nor Se are earth-abundant elements by our definition (see Figure 1.2).
- **CZTS** ($\text{Cu}_2\text{ZnSn}(\text{S},\text{Se})_4$) is a relatively recent addition to the list of interesting PV materials, demonstrating physical and optoelectronic properties similar to CIGS. CZTS has a band gap that can be tuned by the group VI anion ratio from 1.1 \sim 1.5. As of 2013, thin-film efficiencies of 12.6% have been achieved.⁸ The material is also entirely composed of earth-abundant materials. However, the quaternary composition and

kesterite structure of CZTS has led to major challenges in generating uniform materials on a large scale.

- **GaAs** is traditionally a wafer technology. However, in recent years epitaxial lift-off (ELO) techniques have allowed for the fabrication of extremely efficient (>28%) thin-film devices.⁶ Unfortunately, the epitaxial growth processes required for high-quality GaAs deposition as well as the ELO process are expensive and difficult to scale. There is also some concern over whether or not Ga metal is produced at a large enough volume, even in a thin-film architecture, for large-scale deployment. Current commercial technologies have begun to focus on consumer applications.

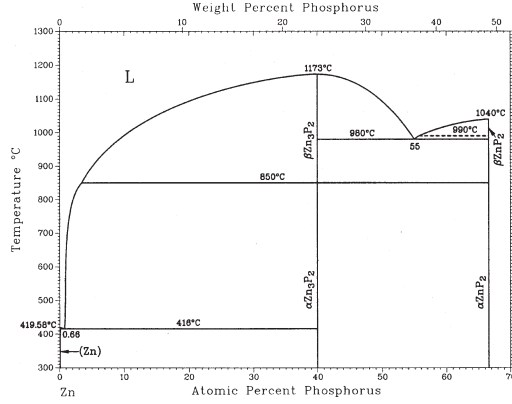
It is not clear if any of the above technologies meet the demands for TW-scale PV. Fortunately, novel solar materials offer the possibility of overcoming some of the present challenges. After careful consideration of a number of different semiconductor materials, we have found zinc phosphide (α -Zn₃P₂) to be an ideal candidate. The properties of Zn₃P₂ that make it an interesting candidate for thin-film solar applications are discussed below.

1.2 Properties of zinc phosphide (α -Zn₃P₂)

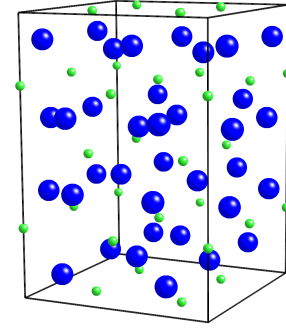
The following sections review the known physical, optical, and electronic properties of zinc phosphide. We have tried to limit the discussion to intrinsic semiconductor properties that are relevant to its application as a light absorber in thin-film photovoltaics.

1.2.1 Physical properties

Zinc phosphide can exist in several crystalline phases. The binary phase diagram for the zinc–phosphorus material system is displayed in Figure 1.4a.⁹ The solid components of the phase diagram are segregated into two primary stoichiometries: Zn₃P₂ and ZnP₂. For each stoichiometry, there also exists



(a) Zn-P binary phase diagram



(b) α -Zn₃P₂ tetragonal unit cell

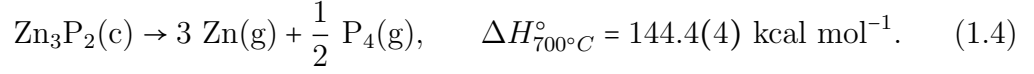
Figure 1.4: (a) The binary phase diagram for the zinc–phosphorus material system.⁹ (b) The unit cell for the tetragonal α -Zn₃P₂ crystal structure.

a low-temperature (α) and high-temperature (β) phase. While all four crystalline phases of zinc phosphide demonstrate semiconducting properties, we are primarily interested in the α -Zn₃P₂ phase since its electronic properties are most favorable for photovoltaic applications. An amorphous zinc phosphide phase, which we will denote as a-Zn_xP_y, can also exist. The amorphous phase is not thermodynamically stable and generally results from kinetically-limited growth techniques, displaying a wide range of stoichiometries.^{10–12}

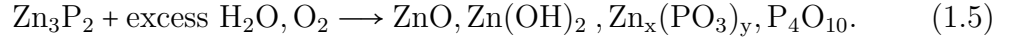
The α -Zn₃P₂ phase is characterized by a tetragonal unit cell containing 40 atoms, drastically larger than the diamond cubic and zinc-blende unit cells of many group IV, III-V, and II-VI materials. The unit cell is actually close to perfectly tetragonal, i.e. $\sqrt{2}a = c$, where $a = 8.89$ Å and $c = 11.453$ Å.^{13,14} The size and anisotropy of the unit cell has implications on the electronic properties of Zn₃P₂, which will be discussed later. However, it is interesting to note that the P sublattice of the unit cell is very similar in atomic arrangement to the anion sublattice in a III-V or II-VI material.

The physical properties of Zn₃P₂ are particularly well suited for thin-film applications. Zn₃P₂ is known to sublime congruently at relatively low temper-

atures ($< 800^\circ\text{C}$) according to the following reaction:¹⁵



Congruent sublimation and low-temperature processing greatly simplify large-scale thin-film deposition and have been a key component to the success of CdTe photovoltaics. Zinc phosphide compounds are also relatively benign to the environment,* decomposing to zinc oxide, hydroxide, and phosphate compounds:¹⁶



Finally, elemental Zn and P are abundant and available at low costs compared to other semiconductor precursors (see Figure 1.2).

1.2.2 Optical properties

The light absorption properties of Zn_3P_2 are the most relevant to its application as a PV material. Zn_3P_2 has a high visible light absorption coefficient ($\alpha > 1 \times 10^4 \text{ cm}^{-1}$) near its band edge, with 90% of light absorbed in the first 10 μm of the material.¹⁷ The absorption onset for Zn_3P_2 occurs around 1.4 ~ 1.5 eV. This is near the optimal value of 1.35 eV for a single junction device under terrestrial insolation.¹⁸

The absorption properties of any semiconductor are dominated by its electronic band structure. Figure 1.5 displays the band diagram for Zn_3P_2 as calculated by hybrid density functional theory (DFT).¹⁹ The band properties of the Zn_3P_2 are also complicated by the size of the unit cell. Interestingly,

*Interestingly, a *large* body of research (as in the vast majority of academic publications on Zn_3P_2) has gone into investigating the effect of Zn_3P_2 on the environment due to its main use as a common commercial rodenticide. A rodenticide is a material used to exterminate rodents via ingestion. Zn_3P_2 does this by generating toxic PH_3 gas upon interaction with an aqueous acidic solution, e.g. stomach acid.

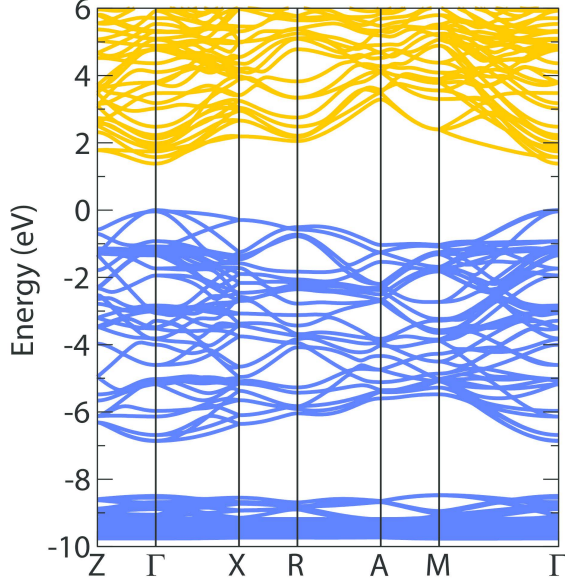


Figure 1.5: The electronic band structure of α -Zn₃P₂ as calculated by hybrid density functional theory (DFT).

Zn₃P₂ is observed to have both direct and indirect gaps, which can be seen in the band diagram at the Γ and R points. However, DFT is known to have difficulty in calculating the absolute value of the band gaps of a semiconductor, leading to some uncertainty regarding which of the gaps is the fundamental gap (i.e. the lowest magnitude gap). In fact, there has been a large amount of controversy in the literature regarding the theoretical and experimental determination of the magnitude of the direct and indirect gaps of Zn₃P₂.^{20,21} Recently, Kimball et al. used ellipsometry and steady state photoluminescence (PL) to accurately determined the room temperature direct and indirect band gaps to be $E_g^{\text{dir.}} = 1.50$ and $E_g^{\text{indir.}} = 1.38\text{eV}$, respectively.²² The indirect band gap helps explain the slower onset of the absorption coefficient for Zn₃P₂ relative to other direct band gap semiconductors.

1.2.3 Electronic properties

In addition to strong light absorption, it is crucial that a PV material has the necessary electronic properties to facilitate the collection of photo-generated electron-hole pairs. This is typically determined by the minority-carrier diffusion length, L . The diffusion length is a function of the carrier lifetime and mobility according to the following expression:⁵

$$L = \sqrt{D\tau} = \sqrt{\frac{\mu k_B T}{q}} \tau. \quad (1.6)$$

For thin-film applications, it is desirable for the absorber to have a diffusion length that is on the order of the film thickness. In the case of a p-type semiconductor like Zn_3P_2 , the electron diffusion length dominates the collection efficiency of the PV device. Catalano et al. performed electron-beam induced current (EBIC) and spectral response measurements on Mg- Zn_3P_2 Schottky diodes (fabricated on both bulk and thin-film Zn_3P_2) and observed an L_n in the range of 3 to 7 μm .^{23,24} More recently, Kimball et al. used time-resolved photoluminescence (TRPL) to study the minority carrier lifetime (τ_n) in p-type wafers.²⁵ They found the value of τ_n to be approximately 20 ns, suggesting diffusion lengths of $> 7 \mu\text{m}$, in excellent agreement with the Catalano work. The large diffusion length makes Zn_3P_2 suitable for a PV device. It is also interesting to note that the electron diffusion length observed in Zn_3P_2 is much greater than that observed in other common polycrystalline thin-film absorber materials. For instance, the L_n typically observed for CIGS and CdTe films are limited to $< 2 \mu\text{m}$.^{26,27} It is believed that the thermalization of carriers from the direct to the indirect gap in Zn_3P_2 is responsible for the larger L_n , resulting in lower bulk recombination rates.

1.2.4 Materials challenges

Some challenges still remain for implementation of Zn_3P_2 as a solar material. For example, Zn_3P_2 is an intrinsic p-type semiconductor. To date, there is only one report of n-type conductivity in Zn_3P_2 .²⁸ Materials that are p-type have the added benefit of electron minority carriers with longer diffusion lengths than holes carriers due to the higher mobility of the electron. However, trouble obtaining low-resistivity n-type material has eliminated the possibility of fabricating homojunction solar cells. Hence, prior studies have focused on devices implementing either a metal Schottky junction or a heterojunction.

In addition to n-type conductivity, the interface properties of Zn_3P_2 junctions are not well understood. It is believed that P dangling bonds or Zn precipitates result in interface states that act as carrier traps.^{25,29} A high density of interface states may lead to Fermi-level pinning, resulting in decreased photovoltaic response. For example, the interface trap density and cross section for a $\text{ZnO}/\text{Zn}_3\text{P}_2$ junction was determined by Nayar et al. to be 10^{12} cm^{-2} and 10^{-13} cm^2 , respectively.³⁰ They found that the surface preparation of Zn_3P_2 had a drastic effect on their device performance, but offered no solutions to avoid such issues like low V_{oc} . Bube and coworkers tried using a metal-insulator-semiconductor (MIS) structure to decrease the number of interface traps. However, their studies on $\text{Al}/\text{Al}_2\text{O}_3/\text{Zn}_3\text{P}_2$ diodes showed surface density of states as high as $10^{13} \text{ eV}^{-1} \text{ cm}^{-2}$.²⁹

Fortunately, Kimball et al. recently demonstrated that the surface recombination velocity of a $\text{Mg}/\text{Al}_2\text{O}_3/\text{Zn}_3\text{P}_2$ MIS structure could be substantially decreased by chemical preparation of the Zn_3P_2 surface.²⁵ They found that by exposing the Zn_3P_2 surface to a 2% $\text{Br}:\text{MeOH}$ etch, followed by a dilute aqueous $\text{HF}/\text{H}_2\text{O}_2/\text{H}_2\text{O}$ etch and air exposure reduced the SRV from $> 10^4 \text{ cm s}^{-1}$ (the untreated surface) down to $\sim 2 \times 10^3 \text{ cm s}^{-1}$. The present work explores additional ways to prepare Zn_3P_2 surfaces and interfaces in order to overcome these challenges.

1.3 Review of prior Zn_3P_2 photovoltaic device studies

The literature on Zn_3P_2 photovoltaic devices is extremely sparse compared to other more established PV materials. However, there have been a handful of studies on the performance of Zn_3P_2 absorbers. The fabrication of Zn_3P_2 homojunctions has been complicated by difficulties in creating low-resistivity, n-type material due to the formation of self-compensating, p-type intrinsic defects in the Zn_3P_2 crystal lattice.^{31,32} Hence, the majority of PV device investigations with Zn_3P_2 have focused on Schottky barrier or heterojunction solar cells, with Table 1.1 listing the champion cell properties for devices that have incorporated Zn_3P_2 as a solar absorber. These studies provide an important basis for further development of Zn_3P_2 photovoltaics. The sections below review and compare the performance of Zn_3P_2 PV devices demonstrated to date.

1.3.1 Mg/ Zn_3P_2 Schottky diodes

A Schottky structure is different from a typical semiconductor p-n junction in that the potential barrier across the device is produced between a metal and a semiconductor, instead of two semiconductors. The built-in potential of the device is nominally a function of the metal work function, ϕ_M . However, in the case of Zn_3P_2 the barrier height appears to be more a function of the heat of reaction between the metal and absorber than ϕ_M .³⁸ Mg/ Zn_3P_2 Schottky structures have demonstrated the highest solar energy-conversion efficiencies, with values of $\sim 6\%$ for devices fabricated on bulk Zn_3P_2 wafers and values of 4.3% for Zn_3P_2 thin films.^{24,33} Mg metal was chosen due to both its low ϕ and high phosphide heat of formation. Unfortunately, these devices were reported to have a high concentration of interface trap states, therefore limiting the V_{oc} to < 500 mV due to Fermi-level pinning.²⁹ In many cases, the Mg metal was

Table 1.1: Device properties of champion Schottky and heterojunction solar cells that utilized a Zn_3P_2 photovoltaic absorber.

Junction partner	Band gap	Electron affinity	Absorber fab.	Device area	Device eficiency	Open-cir. voltage	Diffusion voltage	Short-cir. current density	Fill factor
E_g	χ	A	η	V_{oc}	V_D	J_{sc}	FF		
[eV]	[eV]	[cm ²]	[%]	[mV]	[mV]	[mA cm ⁻²]			
Mg ²⁴	...	3.6	PVT	0.7	5.96	492	800	14.93	0.71
Mg ³³	...	3.6	CSS	1.0	4.3	430	1320	16.8	0.53
ITO ³⁴	3.80	...	PVT	0.06	2.1	280	...	18.4	0.4
ZnO ³⁰	3.40	4.57	PVT	0.022	1.97	260	780	11	0.59
CdS ³⁵	2.42	4.79	PVT	0.09	1.2	300	640	11.1	0.35
ZnSe ³⁶	2.70	4.09	CSS	0.1	0.81	810	1480	1.55	0.5
ZnS ³⁷	3.68	3.9	MBE	0.35	0.01	780	...	0.05	0.35

found to react with the Zn_3P_2 surface resulting in a poorly defined interfacial region.^{39,40}

While metal–semiconductor Schottky devices are simple to fabricate, they are intrinsically less efficient than semiconductor–semiconductor junctions due to lower attainable barrier heights and increased surface recombination. In fact, the barrier height of a Schottky structure is limited to roughly two-thirds of the band gap of the semiconductor.⁵ This limit can be increased with the use of a metal–insulator–semiconductor (MIS) device, but still falls short of the ideal V_{oc} attainable with a semiconductor–semiconductor junction. Optical absorption and reflection losses at the metal front contact also place an upper limit on the attainable J_{sc} in photovoltaics based on a Schottky barrier structure. The combined current density and voltage restrictions of the $\text{Mg}/\text{Zn}_3\text{P}_2$ device thus present challenges to obtaining further improvements in the PV device efficiency of such systems.

1.3.2 Heterojunction Zn_3P_2 solar cells

A preferable solution to the lack of n-type Zn_3P_2 is to create a heterojunction PV device. Zn_3P_2 heterojunction solar cells have been fabricated by use of common n-type emitters such as ZnO , Sn-doped In_2O_3 (ITO), CdS , ZnSe , and ZnS .^{30,34–37} The properties of champion heterojunction solar cells made with these emitters can also be found in Table 1.1. The solar energy conversion efficiencies of these devices to date are less than $\sim 2\%$. Nevertheless, in some cases the V_{oc} and I_{sc} values for certain devices surpass those of $\text{Mg}/\text{Zn}_3\text{P}_2$ Schottky diodes, suggesting that efficiency enhancements are possible through the use of a heterojunction solar cell design. In general, the heterojunction architecture provides a more promising path toward the development of efficient Zn_3P_2 solar cells due to fewer fundamental limitations as compared to a Schottky architecture.

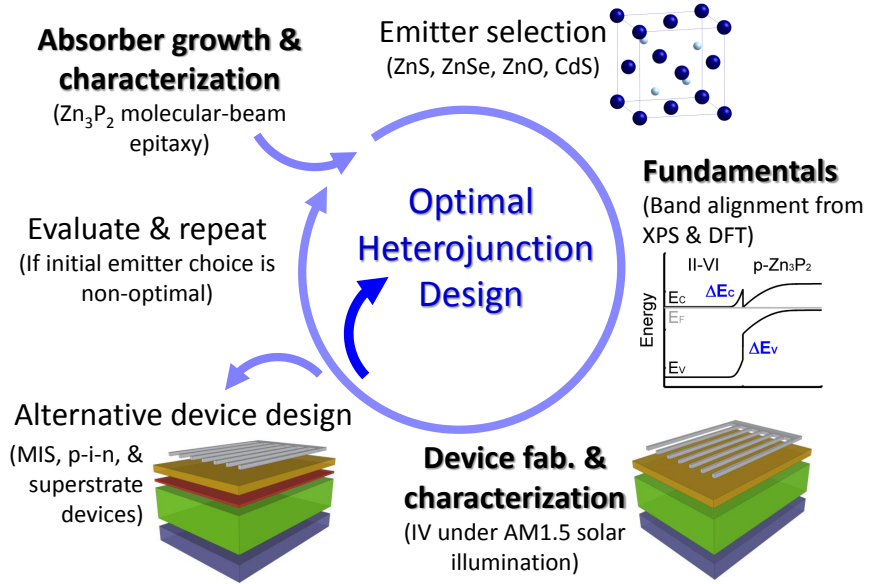


Figure 1.6: The design flow for fundamental characterization and device optimization of Zn_3P_2 heterojunction solar cells.

1.4 Scope of this thesis

The goal of this thesis is to explore the upper limit of solar conversion efficiency achievable with a Zn_3P_2 absorber. We pursue this goal primarily through the design and fabrication of an optimal Zn_3P_2 heterojunction solar cell. In the process, we explore three key aspects of material growth, interface energetics, and device engineering:

- (1) **Absorber Growth:** Compound-source molecular-beam epitaxy (MBE) is employed to grow the highest quality Zn_3P_2 thin films possible. Emphasis is on achieving control of both growth orientation and optoelectronic properties such that they are suitable for photovoltaic applications.
- (2) **Fundamental Characterization:** The energy-band alignments of epitaxial Zn_3P_2 and II-VI and III-V semiconductor interfaces are measured

in order to determine the most appropriate heterojunction partner for Zn_3P_2 .

- (3) **Device Fabrication:** Various heterojunction device designs are assessed based on the material constraints associated with both Zn_3P_2 and the II-VI semiconductors of interest.

CHAPTER 2

Growth of Zn_3P_2 by molecular-beam epitaxy

2.1 Introduction

The fabrication of an efficient p-n junction photovoltaic device places rigorous quality requirements on the active light absorber. This fact is observed by the extremely high purity Si and GaAs semiconductors used in commercially available solar cells. Typical elemental purities are on the order of 99.99999% (7N). The most efficient devices incorporate monocrystalline materials which are either produced from a monolithic boule (as in the case of Si) or deposited as a single-crystal film using an epitaxial growth technique (as in the case of GaAs). The goal of this work is to produce the highest optoelectronic quality Zn_3P_2 thin films possible. Below is a brief review of the various deposition techniques that were previously employed in growing thin films of Zn_3P_2 of varying degrees of quality.

- **Thermal evaporation:** The congruent sublimation of Zn_3P_2 allows for films to be deposited by simply subliming the material in a vacuum environment with a growth substrate within line-of-sight of the source

material. Under the right conditions, stoichiometric, crystalline films will form on the growth substrate. This technique is limited by the resublimation of the film, which is a function of the substrate temperature. Catalano and Hall produced Zn_3P_2 thin films of reasonable electronic quality on glass substrates using thermal evaporation of Zn_3P_2 compound source material.⁴¹

- **Close-space sublimation (CSS):** Similar to thermal evaporation, CSS takes advantage of the fact that Zn_3P_2 sublimates congruently. However, CSS is distinctly different from the thermal evaporation method in that the deposition occurs with the source and substrate placed in extremely close proximity, typically no more than several mm, and with a temperature gradient of roughly $100 \sim 200$ °C. The close proximity solves the problem of resublimation of the deposited film since it is recycled back to the source material. This allows for much higher substrate temperatures as well as faster growth rates. Catalano and coworkers first reported on depositing specular, pinhole-free films of Zn_3P_2 with large grain sizes (>1 μm) using the CSS technique.³³
- **Hot-wall deposition (HWD):** Hot-wall deposition is similar to thermal evaporation except that the source flux travels through an additional heating tube that is held at a different temperature (typically higher) than the source material. The additional heating can influence the sticking coefficient of the flux without modifying the evaporation rate. In particular, this can cause cracking of the sublimated phosphorus tetramer (P_4) to the phosphorus dimer (P_2) which drastically increases its sticking probability. Both Fuke et al. and Babu et al. achieved well oriented Zn_3P_2 films grown of good optoelectronic quality on glass slides using hot-wall deposition.^{42–45}
- **Sputter deposition:** Plasma-deposition techniques have been used to deposit zinc phosphide films on a number of different occasions.^{10–12,46}

Magnetron sputtering can be performed either with a sintered Zn_3P_2 target and an inert Ar working gas or a Zn target with a working gas containing a phosphine (PH_3) partial pressure. However, sputter deposition typically results in amorphous films with optical properties that deviate from the crystalline material.

- **Liquid-phase epitaxy (LPE):** Liquid-phase epitaxy of Zn_3P_2 on InP (001) has also been reported.⁴⁷ Elemental Zn and P were dissolved in a molten In solvent. They achieved oriented growth along the (224) or (004) zone axis through control of the cooling rate of the solvent. The resulting films were polycrystalline and had very high hole-carrier concentrations ($>10^{18} \text{ cm}^{-3}$), consistent with the unintentional incorporation of In as an extrinsic p-type dopant. It was also possible that the observed doping was due to unintentional diffusion of Zn extrinsic dopants into the InP substrate, which would explain the significantly higher hole mobilities that were measured in the Zn_3P_2 .
- **Chemical vapor deposition (CVD):** Chemical vapor deposition is characterized by the vapor-phase transport of the elemental constituents via an inorganic chemical precursor into a growth zone where films are deposited. Russell and coworkers demonstrated the controlled growth of Zn_3P_2 thin films using CVD with Zn vapor and PH_3 and characterized the fundamental growth mechanism.^{48,49} However, their films were not of high enough electronic quality for fabrication of rectifying Schottky devices.
- **Metalorganic chemical vapor deposition (MOCVD):** The first true example of Zn_3P_2 epitaxy was reported by Suda et al.^{50,51} using MOCVD. Similar to CVD, MOCVD transports film precursors in the vapor phase, but uses organic precursors. Suda and coworkers used dimethylzinc (DMZ) and phosphine (PH_3) gases as precursors for Zn and P, respectively. Growth was performed on GaAs(001) and ZnSe(001)

substrates because these materials have a relatively small lattice mismatch with the P sub-lattice in the tetragonal α - Zn_3P_2 unit cell (1.3% and 1.0%, respectively). The epitaxial layers grew along the $\text{Zn}_3\text{P}_2(001)$ crystallographic orientation, independently of the substrate material, and were three-dimensional in nature. Difficulties with the MOCVD technique for growing Zn_3P_2 included a small growth temperature window under which the DMZ and PH_3 precursors would properly decompose *and* the resulting Zn_3P_2 film would not quickly sublime away. An additional problem observed was stress cracks in the epitaxial films that occurred due to expansivity mismatch between the substrate and film.

- **Molecular-beam epitaxy (MBE):** Suda and coworkers also demonstrated growth of Zn_3P_2 epilayers on GaAs(001) using molecular-beam epitaxy (MBE) with separate elemental Zn and P sources.²⁸ Similar to MOCVD growth, the films produced using MBE were observed to be three-dimensional in nature using reflection high-energy electron diffraction. However, they were able to demonstrate the only instance of n-type conductivity in Zn_3P_2 , which they attributed to a large excess of Zn in the crystalline lattice (>10%).

2.2 Fundamentals of molecular-beam epitaxy

In order to obtain the highest quality films possible, MBE was chosen for the growth of Zn_3P_2 films. This technique is characterized by very low growth rates ($\sim 1 \text{ \AA s}^{-1}$) which promote the epitaxy of highly crystalline materials. In order to achieve these low rates while still maintaining low impurity incorporation, an ultra-high vacuum (UHV) environment is required ($P \leq 1 \times 10^{-9}$ Torr). Growth rate and composition control are determined by the flux of impinging atoms on the substrate surface. An atomic flux is created using a Knudsen type effusion cell (see schematic provided in Fig. 2.1a). Elemental or compound source materials are loaded into the effusion cell and evaporated

or sublimed using resistive heating. The atomic flux (\dot{n}) is controlled by the source temperature according to the Knudsen equation as follows:⁵²

$$\dot{n} = \frac{\alpha P^{\text{vap}}(T)}{\sqrt{2\pi M W R T}} N_A \quad [\text{atom m}^{-2} \text{ s}^{-1}], \quad (2.1)$$

where α and P^{vap} are the evaporation coefficient and vapor pressure for a given substance. The atomic flux results in a beam equivalent pressure (BEP) which the growth substrate is exposed to and can be measured and tuned to affect the resulting film properties.

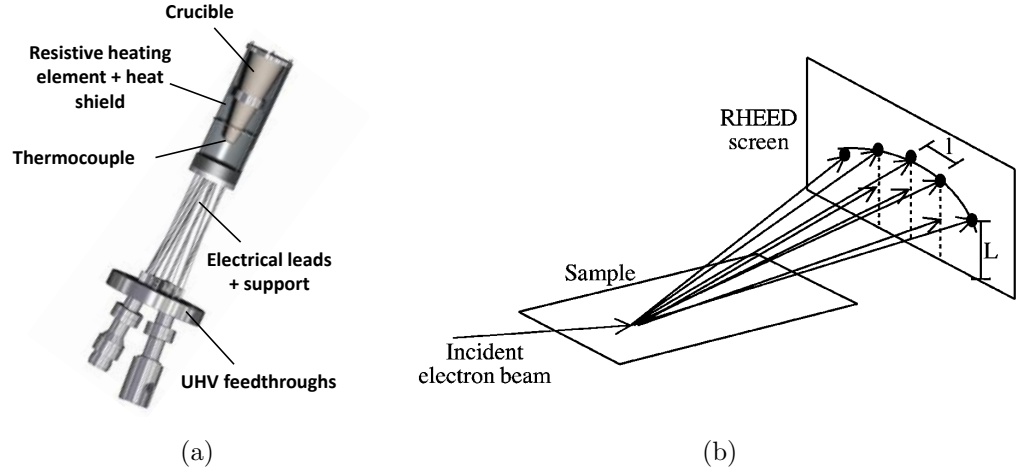


Figure 2.1: Schematics of (a) a standard Knudsen effusion cell and (b) a reflection high-energy electron diffraction (RHEED) set up where an electron beam is reflected off of a surface and the resulting diffraction pattern is collected.

In situ analysis of the epilayer growth is possible using reflection high-energy electron diffraction (RHEED). RHEED works by reflecting a high-energy electron beam off of the growth surface at incidence angles of $1 \sim 3^\circ$. The diffracted beam is directed at a phosphor screen and images are collected using a CCD (see Fig. 2.1b). Electron beam energies typically range from 10 to 30 keV and spot sizes are on the order of $100 \mu\text{m}$. For a smooth, crystalline surface, diffraction occurs on the two-dimensional (2D) grating composed of

the crystalline films surface atomic lattice and “streaks” are observed on the RHEED screen, indicative of the symmetry of the surface lattice or reconstruction. For a rough, or 3D surface, transmission diffraction takes place, resulting in “spot” patterns similar to an electron diffraction pattern. RHEED is a powerful tool to determine the morphology and epitaxial relation of the film during growth and is used extensively in the present work.

One of our initial goals was to achieve heteroepitaxial growth of Zn_3P_2 . Heteroepitaxy refers to the growth of an ideally monocrystalline film of one substance on top of a monocrystalline substrate of a different substance. Heteroepitaxy is necessary when a monocrystalline substrate of the film material is not available and offers an opportunity to control the orientation and decrease the defect density in the resulting film. There are three primary modes of heteroepitaxial growth which are all dependent on the lattice mismatch, defined in terms of the film (f) and substrate (s) in-plane lattice parameters as:

$$f = 2|a_f - a_s|/(a_f + a_s). \quad (2.2)$$

The primary growth modes are:⁵² Frank-van der Merwe or “layer-by-layer” growth which occurs when the deposited material wets the substrate surface and the film grows one monolayer at a time. This regime is typical of very small values of f . The second mode is Volmer-Weber or “island” growth. This highly three-dimensional (3D) growth is caused by very large values of f or when there is insufficient bonding between the substrate and film. Finally, Stranski-Krastanov or “S-K” growth is described by the deposition changing from layer-by-layer to island growth after the first few monolayers. S-K growth indicates a change in surface free energies with increasing film thickness. This is often caused by a slow build up in strain due to intermediate values of f . To obtain smooth, specular films, operating in a layer-by-layer growth regime is advantageous.

2.3 Zn₃P₂ compound source

The following sections describe the synthesis and characterization of the Zn₃P₂ source material and compound effusion source that were used in subsequent MBE growth experiments.

2.3.1 Synthesis of Zn₃P₂ from the elements

Due to the extreme purity requirements for molecular-beam epitaxy (>99.999% or 5N), it was necessary to synthesize our own high-purity Zn₃P₂ material.* Zn₃P₂ can be synthesized from elemental Zn and P through a high temperature physical vapor transport (PVT) process. The synthesis procedure has been outlined previously by several authors.^{53–55} The details of our specific PVT procedure are illustrated in Figure 2.2a. First, stoichiometric quantities of Zn shot (6N) and red P chunk (6N) are loaded into separate ends of a cylindrical quartz ampule (2" diameter \times 12" length). The P end of the ampule is carbon coated prior to loading the material via a methane decomposition process. The ampule is then sealed under vacuum at a pressure of $\sim 1 \times 10^{-5}$ Torr and is ready to be baked.

The high-temperature reaction takes place in a two-zone furnace and happens in several steps. Initially the carbon-coated end of the ampule is heated to 550 °C in order to convert all of the red P to liquid white P and P₄ vapor. Next, the Zn metal end and carbon-coated ends are raised to 850 °C and 650 °C, respectively. The 200 °C temperature gradient is held for roughly 18 to 24 h. During this time, the Zn metal begins to sublime and react with the vapor-phase P₄. Due to the temperature gradient, eventually all of the reacted Zn and P accumulate at the carbon-coated end of the quartz ampule, resulting in a polycrystalline boule that is composed of phase-pure α -Zn₃P₂. After the reaction period, both ends of the quartz ampule are allowed to cool to room temperature before removal from the synthesis furnace. The quartz ampule is

*Current commercial sources of Zn₃P₂ are not available at purities higher than 99.9%.

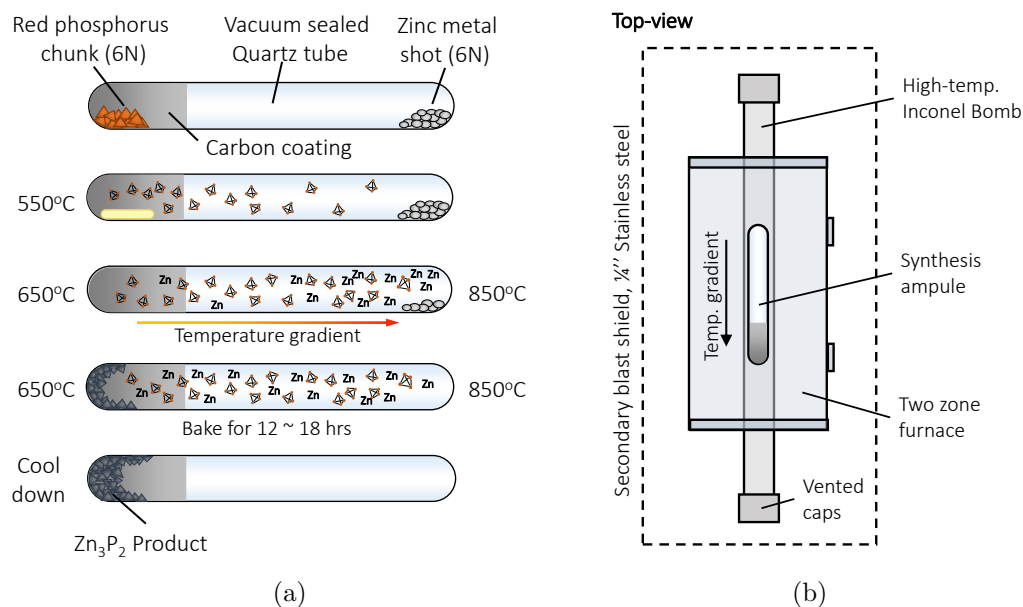
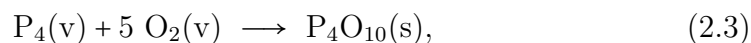


Figure 2.2: (a) The physical vapor transport (PVT) process for synthesizing phase-pure Zn_3P_2 from the elements. (b) Furnace setup and shielding for protection against accidental quartz ampule failure and P_4 explosion.

then broken in half in order to remove the Zn_3P_2 boule. The boule is ground into a fine powder using a mortar and pestle and then placed through an additional PVT process for further purification. The resulting Zn_3P_2 material is of roughly 5N purity according to ICP-MS analysis.⁵⁶

The pyrophoric nature of elemental phosphorus necessitates that the PVT process above be performed in a very controlled fashion. White phosphorus vapor reacts with oxygen spontaneously to form phosphate according to the following reaction:



where the heat and free energy of formation are $\Delta H_f^\circ = -2984 \text{ kJ/mol}$ and $\Delta G_f^\circ = -2690 \text{ kJ/mol}$, respectively.⁵⁷ If the quartz ampule fails at any point during the high temperature procedure, any P_4 in the vapor phase reacts

immediately resulting in an explosion. In fact, a number of ampule explosions have occurred during the initial scale-up of the Zn_3P_2 synthesis procedure. Most of these failures happened during the cool down process, in which the Zn_3P_2 boule contracts in volume. If the ampule is not properly carbon coated, the Zn_3P_2 adheres to the ampule and causes it to crack, exposing any remaining P_4 vapor to atmosphere.* Therefore, we have contained the synthesis ampule within an Inconel pipe that sits directly inside of the two zone furnace. The pipe has vented end caps in order to avoid pressurization. Finally, the entire furnace is surrounded by a secondary blast shield made of stainless steel. An illustration of the furnace setup and blast shield is displayed in Figure 2.2b.

2.3.2 Zn_3P_2 compound effusion source

The synthesized Zn_3P_2 material was loaded into a compound-source effusion cell with an additional cracking zone. The cracking zone was intended to convert phosphorus tetramer species (P_4) into the dimer species (P_2). The dimer species was believed to be favorable for two main reasons. First, P_4 condensation produces white phosphorus which, as mentioned earlier, is a pyrophoric substance whose accumulation within the growth chamber could be potentially dangerous. On the other hand, the P_2 species condenses as solid red phosphorus, a considerably more stable, and therefore safer compound. Furthermore, since P_2 has a larger sticking coefficient than P_4 , the use of a cracker makes the source more efficient.

Prior to any growth studies, the Zn_3P_2 effusion cell performance was evaluated. First, the beam equivalent pressure (BEP) of the cell was measured as a function of source temperature at the maximum cracker temperature of

*The most violent explosion took place during our first attempt to synthesize ZnP_2 , which requires temperatures $>950^\circ\text{C}$ and nearly twice as much red P reactant. In this case, the quartz ampule simply over-pressurized with P_4 vapor causing it to pop and then immediately combust. The remnants of the explosion was a large plume of thick white smoke and a pile of pulverized quartz.

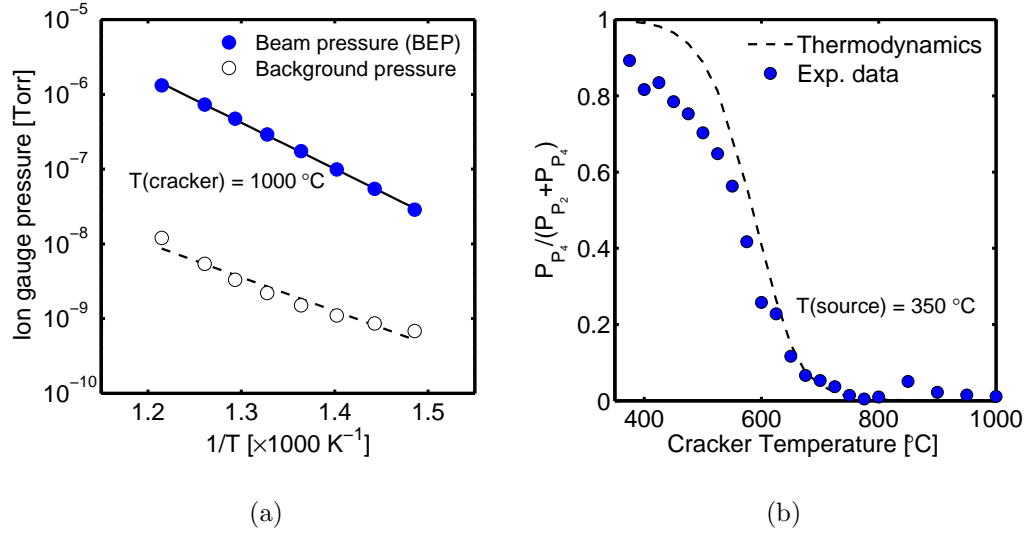


Figure 2.3: (a) Zn_3P_2 compound source effusion cell BEP as a function of the inverse source temperature. (b) Partial pressure ratio of phosphorus tetramer (P_{P_4}) to total phosphorus pressure ($P_{P_2} + P_{P_4}$) exiting the compound-source effusion cell versus cracker temperature.

1000 $^\circ\text{C}$. The BEP was determined using a standard nude ionization gauge located within the Zn_3P_2 beam path and was uncorrected for differing ionization gauge sensitivities of Zn and P_2 vapor species. The measured BEP is displayed in Figure 2.3a as a function of the inverse of the source temperature. The experimental data are well fitted to the following equation: $\log_{10}(\text{BEP}) = 3.4148 - 5971.5 \times T_{\text{source}}^{-1}$. The open circles correspond to the chamber background pressure during source operation. At typical growth source temperatures (330 \sim 380 $^\circ\text{C}$), the background pressure was approximately two orders of magnitude lower than the Zn_3P_2 BEP, which ensures a relatively low rate of impurity incorporation.

Additionally, the ratio of the partial pressure of P_4 to the total phosphorus pressure ($P_T = P_{P_2} + P_{P_4}$) exiting the source is plotted in Figure 2.3b as a function of the cracker temperature. For this experiment, the Zn_3P_2 source temperature was held at 350 $^\circ\text{C}$. The partial pressures of the P, P_2 , P_3 , and P_4

species were monitored in situ using a quadrupole mass-spectrometer located within the beam path. It is clear that the thermal treatment converts P_4 to P_2 species beginning at approximately 400 °C, and complete conversion occurs above 750 °C. Given the equilibrium constant (K_P) for the reaction between dimer and tetramer species as⁹

$$K_P = \exp\left(\frac{-\Delta G^\circ}{RT}\right) = \exp\left(\frac{-229500 + 154.5 \times T + 0.00313 \times T^2 \text{ [J mol}^{-1}\text{]}}{RT}\right), \quad (2.4)$$

the ratio of P_{P_4} / P_T can be calculated from thermodynamics as follows:

$$\frac{P_{P_4}}{P_T} = 1 + \frac{K_P}{2P_T} - \frac{\sqrt{K_P^2 + 4K_P P_T}}{2P_T}. \quad (2.5)$$

The above equation assumes that vapor phase Zn atoms do not interact with P_2 and P_4 species, which is a good assumption since gaseous Zn_3P_2 molecules have not been observed. The predicted ratio can also be found in Figure 2.3b. One can see that good agreement was found between the observed partial pressure ratio and the ratio estimated from thermodynamics. Some deviation from theory occurs at lower cracker temperatures, due to P_4 contributions in the P_2 mass spectrometer peak.*

2.4 Epilayer growth

The following sections describe the process by which Zn_3P_2 heteroepitaxy was achieved. It was necessary to choose a suitable substrate for epitaxy as well as a technique for preparing the substrate surface. Following which, RHEED experiments were used extensively to evaluate our initial growth results. Based on these findings the growth conditions were modified, resulting in high-fidelity

*The quadrupole mass spectrometer employs a thorium-iridium oxide filament that operates at nearly ~2000 °C, which is more than hot enough to result in additional cracking of the phosphorus tetramer to the dimer as well as monoatomic species.

growth.

2.4.1 Heteroepitaxial substrate

The two most important parameters for heteroepitaxy are the lattice mismatch and thermal expansivity mismatch between the substrate and epilayer materials. As mentioned earlier, the lattice mismatch dominates the growth mechanism and a small lattice mismatch provides an opportunity to decrease interfacial and bulk defects in the epilayer. The thermal expansivity mismatch between the substrate and epilayer becomes important when the growth temperature is far from room temperature ($> 300\text{ }^{\circ}\text{C}$). Contraction in either the substrate or epilayer during cooling can result in microcracks in the epilayer. Microcracks were seen previously for MOCVD growth of Zn_3P_2 .⁵⁰ Ideally, the substrate material should be both well lattice matched and thermal expansivity matched to the epilayer material. We reviewed a large number of materials and compared their lattice parameters and expansivity coefficients with those of Zn_3P_2 (See Figure A.1 in section A.1). Of those materials, the GaAs(001) surface was chosen as the substrate for epitaxial growth since the phosphorus sub-lattice of Zn_3P_2 is similar to that of arsenic with a room-temperature lattice mismatch lower than 1.3%. Other possible substrate candidates included ZnSe and Ge, with 1.0% and 1.2% lattice mismatches, respectively. Despite having better lattice match, both materials were ruled out due to other issues; conductive ZnSe substrates are not widely available and the non-polar surface of Ge complicates the heteroepitaxy of polar compounds such as Zn_3P_2 .

Several different methods were attempted to prepare the GaAs(001) surface prior to Zn_3P_2 growth. The goal of the surface preparation was to remove the GaAs native oxide, leaving a clean, atomically smooth surface for subsequent growth. Initially, a chemical etching procedure was adopted based on literature reports.⁵⁸ The etching procedure involved three steps:

- (1) $\text{H}_2\text{SO}_4\text{:H}_2\text{O}_2\text{:H}_2\text{O}$ (4:1:100) for 2 min in order to remove any adventitious

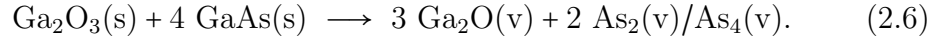
carbon contamination from the surface.

(2) HCl:H₂O (3:1) for 2 min to remove Ga₂O₃ and Ga₂O surface species, leaving behind an As-terminated surface.

(3) DI-H₂O rinse and nitrogen blow dry.

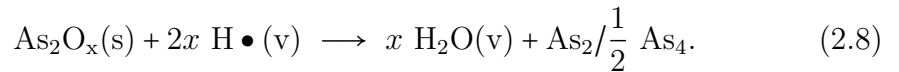
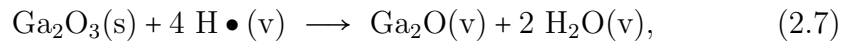
However, the wet etch process failed to completely remove the GaAs native oxide and also resulted in increased surface roughness based on RHEED images.

The second technique adopted was to simply anneal the GaAs substrate at a temperature slightly above its congruent sublimation temperature (~580 °C), which results in decomposition of the native oxide. The anneal takes advantage of the fact that Ga₂O₃ will react with subsurface GaAs to form Ga₂O according to:^{59,60}



Both the Ga₂O and As₄ product species sublime readily at temperatures > 400 °C, leaving behind an oxide-free GaAs surface. This procedure worked considerably better than the wet chemical etch. However, the anneal resulted in large etch pits in the GaAs surface due to Ga₂O₃ consuming the subsurface GaAs. The anneal procedure also leaves a largely Ga-terminated surface, with some formation of liquid Ga droplets.

The final, and most successful method for removing the GaAs native oxide was via exposure of the surface to an atomic hydrogen plasma.⁶¹ Atomic H is capable of reducing the Ga₂O₃ to Ga₂O and As₂O_x to elemental As at temperatures of 400 °C < T_{sub} < 500 °C, according to the following reactions:^{60,62,63}



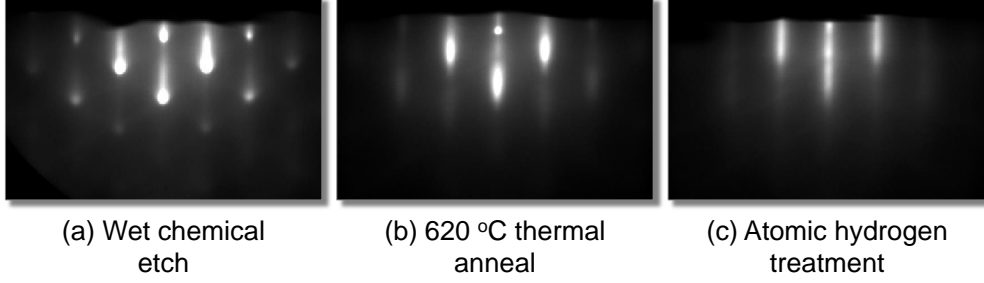


Figure 2.4: *In situ* RHEED images of the GaAs(001) after (a) wet chemical etching, (b) a 620 °C thermal anneal, and (c) a 20 min exposure to an atomic hydrogen flux at 450 °C.

The low temperature reduction drastically limits the reaction of the oxide with subsurface GaAs therefore limiting the formation of both pits and liquid Ga droplets. A comparison of RHEED images for the three different substrate preparation methods is displayed in Figure 2.4. Clearly, the streakiest RHEED pattern was obtained for the atomic H treatment, indicating a smoother GaAs surface. Atomic H preparation of the GaAs(001) surface was used for all subsequent experiments reported in this work.

2.4.2 Initial growth results

Preliminary growth studies were performed using the Zn_3P_2 compound source with high cracker temperatures (>800 °C) in order to guarantee efficient phosphorus incorporation in the deposited films. However, this strategy alone resulted in amorphous films with P-rich stoichiometry. Varying the substrate temperature did not produce crystalline films but strongly affected the growth rate. Crystalline films were obtained when an additional Zn flux was added to the growth recipe. Figure 2.5 shows RHEED patterns recorded at different time intervals during the growth under three Zn fluxes. For all three growths the Zn_3P_2 BEP and substrate temperature were held constant at 1×10^{-6} Torr and 350 °C, respectively. At low Zn BEP (left column), the RHEED patterns were hazy with diffuse spots, indicative of a primarily amorphous film growth.

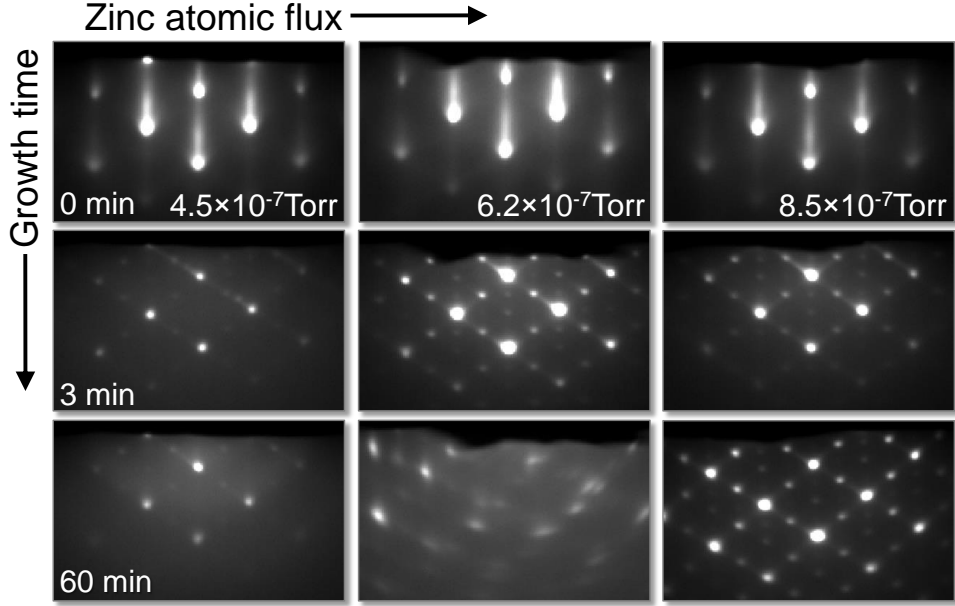


Figure 2.5: *In situ* RHEED images of Zn_3P_2 epitaxial growth on $\text{GaAs}(001)$ at different additional Zn BEP. All of the growths were performed at a substrate temperature of $T_{\text{sub.}} = 350^\circ\text{C}$ and Zn_3P_2 BEP of 1×10^{-6} Torr. Images were recorded along the $\text{GaAs } [0\bar{1}1]$ zone axis.

At higher Zn BEP (middle column), the background remained hazy while a more complex spot pattern was observed. The complex pattern is likely due to uncontrolled crystal twinning resulting in multiple grain orientations. Finally, for the highest Zn BEP (right column) a sharp spot pattern was observed, indicative of a highly crystalline and oriented film with a rough surface.

The higher overpressure of Zn metal required to obtain crystalline Zn_3P_2 films is rather counter intuitive. Growth of group III-V phosphide materials like GaP and InP normally require extremely high overpressures of phosphorus ($P_{\text{V}}:P_{\text{III}} \sim 30:1$) in order to obtain stoichiometric material. The difference between typical III-V growth and Zn_3P_2 growth is that the Zn vapor pressure is much higher than that of a group III element, resulting in a much lower comparative sticking coefficient and thus a more stoichiometric beam composition is required.

The spot pattern obtained from higher Zn fluxes resembles that of a trans-

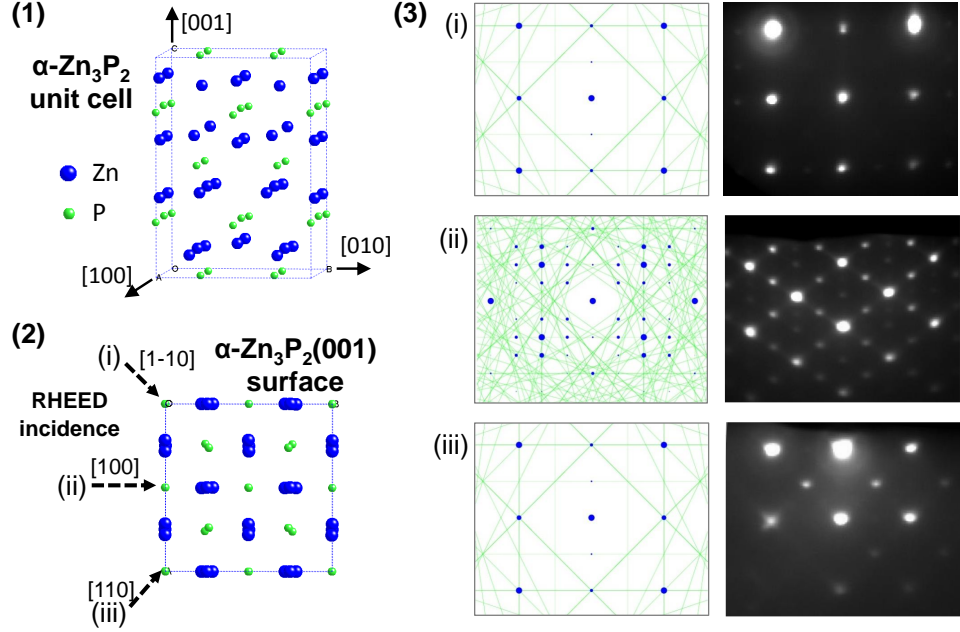


Figure 2.6: (a) α - Zn_3P_2 unit cell, (b) in-plane atomic arrangement of the α - $\text{Zn}_3\text{P}_2(001)$ surface. (c) Comparison of RHEED patterns of the (001) surface with along different zone axes with electron diffraction simulations for the α - Zn_3P_2 tetragonal crystal structure.

mission electron diffraction pattern, indicating that the growth was three-dimensional. While 3D growth is not necessarily desirable for obtaining high quality films, it does allow the use of the RHEED patterns to determine the in-plane epitaxial relationship between Zn_3P_2 and GaAs. RHEED patterns taken for three different zone axes of the Zn_3P_2 film are displayed in the left column Figure 2.6. The right column shows simulated electron diffraction patterns for the same zone axes assuming a tetragonal crystal structure.⁶⁴ From the RHEED patterns, a 45° in-plane rotation about the $\text{Zn}_3\text{P}_2(001)$ direction is observed with respect to GaAs. Hence, the epitaxial relationship between the epilayer and the substrate was $\text{Zn}_3\text{P}_2(004) \parallel \text{GaAs}(002)$ and $\text{Zn}_3\text{P}_2(202) \parallel \text{GaAs}(1\bar{1}1)$. This rotation occurs because it results in a slight decrease in lattice mismatch between the Zn_3P_2 and GaAs.

2.4.3 Two-dimensional growth

An additional way to obtain crystalline films of Zn_3P_2 was to decrease the effusion source cracker temperature. At cracker temperatures $< 500^\circ\text{C}$, the vapor-phase phosphorus is composed predominately of the P_4 species, which has a much lower sticking coefficient than the P_2 species. Figure 2.7 displays RHEED images collected along the $[100]$ zone axis of Zn_3P_2 films that were grown with a cracker temperature of 450°C and at substrate temperatures of 150°C , 200°C , and 250°C , respectively. The RHEED images of Zn_3P_2 films that were grown at $200 \sim 235^\circ\text{C}$ exhibited streaky (1×1) patterns, indicating highly crystalline, oriented film growth that occurred two-dimensionally. The faint appearance of half-order streaks in the RHEED patterns suggested that a partial surface reconstruction occurred for thicker films. The reconstruction is consistent with Zn-termination of the $\text{Zn}_3\text{P}_2(001)$ surface. All RHEED images observed for films that were grown at substrate temperatures $< 175^\circ\text{C}$ revealed cloudy, specular beam reflection with only a faint appearance of crystalline peaks, indicating that the films were primarily amorphous. The deposition of amorphous material established a practical lower bound of $\sim 200^\circ\text{C}$ on the substrate temperature for Zn_3P_2 epitaxy. Spotty RHEED patterns were observed for films that were grown at substrate temperatures of $> 250^\circ\text{C}$, indicating that these films were crystalline and oriented, but that their surfaces were significantly rougher than the surfaces of films that were grown at lower temperatures. The observed increase in roughness is consistent with the partial re-sublimation of the deposited Zn_3P_2 film along some preferred orientation.

2.5 Conclusions

The growth of epitaxial Zn_3P_2 films was successfully demonstrated using compound-source MBE. It was found that the cracking of P_4 vapor species to P_2 was not favorable for the growth of films with smooth surfaces, which is

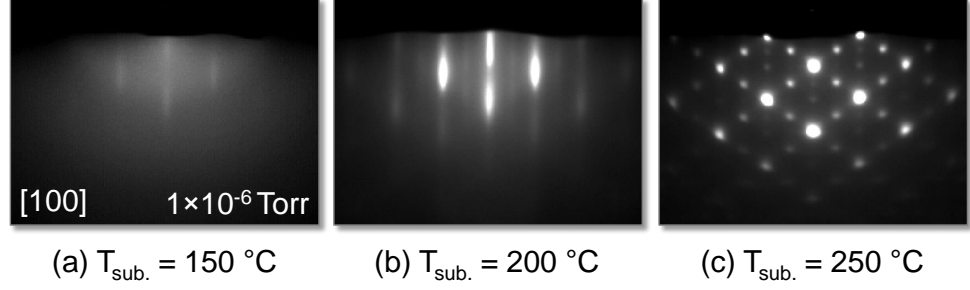


Figure 2.7: RHEED images of Zn_3P_2 films grown at a substrate temperature of (a) $150\text{ }^{\circ}\text{C}$, (b) $200\text{ }^{\circ}\text{C}$, and (c) $250\text{ }^{\circ}\text{C}$.

in direct conflict with the conventional growth conditions used for epitaxy of III-V phosphide materials. This discrepancy results from the difference in sticking coefficients between a group III element and Zn metal. By employing a stoichiometric flux, we were able to achieve a 2D growth regime which was not observed in previous epitaxial growth studies of Zn_3P_2 . Finally, RHEED patterns were used to determine the epitaxial orientation between the Zn_3P_2 epilayer and the GaAs substrate. The subsequent chapters will examine the properties of MBE grown Zn_3P_2 films in greater detail.

CHAPTER 3

Ex situ characterization of Zn_3P_2 epilayers

In addition to in situ RHEED measurements, the Zn_3P_2 epilayers were evaluated using a number of ex situ characterization techniques in order to verify the thin-film properties. The following sections describe our investigation of the bulk, surface, and growth interface morphology as well as the optical and electronic properties of pseudomorphic Zn_3P_2 films.

3.1 Growth rate and film morphology

Figure 3.1 displays the growth rate of Zn_3P_2 as a function of the substrate temperature for a BEP of $\sim 1 \times 10^{-6}$ Torr. The growth rate was calculated from the film thickness and the growth length. The film thickness was determined by profilometry. For substrate temperatures < 250 °C, the growth rate was typically $3 \sim 4$ nm min $^{-1}$. For temperatures > 250 °C, a rapid decline in the growth rate was observed, consistent with a decrease in the Zn sticking coefficient with increasing temperature. Analogous trends in growth rate have been reported for Zn-containing II-VI compounds, such as ZnSe and ZnS.^{65,66}

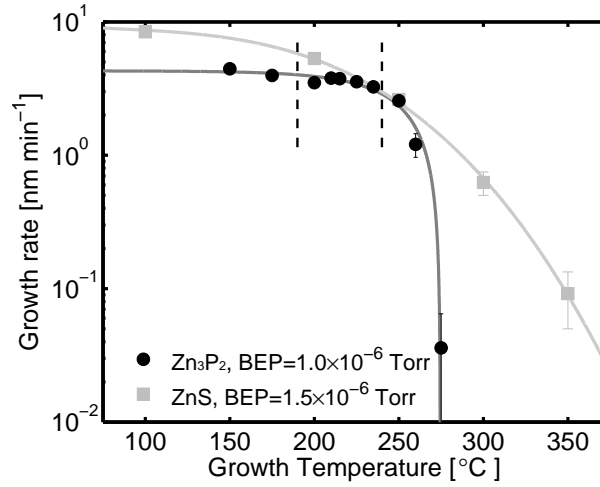


Figure 3.1: The growth rate of Zn_3P_2 as a function of substrate temperature for a given BEP of $\sim 1 \times 10^{-6}$ Torr. The growth rate data for ZnS is displayed for comparison.⁶⁶ The optimal growth window for Zn_3P_2 epitaxy was between 200 °C and 250 °C, indicated by the vertical dotted lines.

For comparison, the growth rate of ZnS produced by compound-source MBE under similar conditions is plotted along with the Zn_3P_2 data. The Zn_3P_2 growth rate decreased over a much narrower temperature range than has been reported for growth of ZnS, with the Zn_3P_2 growth completely terminated by 300 °C. This behavior is expected, since within the temperature range of interest Zn_3P_2 exhibits a much higher sublimation pressure than ZnS.^{15,67} To allow for Zn_3P_2 epitaxy, the observed rapid reduction in growth rate establishes a practical upper bound of ~ 250 °C on the substrate temperature.

The surface roughness of the as-grown films was verified by atomic force microscopy (AFM) topography imaging (Figure 3.2). Films that were grown between 200 ~ 235 °C had a typical RMS surface roughness of 0.6 nm, whereas films that were grown at < 175 °C or at > 250 °C were significantly rougher, having typical RMS roughness values of 2 nm and 10 nm, respectively. The AFM topography results, in addition to the growth rate and RHEED images, indicated that the growth of smooth, epitaxial Zn_3P_2 films was constrained

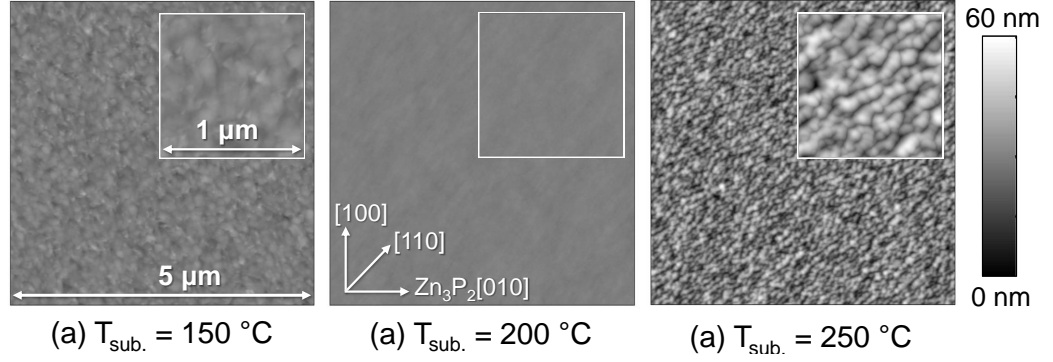


Figure 3.2: AFM topography images of the Zn_3P_2 surface for films grown at substrate temperatures of 150 °C, 200 °C, and 250 °C, respectively. The height scale bar applies to all of the AFM images.

to a narrow temperature window, specifically between 200 °C and 235 °C. To maximize the growth rate and to minimize the surface roughness, all subsequent growths were therefore performed at a substrate temperature of 200 °C.

The crystallinity and orientation of the Zn_3P_2 epilayers were further verified by high-resolution x-ray diffraction (HRXRD). Figure 3.3a displays symmetric HRXRD spectra of the GaAs(004) and Zn_3P_2 (008) reflections collected on increasing epilayer thicknesses. Clear Pendellösung oscillations were observed for film thicknesses of < 150 nm, indicating highly crystalline thin films. The Pendellösung oscillations arise from optical interference of the x-rays due to thin-film diffraction between the Zn_3P_2 epilayer surface and the Zn_3P_2 /GaAs interface. Table 3.1 reports the 2θ values of the Zn_3P_2 (008) peak maximum for all films. A shift in the Zn_3P_2 (008) peak position with respect to the bulk 2θ position was observed for film thicknesses up to ~ 150 nm.¹³ This shift represents an out-of-plane strain (ϵ_{\perp}) value of approximately 0.91%. For films > 150 nm in thickness, the XRD indicated a partial relaxation of ϵ . However for thicknesses up to 400 nm, 100% relaxation was not yet observed.

Figure 3.3b displays HRXRD double-axis rocking curves of the Zn_3P_2 (008) reflection for 70, 150 and 400 nm thick epilayers. The peak width of the rocking

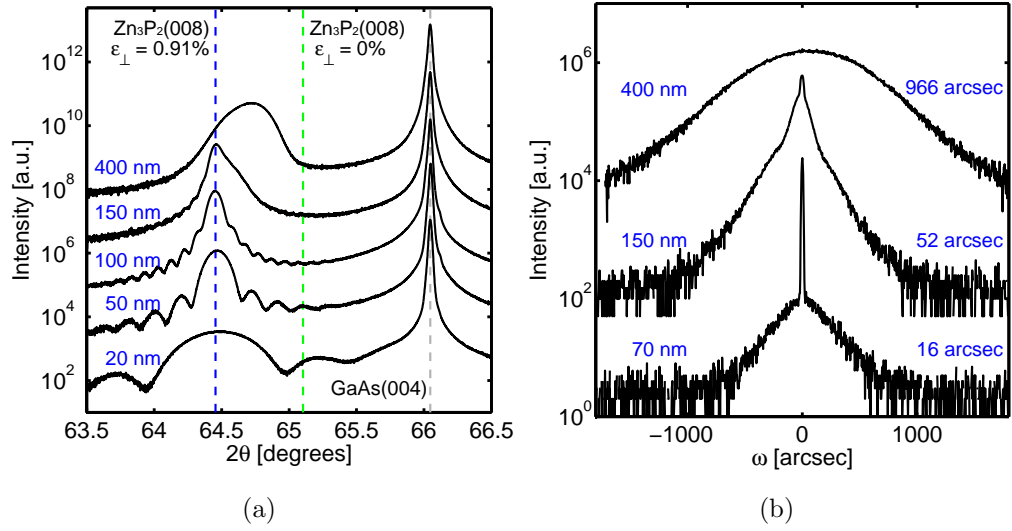


Figure 3.3: (a) Symmetric HRXRD scans of the Zn₃P₂(008) and GaAs(004) reflections for increasing Zn₃P₂ layer thickness. Vertical dashed lines represent the Zn₃P₂ peak positions for a fully strained and relaxed unit cell. (b) Rocking curves of the Zn₃P₂(008) reflection for film thicknesses of 70, 150, and 400 nm.

curve is considered a good indication of the crystallinity of the epilayer, with narrower widths equivalent to higher crystallinity. The rocking curve of the 70 nm film was composed of a narrow, coherent scattering peak with a FWHM of 16 arcsec, as well as a low-intensity diffuse scattering feature. A diffuse scattering peak is often observed in epitaxial layers and is associated with the presence of point defects.⁶⁸ A broadening in the rocking curve was observed for the 150 nm and 400 nm films, with the peak FWHM values increasing to 52 arcsec and 966 arcsec, respectively. This broadening is expected as the in-plane lattice parameter of the epilayer relaxes towards its native value. The relaxation process is normally accompanied by the creation of defects within the film.

Further evidence of pseudomorphic epilayer growth and strain relaxation was obtained from reciprocal space maps of the GaAs(113) and Zn₃P₂(206) asymmetric reflections that were collected for the 70 nm, 150 nm, and 400

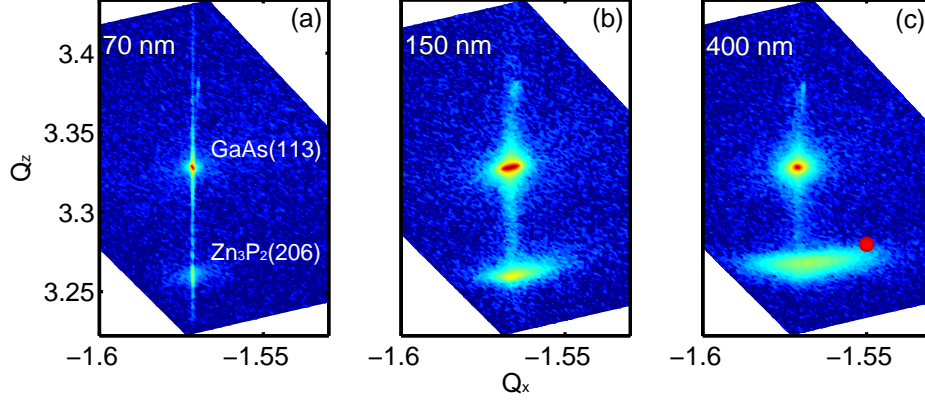


Figure 3.4: Reciprocal space maps of the $\text{Zn}_3\text{P}_2(206)$ and $\text{GaAs}(113)$ asymmetric reflections for Zn_3P_2 film thicknesses of (a) 70, (b) 150, and (c) 400 nm. The red dot in (c) represents the position of the fully relaxed $\text{Zn}_3\text{P}_2(206)$ reflection in reciprocal space.

nm thick films (Figure 3.4). A relaxation of the in-plane lattice parameter of the Zn_3P_2 epilayer was clearly evident by the comparison of the three measurements. The reciprocal space map of the 70 nm film showed a coherently strained Zn_3P_2 peak with respect to the GaAs substrate. The onset of relaxation was also observed for the 150 nm film, with a noticeable broadening of the film peak. Finally, the 400 nm film peak was further broadened in the direction of the calculated position for a fully relaxed film (red dot).

The microstructural changes incurred in the Zn_3P_2 epilayers upon relaxation were investigated using transmission electron microscopy (TEM). Figure 3.5 (a) and (b) display bright-field TEM images of the 50 and the 150 nm thick Zn_3P_2 epilayers, respectively. The 50 nm epilayer was effectively dislocation free, in agreement with both the coherent strain and extremely sharp rocking curves observed with HRXRD. On the other hand, a low concentration of crystalline defects was observed for the 150 nm thick film, further indicating the onset of strain relaxation. The red arrow in Figure 3.5 (b) points to the initiation of a threading dislocation in the epilayer. For a lattice mismatch of 1.3%, such dislocations are unavoidable for growth of thick films and will

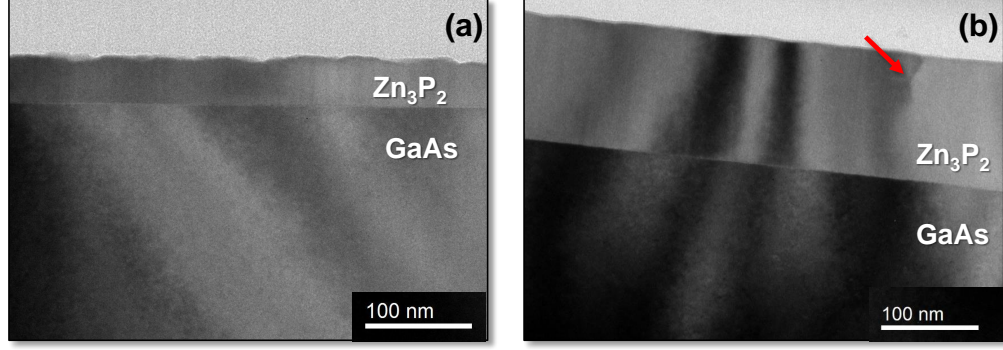


Figure 3.5: Bright field transmission electron micrographs of pseudomorphic Zn_3P_2 layers with thicknesses of (a) 50 nm and (b) 150 nm. The red arrow in (b) indicates the initiation of a threading dislocation due to the onset of strain relaxation.

likely degrade the electronic properties of the Zn_3P_2 to some extent.

3.2 Surface and interface characterization

In order to explore the properties of Zn_3P_2 epitaxy, high-resolution TEM images of the $\text{Zn}_3\text{P}_2/\text{GaAs}$ interface as well as scanning tunneling microscopy (STM) images and x-ray photoelectron spectra of the initial stages of Zn_3P_2 growth were collected. The TEM images were collected by Dr. Steve Rozeveld of the DOW Chemical Company and the STM images were collected on fresh Zn_3P_2 surfaces grown on GaAs by Dr. Seokmin Jeon.⁶⁹ More details of the STM characterization of Zn_3P_2 surfaces can be found in Dr. Jeon's Ph.D. thesis.⁷⁰

Figure 3.6 (a) shows a high-resolution TEM image of the $\text{Zn}_3\text{P}_2/\text{GaAs}(001)$ interface revealing crystalline, atomic order with (001) out-of-plane orientation for both the substrate and the epilayer. The out-of-plane bilayer spacing across the interface (Figure 3.6 (b)) was calculated by averaging the image contrast across the atomic layers and determining the distance.* Both the GaAs and

*The bilayer spacing was actually calibrate to the known lattice parameter of the GaAs

Zn_3P_2 bilayer spacings were in excellent agreement with the values calculated from the known lattice constants of each crystal structure (black lines). However, near the interface the bilayer spacing dramatically decreased. The smallest bilayer spacing observed matched the expected spacing of a GaP lattice which was under tensile strain due to the larger GaAs in-plane lattice constant (red dotted line). We believe this was evidence of a tetragonally-strained GaP interfacial layer between the GaAs substrate and the Zn_3P_2 epilayer. The thickness of the interfacial layer was difficult to accurately determine since changes in the bilayer spacing did not occur in discrete steps. However, the thickness appears to be on the order of $1 \sim 2$ nm. Finally, slight increases in the Zn_3P_2 and GaAs bilayer spacings directly adjacent to the interface were also observed (black arrows), indicating that the strained GaP layer caused some tetragonal compressive strain to occur in the adjacent epilayer and substrate.

The schematic diagram in Figure 3.7 displays STM images and our proposed film growth mechanism of Zn_3P_2 on the Ga-rich GaAs(001) using compound-source MBE. Initiation and growth occurs in several steps:

- (i) The GaAs(001) surface prepared by either atomic hydrogen cleaning or inert ion sputtering displays the Ga-rich GaAs(6×6) reconstruction.
- (ii) P_4 vapor decomposes and bonds to the surface Ga atoms changing the surface to a P-dimer terminated surface with either the $\beta 2(2\times4)$ or $\delta(2\times4)$ reconstructions. XPS indicates that these surface reconstructions are those of the GaP(001) surface based on the P 2*p* core-level shift.*
- (iii) The formation of a GaP surface layer was followed by the formation of featureless islands with random locations on the surface, indicating the growth of a P-rich ZnP_x ($x > 1$) amorphous overlayer.

bulk, far away from the $\text{Zn}_3\text{P}_2/\text{GaAs}$ interface

*DFT simulations performed by Dr. Jeon predicted that the replacement of subsurface As atoms by P atoms is an exothermic process, causing the formation of a GaP interfacial layer up to several monolayers thick.

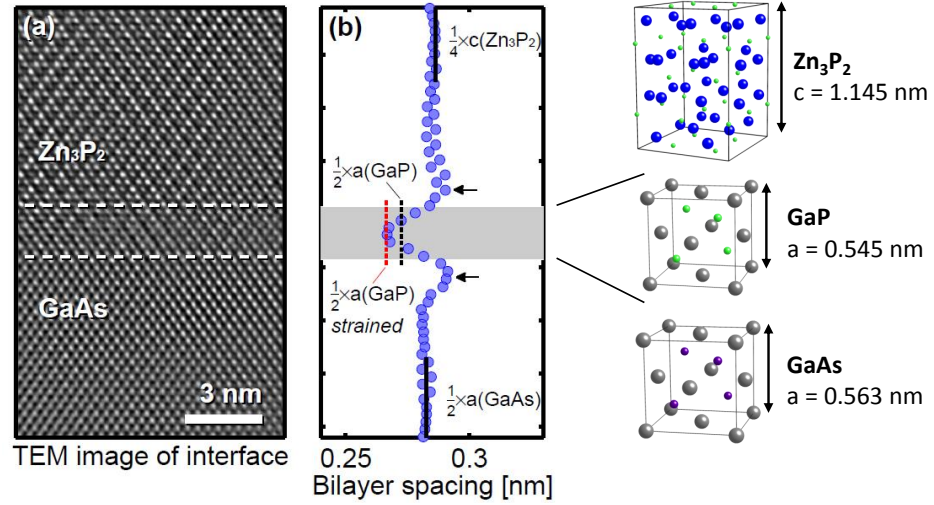


Figure 3.6: (a) High-resolution TEM image of the Zn₃P₂(001)/GaAs interface showing the presence of a GaP interfacial layer. (b) The calculated bilayer spacing across the interface. The black lines represent the bilayer spacing for the Zn₃P₂ and GaAs lattices. The black and red dotted lines represent the bilayer spacing for unstrained and strained GaP, respectively. The blue, gray, green, and violet spheres in the structure model represent Zn, Ga, P, and As atoms, respectively.

- (iv) Under further Zn and P flux, an epitaxial Zn₃P₂ film grows below the amorphous overlayer. However, the surface of the Zn₃P₂ epilayer remains covered by the amorphous overlayer with a total thickness of $\sim 1 \text{ nm}$.

Formation of the P-rich overlayer is likely due to the low sticking coefficient of Zn as compared to P on the Ga-rich GaAs(001)-(6 \times 6) surface, especially at low Zn₃P₂ coverage. Thus, the film growth is expected to be limited by Zn adsorption.

3.3 Optical properties

The optical properties of the epitaxial Zn₃P₂ films were determined using spectroscopic ellipsometry. Figure 3.8 displays the wavelength dependence of the

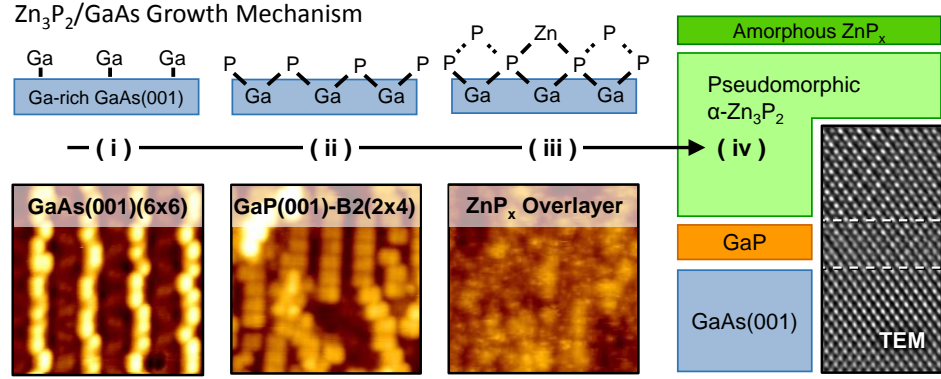


Figure 3.7: STM images of the initial stages of Zn_3P_2 growth on the Ga-rich GaAs(001) surface. A proposed model for the growth mechanism is also displayed.

index of refraction (n) and the extinction coefficient (k), as determined on a $7 \mu\text{m}$ thick Zn_3P_2 film. The measured values of k also allow determination of the energy dependence of the absorption coefficient ($\alpha = 4\pi\lambda/k$) of Zn_3P_2 . Figure 3.8 (b) and (c) display α^2 and $\alpha^{1/2}$ plotted versus photon energy, near the band edge of Zn_3P_2 . Extrapolation of the linear regions of the data yielded values for the direct and indirect band gaps of Zn_3P_2 of 1.52 eV and 1.39 eV, respectively. These values are in excellent agreement with those previously obtained on bulk Zn_3P_2 wafers.²² The effect of crystalline relaxation on the optical properties could not be directly observed since thin films ($< 3 \mu\text{m}$) of Zn_3P_2 were not fully absorbing near the band edge, which led to interference with the GaAs substrate. Our attempts to study the photoluminescence properties of Zn_3P_2 epilayers were also hindered by the luminescence of the GaAs substrate.

3.4 Electrical properties

The electrical properties of the Zn_3P_2 epilayers were determined using a combination of van der Pauw and Hall effect measurements. First, the intrinsic

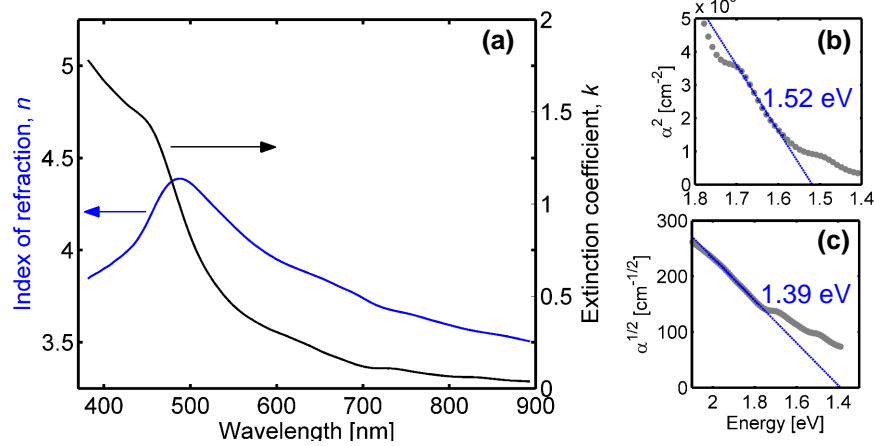


Figure 3.8: (a) The index of refraction (n) and extinction coefficient (k) values obtained by spectroscopic ellipsometry on a 7 μm thick Zn_3P_2 film. The linear extrapolation of (b) α^2 and (c) $\alpha^{1/2}$ as a function of energy resulted in direct and indirect transition values of 1.52 eV and 1.39 eV, respectively.

conductivity of as-grown Zn_3P_2 samples was studied, followed by attempts to incorporate extrinsic dopants with the goal of obtaining controllable p-type and n-type doping. All measurements were performed on 6 mm \times 6 mm samples with soldered In contacts.

3.4.1 Intrinsic doping

All of the as-grown Zn_3P_2 epilayers exhibited p-type conductivity. Figure 3.9 displays the resistivity, carrier concentration, and Hall mobility of Zn_3P_2 films as a function of epilayer thickness. The electrical measurement results are also tabulated in Table 3.1. The resistivity of the strained films was consistently on the order of 1 $\Omega\text{-cm}$, with corresponding hole concentrations of $> 1 \times 10^{17} \text{ cm}^{-3}$. A large increase in resistivity, and consequent decrease in the hole carrier concentration, was observed as the film thickness was increased above 150 nm. The Zn_3P_2 hole mobility also varied as a function of the epilayer thickness. For strained films, an increase in mobility was observed for increasing epilayer thicknesses between 20 and 150 nm. This increase is consistent with a decrease

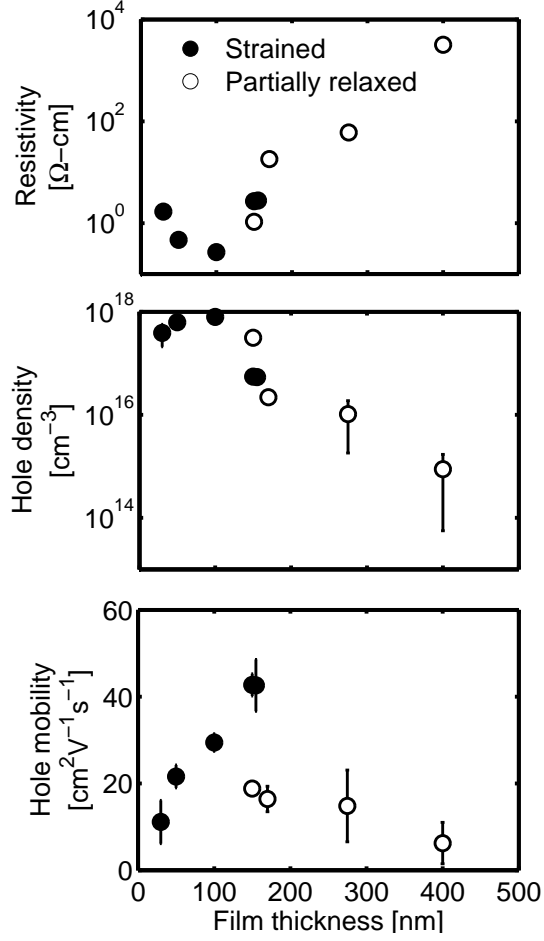


Figure 3.9: (a) Van der Pauw resistivity, (b) hole carrier concentration, and (c) hole mobility as a function of Zn_3P_2 epilayer thickness. The filled and open circles represent the data collected on strained and partially relaxed films, respectively.

in sensitivity to the interfacial defects between the Zn_3P_2 epilayer and the GaAs substrate. Similar trends have been observed for heteroepitaxial films of InAs on GaAs,^{71,72} InSb on GaAs,⁷³ and GaN on Al_2O_3 .⁷⁴ A maximum hole mobility of $\sim 45 \text{ cm}^2 \text{ V}^{-1} \text{ s}^{-1}$ was observed for a strained 150 nm thick film. This value is comparable to the maximum hole mobility reported for Zn_3P_2 single crystals that were grown by PVT.^{41,55} Upon partial relaxation of the films, the hole mobility decreased to $< 20 \text{ cm}^2 \text{ V}^{-1} \text{ s}^{-1}$, which is similar to values previously reported for polycrystalline Zn_3P_2 .²²

Theoretical³¹ and experimental⁴¹ studies have indicated that the dominant mechanism for intrinsic p-type conductivity in Zn_3P_2 is the presence of interstitial phosphorus atoms. This hypothesis agrees well with the observation of diffuse scattering peaks in the HRXRD rocking-curves of the pseudomorphic Zn_3P_2 films. The diffuse scattering is indicative of point defects within the epilayer, and in the case of Zn_3P_2 is consistent with the presence of interstitial P atoms. A high level of interstitial P is also consistent with the high concentration of hole carriers observed in strained films by the Hall effect. A subsequent decrease in the hole carrier concentration and the hole mobility upon film relaxation is consistent with the occurrence of misfit dislocations and threading dislocations within the epilayers, as observed by TEM. Dislocations have been suggested to act both as charged-carrier scattering and acceptor-compensating regions within a semiconductor material.⁷⁵ Therefore, a high density of threading dislocations within a partially relaxed Zn_3P_2 film would be expected to compensate the P interstitials that are responsible for the intrinsic p-type conductivity, and to thus decrease the effective hole mobility by 50% or more.

3.4.2 Extrinsic p-type doping

Controlled p-type doping is valuable for PV fabrication since it allows for improved device performance through both tuning of the built-in potential and incorporation of a back-surface field for passivation. Extrinsic p-type doping in Zn_3P_2 bulk crystals was previously reported using Ag impurities. In these studies, Ag films were deposited and then annealed into the bulk of the wafer at high temperatures ($> 400\text{ }^\circ\text{C}$), resulting in an increase in the acceptor density. Hole concentrations on the order of $\sim 1 \times 10^{17}\text{ cm}^{-3}$ were achieved using this method without a significant decrease in the hole mobility.

While diffusion doping has the merit of being simple and functional, it results in a doping profile that is difficult to control. Our goal was to incorporate extrinsic Ag atoms into the Zn_3P_2 lattice during normal epilayer

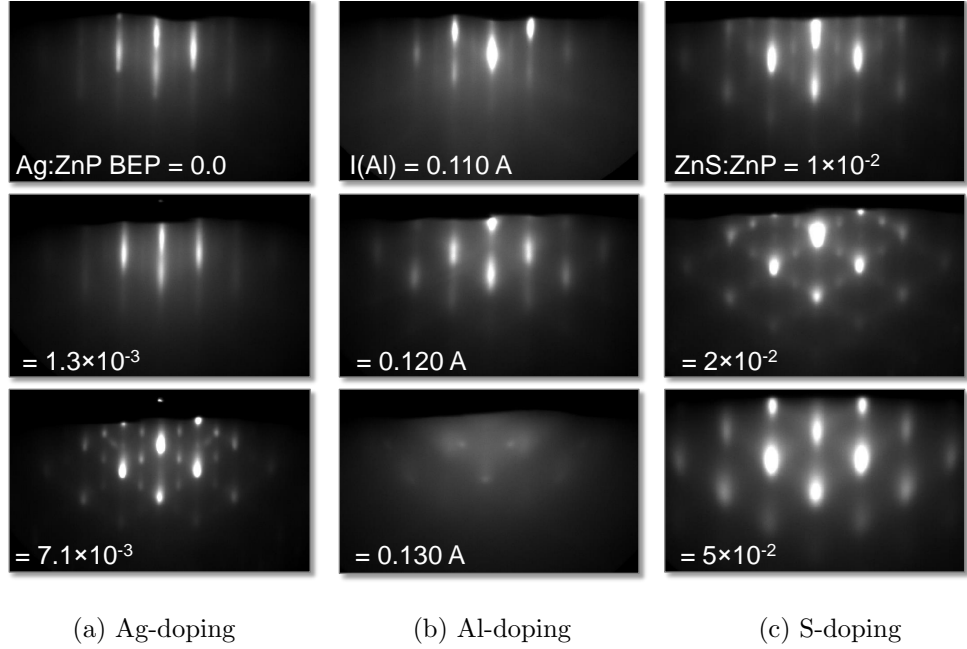


Figure 3.10: RHEED images of Zn_3P_2 epilayers for increasing impurity incorporation of (a) Ag, (b) Al, and (c) S. For all growth the Zn_3P_2 BEP and substrate temperatures were maintained at $\sim 1 \times 10^{-6}$ Torr and 200°C , respectively.

growth, resulting in controllable p-type doping levels throughout the film. Zn_3P_2 epilayers were grown with an increasing beam flux of Ag atoms. The flux was supplied using an additional Knudsen effusion source loaded with 6N Ag metal. Throughout all of the growths, the Zn_3P_2 beam flux was maintained at $\sim 1 \times 10^{-6}$ Torr and the ratio of the Ag to Zn_3P_2 flux is reported. RHEED images collected during the growth demonstrated that the incorporation of additional Ag at low ratios ($\text{Ag}:\text{Zn}_3\text{P}_2 < 5 \times 10^{-3}$) did not effect the orientation of the Zn_3P_2 growth (Figure 3.10a). However, at higher Ag fluxes, the surface of the film was roughened and a small amount of crystalline twinning was observed, indicating the onset of Ag-alloying or possibly phase separation.

The electronic properties of Ag-doped films as grown, and after a series of low-temperature vacuum anneals, were investigated using van der Pauw and

Hall effect measurements. Figure 3.11 displays (a) the thin-film resistivity as well as (b) the hole mobility of undoped, lightly Ag-doped, and heavily Ag-doped Zn_3P_2 layers as a function of the annealing temperature. In this case, the base annealing temperature of 200 °C is the growth temperature. Both of the Ag-doped films demonstrated resistivities an order of magnitude lower than the undoped film at 200 °C. Upon further heating, all three films resistivities decreased nearly linearly with the anneal temperature. We attribute the decrease in resistivity with annealing to the removal of charge scattering defects in the films. Such defects typically result in compensation of the active acceptor as well as decrease the effective carrier mobility. The removal of scattering defects is more clearly seen in the hole mobility as a function of temperature. Upon annealing, the hole mobility of all three films increased to a value of $10 \sim 20 \text{ cm}^2 \text{ V}^{-1} \text{ s}^{-1}$, with higher mobilities achieved for the Ag-doped samples. However, it seems that there is a diminishing return to the incorporation of Ag, since moderate beam ratios ($\text{Ag}:\text{Zn}_3\text{P}_2 \sim 1 \times 10^{-3}$) produced films with both lower resistivity and higher mobilities than high beam ratios ($\text{Ag}:\text{Zn}_3\text{P}_2 \sim 7 \times 10^{-3}$). This result is in agreement with the observation of twinning or phase separation occurring at higher Ag fluxes, which is likely responsible for the slight decrease in electronic quality.

3.4.3 Extrinsic n-type doping

Achieving reproducible n-type doping in Zn_3P_2 would allow for the formation of homojunction solar cells. As mentioned earlier, there is only one reported case of n-type doping in Zn_3P_2 .²⁸ However, due to the extremely high incorporation of excess Zn metal into the n-type films (17%!), these results are somewhat unconvincing and further study is necessary. We chose to investigate the formation of n-type conductivity via both cation replacement of Zn with Al and anion replacement of P with S. Similar to Ag doping, the impurity atoms were introduced into the Zn_3P_2 film growth through an additional effusion source. In this case, Al metal atoms were supplied using an electron-

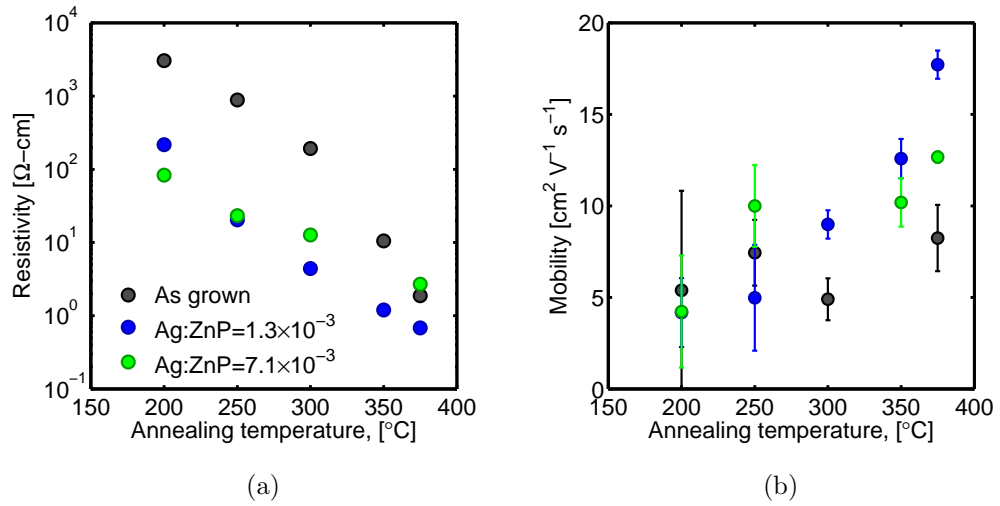


Figure 3.11: (a) Thin-film resistivity and (b) hole mobility of Ag-doped Zn_3P_2 epilayers as a function of annealing temperature.

beam evaporation source, whereas a ZnS compound effusion source was used to provide S atoms with an overpressure of Zn metal

RHEED images of Zn_3P_2 epilayers with increasing Al-dopant incorporation are displayed in Figure 3.10b. The Al flux was controlled by the electron-beam current since beam-equivalent pressure measurements were not possible.* At electron-beam currents ≥ 0.130 A, the growth immediately becomes amorphous, indicating excessive Al flux. However, at low electron beam currents, Al incorporation has little to no effect on the growth. Hall measurements collected on the crystalline $\text{Ag:Zn}_3\text{P}_2$ films showed clear compensation of the intrinsic p-type conductivity with a decrease in the hole carrier concentration. Unfortunately, the Al-doping concentration could not be increased enough to move past compensation into n-type conductivity before amorphous growth was observed.

RHEED images of Zn_3P_2 grown with ZnS flux for anion substitution are

*It seems that the electron-beam evaporator generates a small quantity of “loose” electrons in the vacuum chamber that perturb the operation of an ionization gauge causing extremely inaccurate readings, if any.

displayed in Figure 3.10c. The use of a ZnS beam flux is advantageous since the additional Zn flux helps prevent the creation of Zn vacancies in the Zn_3P_2 lattice, which are known to be compensating p-type defects.³¹ The Zn_3P_2 growth could be exposed to relatively high ZnS beam pressures before significant surface modification was observed. At low ZnS flux (BEP ratio $\leq 2 \times 10^{-2}$), only slight surface roughening was observed, but the RHEED pattern for the tetragonal unit cell was preserved. At $\sim 5 \times 10^{-2}$ BEP ratio, the Zn_3P_2 growth is effectively terminated, resulting in a ZnS RHEED pattern. The incorporation of S into the Zn_3P_2 lattice was verified with HRXRD symmetric scans (Figure 3.12). The S incorporation at low flux (BEP ratio = 1×10^{-2}) resulted in a decrease in the Zn_3P_2 lattice constant, indicated by a decrease in the tetragonal strain and therefore an increase in the 2θ value observed for pseudomorphic films. As the S flux is increased (BEP ratio = 2×10^{-2}), strain relaxation is observed in the film, likely due to the onset of phase separation of zinc-blende ZnS and tetragonal Zn_3P_2 . Finally, no Zn_3P_2 peak is observed for high S flux, indicating Zn_3P_2 growth did not occur. The indication that phase separation occurs for $\sim 2\%$ anion incorporation is in good agreement with the thermodynamic solubility limit of S in Zn_3P_2 .⁷⁶

3.5 Conclusions

We have shown the first demonstration of pseudomorphic growth of Zn_3P_2 on the GaAs(001) surface using compound-source molecular-beam epitaxy. Under MBE conditions, the optimal substrate temperature was between 200 °C and 235 °C. The growth window was constrained by amorphous deposition at low temperatures, and at higher temperatures by decreased growth rates and increased surface roughness. TEM and HRXRD studies confirmed that the epitaxial films grew pseudomorphically up to a critical thickness of ~ 150 nm. A growth mechanism was proposed base on interfacial TEM images and STM images showing the growth is initiated by phosphorus termination of GaAs

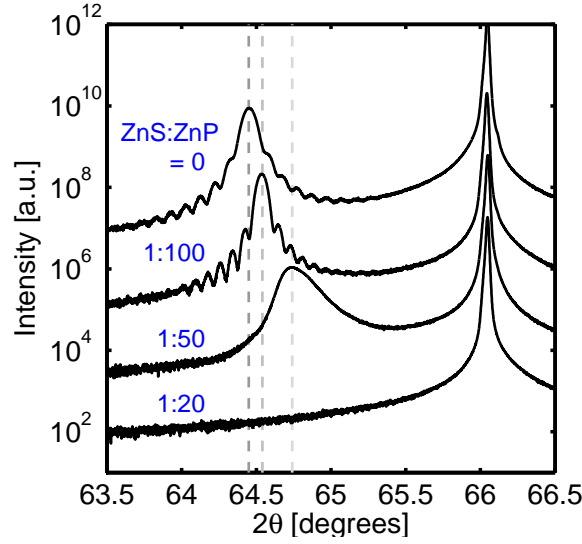


Figure 3.12: Symmetric HRXRD scans of Zn_3P_2 films grown with increasing sulfur incorporation.

forming an interfacial GaP layer, followed by an amorphous ZnP_x overlayer under which crystalline and oriented $\alpha\text{-Zn}_3\text{P}_2$ is precipitated.

Coherent growth allowed for further investigations into the effect of defects on the electronic properties of Zn_3P_2 thin films. Van der Pauw and Hall effect measurements showed that relaxation of the Zn_3P_2 lattice caused a significant decrease in the effective hole mobility and carrier density. However, below the critical film thickness, p-type mobilities of $> 40 \text{ cm}^2 \text{ V}^{-1} \text{ s}^{-1}$ were observed. These values are comparable to those reported for single-crystal Zn_3P_2 . The acceptor doping level in Zn_3P_2 could be modified by incorporation of extrinsic Ag impurities, whereas our attempts to produce n-type conductivity through anion or cation substitution were unsuccessful. However, S impurities could be introduced at high enough levels in Zn_3P_2 to result in alloying and a modification of the lattice parameter. The ability to tune the Zn_3P_2 lattice parameter could be useful in the future for controlling strain relaxation in Zn_3P_2 .

Table 3.1: Tabulated data for symmetric XRD, van der Pauw, and Hall effect measurements.

Thickness [nm]	Zn ₃ P ₂ (008) 2 θ [°]	Partially relaxed?	Resistivity [Ω -cm]	Hole density [cm ⁻³]	Hole mobility [cm ² V ⁻¹ s ⁻¹]
20	64.50(0)	no	1.68 \pm 0.06	(3.88 \pm 1.80) $\times 10^{17}$	11.0 \pm 5.0
50	64.46(3)	no	0.47 \pm 0.01	(6.22 \pm 0.70) $\times 10^{17}$	21.6 \pm 2.7
100	64.45(0)	no	0.27 \pm 0.01	(7.94 \pm 0.55) $\times 10^{17}$	29.4 \pm 2.0
150	64.46(1)	yes	1.06 \pm 0.03	(3.12 \pm 0.21) $\times 10^{17}$	18.8 \pm 1.4
155	64.45(0)	no	2.78 \pm 0.06	(5.36 \pm 0.82) $\times 10^{16}$	42.6 \pm 6.0
170	64.46(1)	yes	18.0 \pm 1.2	(2.19 \pm 0.45) $\times 10^{16}$	16.4 \pm 3.0
275	64.76(2)	yes	60.1 \pm 1.8	(1.03 \pm 0.85) $\times 10^{16}$	14.8 \pm 8.3
400	64.72(2)	yes	3190 \pm 46	(8.8 \pm 8.2) $\times 10^{14}$	6.2 \pm 4.8

CHAPTER 4

Growth and characterization of II-VI materials

A crucial phase of this work was to evaluate heterojunction partners for a Zn_3P_2 absorber. Of course, before it is possible to test the photovoltaic properties of a heterojunction partner, it is a prerequisite to be able to grow high quality thin films of that material. We initially chose a group of compound semiconductors that we believed had suitable electronic properties for making an emitter with Zn_3P_2 and then studied their growth by either compound-source MBE or sputter deposition. The following factors were taken into account before choosing potential emitter candidates:

- **Wide band gap:** As a general rule, it is recommended that the heterojunction partner have a band gap of at least 2.7 eV. Below this limit, absorption losses in the UV range become significant which result in decreased photocurrent.⁷⁷
- **Low electron affinity:** Zn_3P_2 has a relatively low electron affinity of ~ 3.6 eV.⁷⁸ It is important that the emitter for Zn_3P_2 has a similarly low electron affinity in order to avoid a large conduction band cliff at the

heterojunction interface. The effect of band alignment in heterojunction devices is discussed in more detail in chapter 5.

- **High n-type dopability:** n-type dopability is essential for fabricating a p-n junction with Zn_3P_2 . The doping in the n-type emitter layer will also play a role in the maximum achievable barrier height of the heterojunction device. Electron concentrations of $n > 1 \times 10^{17} \text{ cm}^{-3}$ are desirable.
- **High electron mobility:** In addition to n-type conductivity, it is also favorable for the emitter to have a high electron mobility ($\mu_e > 50 \text{ cm}^2 \text{ V}^{-1} \text{ s}^{-1}$) even at high doping levels. The electron mobility will dictate free carrier absorption at infrared wavelengths below the emitter band gap which can result in current losses in a final device.
- **Lattice match:** The highest quality heterojunction will result from an emitter with a lattice parameter that is closely matched with that of Zn_3P_2 . A small lattice mismatch often results in fewer interfacial defects which in theory results in lower interfacial recombination and improved carrier collection. Although this is not a prerequisite for a functional device, it is most certainly a favorable characteristic.
- **Facile growth:** We are interested in materials that have physical properties that are compatible with scalable thin-film deposition techniques. In particular, compounds that sublime congruently similar to Zn_3P_2 are desired. Compound sublimation allows for fast, large-scale processes like CSS or PVT.

After careful consideration of relevant optical and electronic properties we decided to focus our investigations on a small group of II-VI materials: ZnS , ZnSe , CdS , and ZnO . The following sections review our experience with their growth and characterization.

4.1 Zinc sulfide (ZnS) growth

Zinc-blende zinc sulfide (zb-ZnS) was considered an excellent candidate emitter for Zn_3P_2 . ZnS has a wide band gap of 3.68 eV, a reported χ of 3.9 eV,⁷⁹ and is comprised of earth-abundant elements. High levels of n-type doping in ZnS ($n > 1 \times 10^{18} \text{ cm}^{-3}$) have been achieved through non-equilibrium growth techniques that enable the incorporation of extrinsic dopants comprised of either group III or group VII elements.^{66,80,81} ZnS has also exhibited excellent surface passivation in heterojunctions with other semiconductors, including Si, Cu(In,Ga)Se₂, CdTe, and GaAs.^{82–86} Prior to this work, there have been no ZnS/ Zn_3P_2 heterojunction photovoltaic devices reported in the literature.

A considerable amount of effort was placed on understanding the growth and doping of ZnS epilayers. This knowledge greatly simplified the later growth studies on the other II-VI compounds of interest. While we are eventually interested in growing directly on Zn_3P_2 surfaces, for our initial growth studies we focused on growing on GaAs(001) for simplicity. Similar to Zn_3P_2 , ZnS sublimes congruently and thermal sublimation of the compound was previously found to result in high quality films.⁸⁷ The ZnS films were grown in the same UHV MBE chamber as the Zn_3P_2 films.⁶⁶ A standard Knudsen effusion cell loaded with pure ZnS (6N) was employed as a compound source. Epi-ready, semi-insulating GaAs(001) single crystal wafers (AXT) were used as an epitaxial substrate. The GaAs native oxide was removed prior to film growth by exposure to a flux of RF generated atomic hydrogen in the same fashion as described in subsection 2.4.1. The ZnS BEP was maintained at $\sim 1.5 \times 10^{-6}$ Torr (source temperature of 850 °C) throughout the entire study. The growth temperature was varied between 50 °C and 350 °C. RHEED was used extensively to characterize the orientation and surface morphology of the grown films. n-type doping of the ZnS films during epitaxial growth was accomplished by co-evaporation of pure Al metal (5N) using an additional electron-beam evaporator. The dopant incorporation was tuned by varying the e-beam current

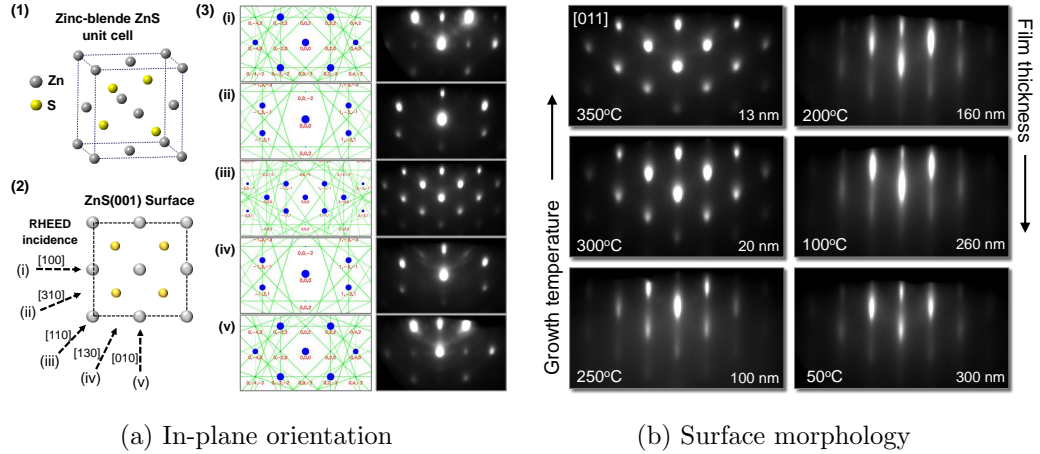


Figure 4.1: (a) Schematics of the (1) zinc-blende ZnS unit cell and (2) in-plane atomic arrangement of the ZnS(001) surface, as well as (3) RHEED patterns of the (001) surface along different zone axes compared with the equivalent electron diffraction simulations for the ZnS crystal structure. (b) RHEED images recorded along the $[011]$ zone axis of ZnS films grown at substrate temperatures ranging from 350 to 50 °C.

in the same manner as previously described for extrinsic doping of Zn_3P_2 in section 3.4.

ZnS epilayers with specular surfaces were achieved at growth temperatures ranging from 350 °C down to 50 °C despite a $> 4\%$ lattice mismatch with GaAs. AFM revealed an average RMS surface roughness of $< \pm 1$ nm for films greater than 200 nm in total thickness. The growth rate of ZnS as a function of substrate temperature was determined by both ellipsometry and profilometry measurements. There was excellent agreement between the two thickness measurement techniques and the ZnS growth rate was found to decrease rapidly for substrate temperatures > 250 °C (See Figure 3.1 in section 3.1). This trend can be attributed to a decrease in the Zn sticking coefficient with increasing temperature as was previously observed for ZnS growth on the Si(001) surface.⁸⁸ The growth rate was also found to increase linearly with the ZnS BEP for a given growth temperature.

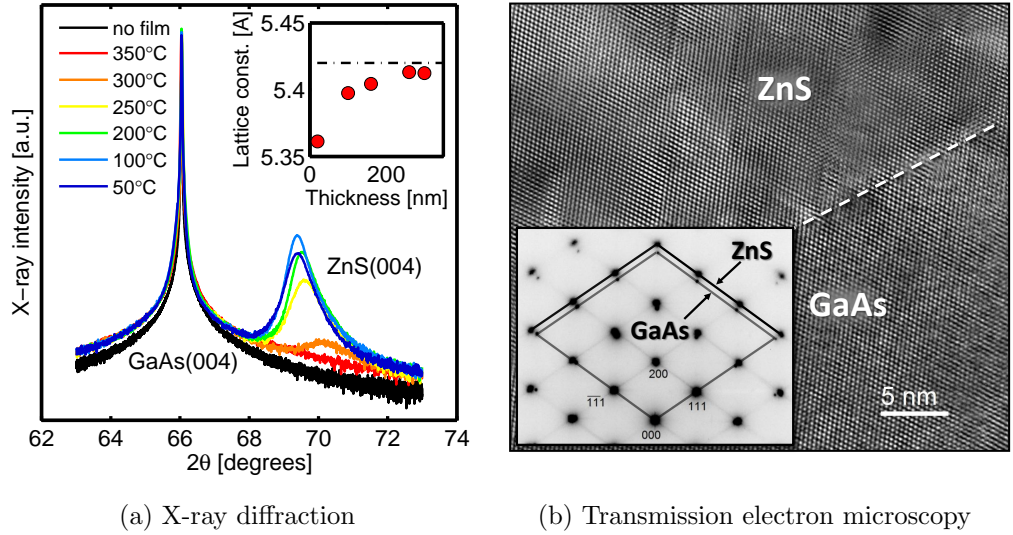


Figure 4.2: (a) HRXRD of the GaAs and ZnS (004) reflections for films of varying thicknesses and (b) a high-resolution transmission electron micrograph of the ZnS/GaAs interface.

Figure 4.1a displays RHEED images collected at various zone axes for a 13 nm thick ZnS film. For such thin films, the ZnS film displayed a considerable amount of surface roughness, likely resulting from an island growth mechanism at the initial stages of deposition. The roughness resulted in point diffraction patterns in the RHEED images. A comparison with simulated electron diffraction patterns verified that the films exhibited the zinc-blende crystal structure well aligned with the unit cell of the GaAs substrate perpendicular to the growth axis.⁶⁴ RHEED images collected along the $[011]$ zone axis of ZnS as a function of the growth temperature (and hence film thickness) are displayed in Figure 4.1b. The RHEED pattern was found to change quickly from spots to streaks, indicating a transition from a three-dimensional growth regime to a more favorable two-dimensional growth regime. The similarity of RHEED patterns obtained for a given film thickness grown at two different temperatures (not shown) suggests that the observed transition is primarily due to thickness rather than temperature.

Figure 4.2 displays (a) HRXRD of the GaAs (004) reflection for ZnS films of varying thicknesses and (b) a high-resolution TEM image of the ZnS/GaAs interface. From Figure 4.2a we observe a clear ZnS(004) reflection in addition to the GaAs diffraction peak. No other ZnS orientations were observed. From the 2θ position of the ZnS(004) peak, the out-of-plane ZnS lattice parameter was calculated and plotted as a function of epilayer thickness (see inset of Figure 4.2a). For very thin films, the ZnS lattice parameter is below the native value due to a small amount of tensile tetragonal strain. The lattice parameter was observed to increase with film thickness towards its relaxed value of 5.420 Å. This is an indication of the rapid film relaxation that can be considered complete after ~ 250 nm. From the TEM image of the interface in Figure 4.2b, one can see the clear presence of interface defects as well as extra half-planes. Stacking faults and crystal twinning were also observed within the bulk of the ZnS film. However, these defects and dislocations are expected considering the lattice mismatch between GaAs and ZnS of roughly 4%. The inset of Figure 4.2b shows an SAED pattern collected at the ZnS/GaAs epitaxial interface. The SAED pattern shows a smaller lattice parameter for the ZnS film as compared to the GaAs, again indicative of immediate lattice relaxation. In addition, a $\sim 1^\circ$ tilt in the ZnS(001) orientation was observed with respect to the GaAs(001) crystal direction. The tilt is likely a growth mechanism for compensating the large lattice mismatch mentioned earlier. This tilt mechanism appears to be common for lattice mismatched growth of II-VI compounds and was previously observed for ZnSe epilayers grown on Ge(001) substrates by MBE.⁸⁹

The electronic properties of Al-doped ZnS films were studied using van der Pauw and Hall effect measurements. These measurements were only possible for heavily-doped samples ($n > 1 \times 10^{17} \text{ cm}^{-3}$). For lower doping levels it was very difficult to make reliable ohmic contact to the films, a common problem when working with wide band gap semiconductors. Figure 4.3a compares the resistivities and dopant concentrations obtained in this work with those from

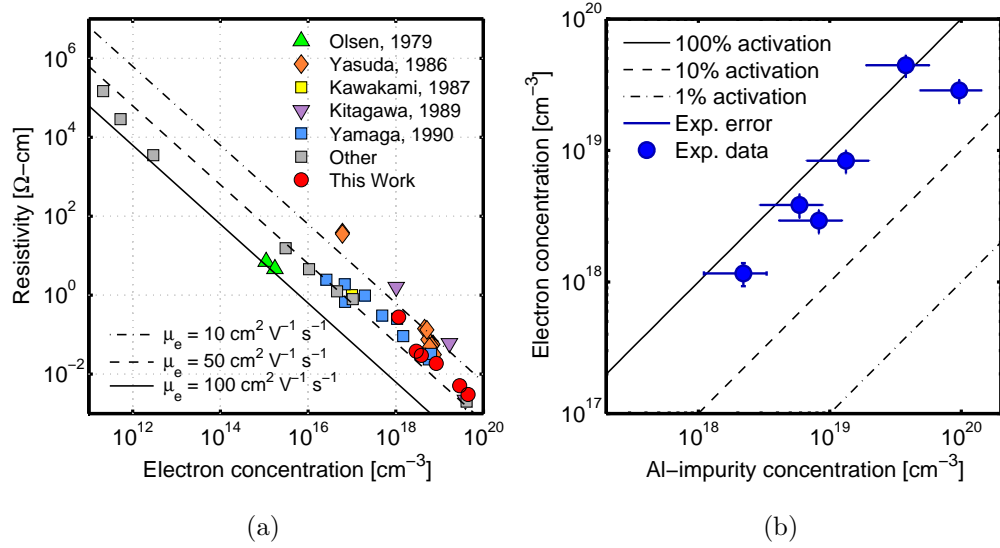


Figure 4.3: (a) van der Pauw resistivity vs. Hall electron concentration for Al-doped ZnS films and (b) a comparison of the measured Hall electron concentration and the Al-impurity concentration determined by SIMS analysis.

previous doping studies involving MBE, MOCVD, and MOPVE growth techniques.^{80,81,87,90} The highest electron concentration we achieved was $4.5 \times 10^{19} \text{ cm}^{-3}$, corresponding to a film resistivity of $0.003 \text{ } \Omega\text{-cm}$ and electron mobility of $46 \text{ cm}^2 \text{ V}^{-1} \text{ s}^{-1}$. Slightly higher mobilities ($\sim 55 \text{ cm}^2 \text{ V}^{-1} \text{ s}^{-1}$) were achieved at lower dopant concentrations. Our results compare well with the previous work, with the highest previously reported electron concentration being $3.9 \times 10^{19} \text{ cm}^{-3}$ ($\rho = 0.002 \text{ } \Omega\text{-cm}$). At these doping levels, sheet resistances of $< 100 \text{ } \Omega/\square$ can be achieved for film thicknesses of $100 \sim 200 \text{ nm}$. The actual Al impurity concentration incorporated in the ZnS films was determined by secondary-ion mass spectrometry (SIMS) analysis and is compared to the measured electron concentration in Figure 4.3b. Al-dopant activation was observed to range from roughly $25 \sim 100\%$. It appears that the low growth temperatures accessible using compound-source MBE help to avoid the issue of self-compensation commonly encountered for extrinsic doping of wide band gap II-VI compounds.⁹¹

4.2 Zinc selenide (ZnSe) growth

ZnSe was the second emitter candidate we focused on. ZnSe has a band gap of 2.7 eV (near the lower limit of suitable values), a reported χ of 4.09 eV, and obtainable μ_e of $100 \sim 300 \text{ cm}^2 \text{ V}^{-1} \text{ s}^{-1}$. The growth and doping of ZnSe epilayers on GaAs(001) is very well established in the literature.^{65,92,93} In a similar approach to that used with ZnS, we chose to use thermal sublimation of a compound source to deposit ZnSe, since this approach was previously reported to work well.⁹⁴ The same procedures for growing ZnS were used for the initial ZnSe growth studies. Again, atomic-hydrogen treated GaAs(001) substrates were employed as an epitaxial template. The ZnSe BEP was maintained at 1.5×10^{-6} Torr (source temperature of 825 °C) throughout the entire study while the growth temperature was varied between 100 °C and 350 °C.

HRXRD symmetric scans of the ZnSe(004) and GaAs(004) peaks for 200 nm and 300 nm thick ZnSe epilayers grown directly on the GaAs(001) surface are displayed in Figure 4.4. A scan of the Zn_3P_2 (008) peak as well as for bare GaAs are also included for comparison. The XRD confirmed that that ZnSe and GaAs heteroepitaxial relationship was $\text{ZnSe}(001) \parallel \text{GaAs}(001)$, as expected. No other ZnSe orientations were observed. The 2θ peak position of both ZnSe samples were shifted lower in value with respect to the native lattice position, indicating the presence of tetragonal strain. The additional presence of Pendellösung oscillations in the 200 nm film is additional evidence that for thin samples the ZnSe grows pseudomorphically on the GaAs. Between 200 and 300 nm there is some relaxation that occurs, as evidenced by the broadening of the 300 nm sample's peak.

Figure 4.5 displays a cross sectional TEM image and SAED pattern of a 300 nm thick ZnSe epilayer. The TEM image reveals a sharp ZnSe/GaAs(001) interface as well as a smooth ZnSe surface. The bulk of the ZnSe film appeared to have a “mottled” internal defect structure. The mottled structure has been observed before in CdS films created by either chemical-bath deposition

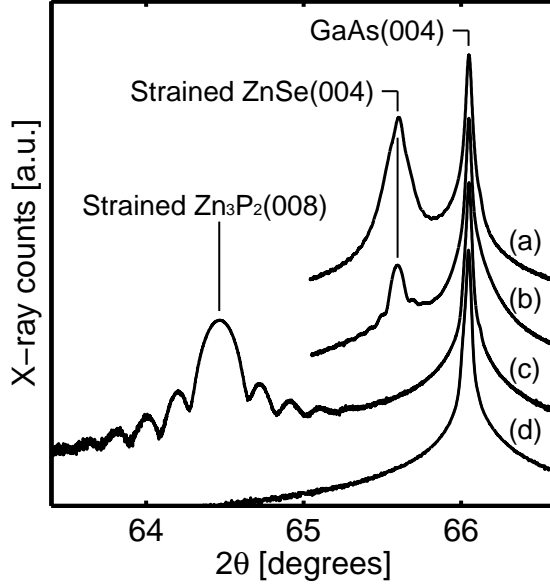


Figure 4.4: HRXRD of the (a) 300 nm and (b) 200 nm thick strained ZnSe epilayers grown on GaAs(001) and for comparison (c) Zn₃P₂ grown on GaAs(001) as well as (d) bare GaAs(001).

(CBD) or physical-vapor deposition (PVD).⁹⁵ There appears to be a very high concentration of stacking faults and other crystalline defects in the ZnSe films. However, SAED patterns of the ZnSe film showed that despite the very high defect concentration the film was highly oriented and single crystalline.

Figure 4.6 compares the resistivity and dopant concentrations obtained from van der Pauw and Hall effect measurements obtained on Al-doped ZnSe films with thicknesses ranging from 200 ~ 600 nm. A comparison is made with previous doping studies of PVT and melt-grown ZnSe single crystals and thin films grown by MBE and MOCVD techniques.^{96–101} Without extrinsic dopants, the as-grown ZnSe films were extremely resistive ($\rho > 1 \times 10^8 \Omega\text{-cm}$) and therefore could not be measured. Ohmic contacts could be made to Al-doped films if the electron concentration was $\geq 1 \times 10^{17} \text{ cm}^{-3}$. The highest electron concentration achieved in the current work was $3 \times 10^{19} \text{ cm}^{-3}$, corresponding to a film resistivity of 0.001 $\Omega\text{-cm}$ and electron mobility of 140 $\text{cm}^2 \text{ V}^{-1} \text{ s}^{-1}$. Our results compare well with previous investigations, with the

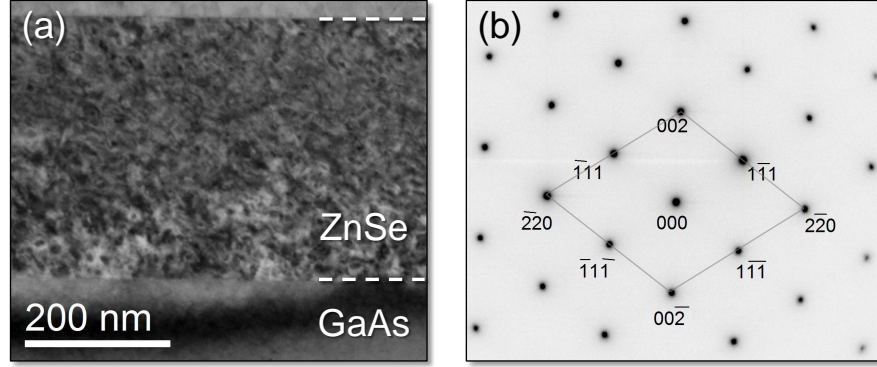


Figure 4.5: (a) Transmission electron micrograph and (b) selected-area electron diffraction of a pseudomorphic 300 nm ZnSe film grown directly on a GaAs(001) substrate.

highest reported electron concentration being $8 \times 10^{19} \text{ cm}^{-3}$ ($\rho = 0.0007 \text{ } \Omega\text{-cm}$). Higher mobilities ($\sim 200 \text{ cm}^2 \text{ V}^{-1} \text{ s}^{-1}$) were achieved at lower dopant concentrations. There was also some evidence that the film thickness affected the mobility, where higher mobilities were observed for thinner films ($< 300 \text{ nm}$) where strain relaxation had not yet occurred.

4.3 Cadmium sulfide (CdS) growth

Wurtzite cadmium sulfide (w-CdS) is already used extensively in commercial PV devices and has proven to be a stable and efficient emitter in thin-film applications implementing CdTe and CIGS absorbers. The positive attributes of CdS are its passivating properties and its high n-type dopability over a wide range of carrier concentrations ($10^{15} \sim 10^{19} \text{ cm}^{-3}$). However, CdS has a slightly too narrow band gap of 2.4 eV and a larger electron affinity of 4.5 eV as compared to ZnSe and ZnS. The most popular method for forming CdS films is via chemical-bath deposition. However, CdS films of reasonable electronic quality have also been grown using thermal evaporation. Similar to our procedure for ZnS and ZnSe, CdS films were grown by compound-source MBE. Little effort was made to optimize the growth conditions for CdS or explore extrinsic

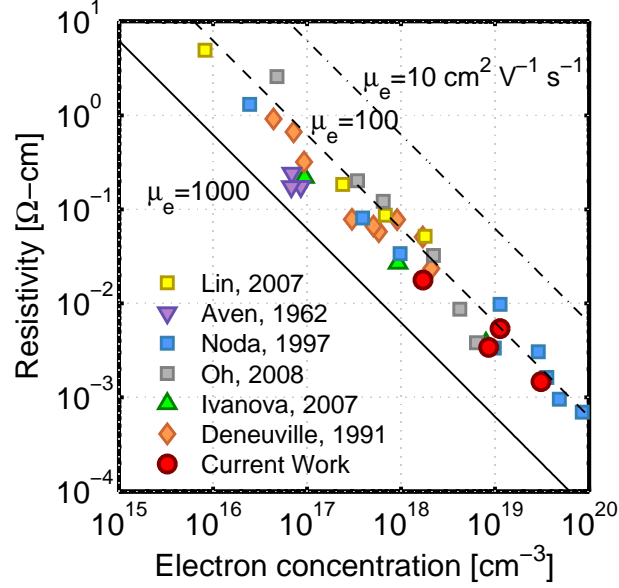


Figure 4.6: Van der Pauw resistivity versus Hall carrier concentration measured on Al:ZnSe epilayers. A comparison with previous literature studies is made.^{96–101} The lines represent the ideal relationship between resistivity and carrier concentration for a given electron mobility.

dopants since it was unlikely that the n-type material would prove a good emitter for Zn_3P_2 devices.* Nevertheless, crystalline CdS films with (0001) orientation were grown using the compound-source technique. These films were sufficient for performing the band alignment measurements discussed in chapter 5.

4.4 Zinc oxide (ZnO) sputter deposition

The final material we studied was wurtzite zinc oxide (w-ZnO), which has a large band gap of 3.4 eV, an electron affinity of 4.6 eV, and is easily doped n-type with attainable electron concentrations of $n > 1 \times 10^{20} \text{ cm}^{-3}$. Unlike the previous growth studies, ZnO films were grown in a separate vacuum chamber

*The details of exactly why the CdS/ Zn_3P_2 heterojunction is non-ideal for PV application will be stated more clearly in chapter 5.

by RF magnetron sputter deposition. A sintered ZnO target was used as a source material. Various sputtering conditions were explored in order to minimize the electron carrier concentration in the ZnO. Our goal was to avoid high doping levels since they were deleterious to the XPS measurements that are discussed in chapter 5. The highest resistivity films were obtained for room temperature deposition using a 10% O₂/Ar gas mixture at 10 mTorr. ZnO mobilities were too low to measure by Hall effect, but the films had typical resistivities on the order of 10⁻² Ω-cm. The ZnO films were also polycrystalline with a strongly preferred (0001) orientation.

4.5 Alternative: Zn_xMg_{1-x}S_ySe_{1-y} quaternary alloy

As stated previously, we chose the above II-VI materials as emitters for a Zn₃P₂ photovoltaic device in order to optimize several parameters such as conduction-band offset, band gap, surface passivation, etc. The simplicity of binary semiconductor growth from a compound source is also advantageous from an industrial perspective. While the mentioned materials are potentially very good matches for Zn₃P₂, any conduction-band offset between the emitter and absorber materials represents a direct loss in V_{oc} . Lattice mismatch between the two semiconductor compounds may also result in losses in device performance. Improving these values could nominally improve the performance of a heterojunction device.

At the risk of complicating the growth, we believe that quaternary alloys of Zn, Mg, S, and Se, with the correct stoichiometry, could produce a material that is both electron affinity and lattice matched to Zn₃P₂. Even though we do not intend to experimentally explore this quaternary material, we would like to mention its potential as an emitter material for advance Zn₃P₂ devices. Approximate calculations of lattice parameter, electron affinity, and energy

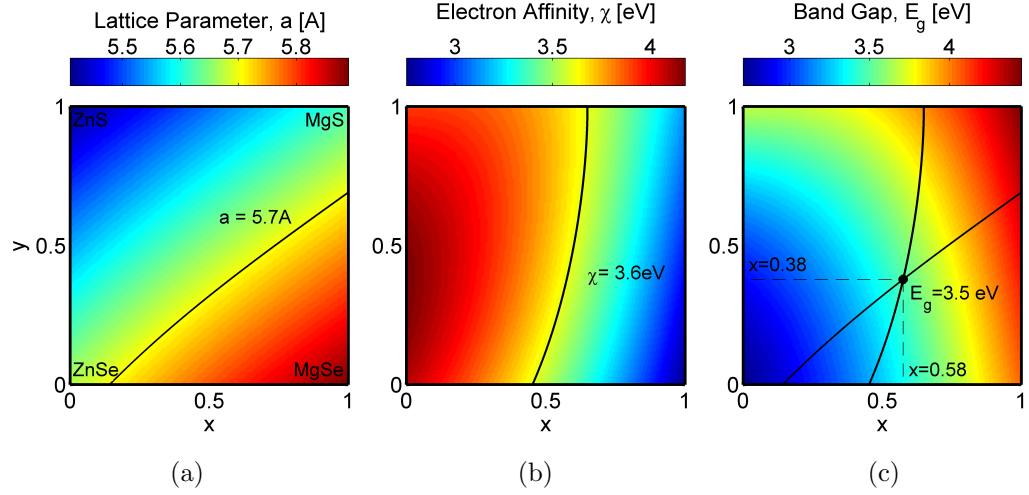


Figure 4.7: (a) Lattice parameter, (b) electron affinity, and (c) band gap calculated for the $\text{Zn}_x\text{Mg}_{1-x}\text{S}_y\text{Se}_{1-y}$ quaternary alloys. Black curves represent the compositions where lattice parameter and electron affinity are matched to Zn_3P_2 . In (c), the intersection of the curves shows the composition where the alloy is both lattice and electron affinity matched to Zn_3P_2 .

band gap for the full composition range of the quaternary alloy have been performed, given experimental and calculated bowing parameters for each of the four ternary sub-systems (i.e. Zn-Mg-S, Zn-Mg-Se, Zn-S-Se, Mg-S-Se).^{102–104} The details of the calculation can be found in section A.2. The results are displayed in Figure 4.7 and show that both lattice and electron affinity match to Zn_3P_2 is possible for an alloy with composition $\text{Zn}_{0.42}\text{Mg}_{0.58}\text{S}_{0.38}\text{Se}_{0.62}$. At this composition, the energy band gap is found to be large at 3.5 eV. Albeit it is likely that the actual electron affinity at the quaternary/ Zn_3P_2 interface will deviate from the nominal value, it would be possible to further tune the composition until experimentally matched.

4.6 Conclusions

We have demonstrated the growth of several II-VI compounds that are po-

tential n-type emitters for a heterojunction Zn_3P_2 photovoltaic device. Special attention was given to understanding the growth and doping of ZnS and ZnSe , since these materials demonstrate the most favorable properties for PV applications. The idea of an alternative $\text{Zn}_x\text{Mg}_{1-x}\text{S}_y\text{Se}_{1-y}$ quaternary emitter material was also theoretically investigated, demonstrating that it would be possible to attain a wide band gap emitter that is nominally lattice matched *and* electron affinity matched to Zn_3P_2 . However, this material system has not yet been pursued experimentally. The subsequent chapter will focus on evaluating the above II-VI materials as heterojunction partners with Zn_3P_2 .

Band energetics of II-VI/ Zn_3P_2 heterostructures

5.1 Introduction to energy-band alignments

There are many factors that determine the photovoltaic properties of a heterojunction solar cell. Arguably the most important of these is the energy-band alignment between the absorber material and the emitter. The V_{oc} of a PV device is dominated by the obtainable barrier height. The barrier height is in return dependent on a number of factors including the alignment between the conduction and valence bands of the two heterojunction materials, doping in the emitter and absorber layers, and recombination of carriers at the surface and in the bulk. Not only does the band alignment affect the barrier height, but it also affects carrier transport and separation at the interface. The sections below review the most common theoretical models and experimental methods for calculating or measuring a heterojunction alignment, following which we will discuss our own route to determining the band alignment of II-VI/ Zn_3P_2 heterojunctions.

5.1.1 Anderson energy-band alignment

The Anderson energy-band alignment theory, also known as the “electron affinity” or EA model, is the simplest method for estimating the band alignment of two semiconductor materials.¹⁰⁵ The basic assumption of this model is that the conduction-band discontinuity (ΔE_C) of a heterojunction is simply the difference in electron affinities (χ) of the two semiconductors of interest. In other words, for a heterojunction between semiconductors A and B , the ΔE_C is given as,

$$\Delta E_C(A/B) = \chi_A - \chi_B. \quad (5.1)$$

The convention used here is that semiconductor A is grown on top of semiconductor B . Figure 5.1 displays Anderson band diagrams for a typical p-n junction with a wide band gap p-type layer and narrow band gap n-type layer under (a) isolated and (b) equilibrium conditions. This model tends to work relatively well for simple systems comprised of like materials. However, there are a large number of cases described in the literature where this basic assumption fails to accurately predict heterojunction band discontinuities. In particular, Anderson band alignment theory fails to take into account deviations in the band discontinuities due to a number of non-idealities including: interfacial dipoles, interfacial defects, lattice strain, and impurities.¹⁰⁶

5.1.2 Effective dipole model

As a first-order correction to the Anderson band alignment model, Ruan and Ching proposed the effective dipole model.¹⁰⁷ Their model generally results in improved ΔE_V predictions for a large number of common heterojunctions. Assuming defect-free interfaces, the model calculates the effective interfacial dipole resulting from charge transfer from the higher valence-band material in the heterojunction to the lower valence-band material, and thus predicts the extent to which the band offsets are modified. For a heterojunction consisting

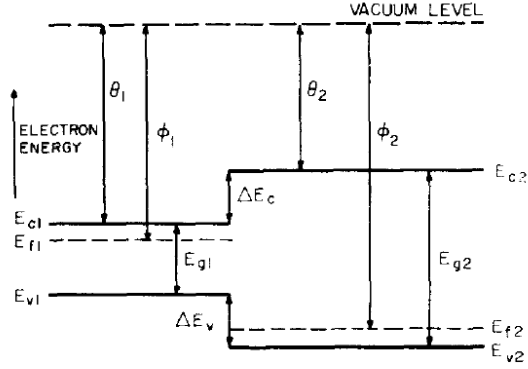


FIG. 1. Energy-band diagram for two isolated semiconductors in which space-charge neutrality is assumed to exist in every region.

(a)

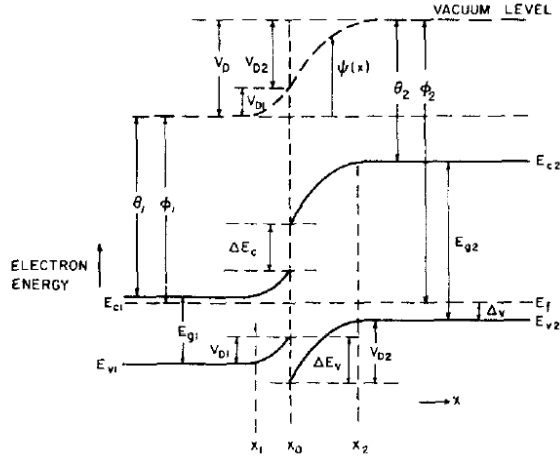


FIG. 2. Energy-band diagram of *n-p* heterojunction at equilibrium.

(b)

Figure 5.1: Original Anderson energy-band diagrams for two semiconductors under (a) isolated and (b) equilibrium conditions. In this case, Anderson used the symbols θ_1 and θ_2 to represent the electron affinities of semiconductors 1 and 2, respectively.

of semiconductors A and B, the following self-consistent equation is solved iteratively to determine the value of $\Delta\phi$, the deviation of the ΔE_v from the ideal value predicted by Anderson band alignment theory (i.e. $\Delta E_v(\text{dipole}) =$

$\Delta E_V(\text{Anderson}) - \Delta\phi$:

$$\Delta\phi = 0.15e(\epsilon_o\epsilon_B\pi^2)^{-1} \times \dots$$

$$\left[1 + \epsilon_B\epsilon_A^{-1} \sum_{l=1}^n k_l (1 - \eta_l^{-1} \arctan(\eta_l)) \left(\sum_{l=1}^n k_l (\eta_l^{-1} \arctan(\eta_l) - \eta_{o,l}^{-1} \arctan(\eta_{o,l})) \right)^{-1} \right] \times \sum_{l=1}^n k_l (1 - \eta_l^{-1} \arctan(\eta_l)), \quad (5.2)$$

where the variables k_l , η_l , and $\eta_{l,o}$ are defined as follows,

$$k_l = (2m_l^* \hbar^{-2} \Delta E_{Vo,l})^{1/2}, \quad (5.3)$$

$$\eta_l = \left[\frac{5}{3} \Delta E_{Vo,l} (\Delta E_{o,l} + e\Delta\phi)^{-1} \right]^{1/2}, \quad (5.4)$$

$$\eta_{l,o} = \left[\frac{5}{3} \Delta E_{Vo,l} (\Delta E_{o,l})^{-1} \right]^{1/2}, \quad (5.5)$$

and the initial valence-band offset (ΔE_{Vo}) is calculated from Anderson theory as follows,

$$\Delta E_{Vo} = (E_{g,B} + \chi_B) - (E_{g,A} + \chi_A). \quad (5.6)$$

In the case where the valence region is composed of multiple bands with different energy levels due to spin-orbit splitting or crystal-field splitting, the subscript l is added. For example, Zn_3P_2 exhibits three degenerate bands which vary in energy from the valence-band maximum ($l = 1$) due to crystal-field splitting (Δ_{CF} , $l = 2$) and spin-orbit splitting (Δ_{SO} , $l = 3$). Therefore,

$$\Delta E_{Vo,1} = (E_{g,B} + \chi_B) - (E_{g,A} + \chi_A), \quad (5.7)$$

$$\Delta E_{Vo,2} = \Delta E_{Vo,1} - \Delta_{CF}, \quad (5.8)$$

$$\Delta E_{Vo,3} = \Delta E_{Vo,1} - \Delta_{SO}. \quad (5.9)$$

Finally, the initial barrier height for tunneling of electrons from one valence band to the other is given by the difference in the conduction-band minimum

of semiconductor B to one of the valence bands of semiconductor A,

$$\Delta E_{o,l} = E_{g,B} - \Delta E_{Vo,l}. \quad (5.10)$$

A qualitative illustration of the (a) initial and (b) modified band alignment between narrow band gap semiconductor A and wide band gap semiconductor B is displayed in Figure 5.2. An induced dipole at the interface typically results in a decrease in the valence-band offset as electrons from the higher valence band material tunnel into the lower valence band material. This causes the theory to be very sensitive to the value of the hole effective mass of the higher valence band material. Furthermore, any additional disturbances local to the interface, such as interfacial defects, are not included in the model but in reality will modify the induced dipole. Hence, predictions are more accurate for low lattice mismatch heterojunctions.

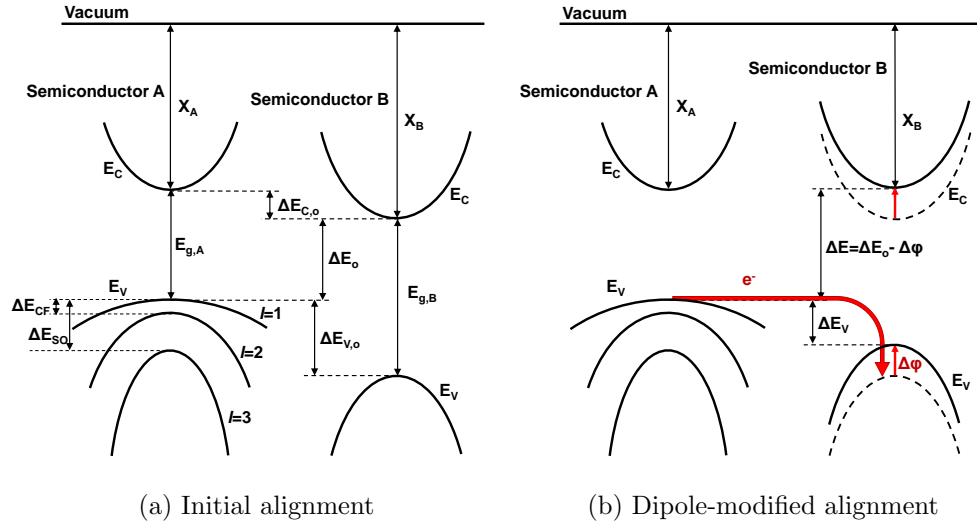


Figure 5.2: A schematic of the effective dipole calculation and associated variables as proposed by Ruan and Ching.¹⁰⁷

5.1.3 Advanced methods

The use of more detailed calculations to determine the valence-band offset between two materials has been proposed. The most common method is to use density functional theory (DFT) to calculate the difference in average electrostatic potentials between the two semiconductor materials.¹⁰⁶ There are two general approaches to DFT models for band alignment prediction, the major assumption being whether or not the system is “intrinsic.” An intrinsic alignment is defined as one that depends only on the bulk electronic properties of the heterojunction materials. For non-intrinsic systems, a detailed understanding of the atomic ordering at the interface is necessary.^{106,108} The number of possible atomic arrangements it may be necessary to explore can result in a substantial computational expense. One example of an intrinsic theory is the universal hydrogen energy model, which assumes that dissolved H atoms that exist in every material dominate the bulk energy alignment.¹⁰⁹ Therefore, if one calculates the energy level of a H atom with respect to the valence band position within the bulk lattices of two different materials, one can then equate those values to determine the ΔE_V . This technique has been used to explore a number of heterojunction systems, including some specific examples involving Zn_3P_2 .¹¹⁰

5.2 Experimental determination of ΔE_V and ΔE_C

To understand the fundamental limitations on the attainable barrier heights of Zn_3P_2 heterojunction solar cells, we experimentally determined the band alignment of heterovalent interfaces composed of n-type II-VI semiconductors grown on the $\text{Zn}_3\text{P}_2(001)$ surface. As mentioned earlier, we are specifically interested in ZnS, ZnSe, CdS, and ZnO emitters because these materials are commonly employed in photovoltaic devices and have already been used in

conjunction with Zn_3P_2 -based photovoltaics. There are a number of electrical measurements that may be used to determine the band alignment of a heterojunction, including: capacitance-voltage (C-V), temperature-dependent current-voltage (I-V), and internal photoemission spectroscopy (IPE) measurements.¹⁰⁶ However, all of these techniques require working devices and are subject to experimental error due to deviations in ohmic contacts and doping profiles. On the other hand, the method of determining the ΔE_V of a heterojunction interface proposed by Kraut and coworkers does not require the fabrication of a functional electronic device, and is therefore independent of spurious device properties.

The Kraut method employs x-ray photoelectron spectroscopy to determine the ΔE_V of a heterojunction based on core level energy differences.^{111,112} The method relies on the fact that the energy difference between a given core level (CL) and the valence-band maximum (VBM) of a semiconductor material is fixed and does not vary with the position of the Fermi level within the semiconductor. Therefore, measuring the shift in the core-level energies of two semiconductor materials put in contact allows one to determine their valence-band discontinuity. In the case of a II-VI/ Zn_3P_2 heterojunction, ΔE_V is calculated as follows:

$$\Delta E_V (\text{II-VI}/\text{Zn}_3\text{P}_2) = (E_{\text{CL}}^{\text{II-VI}} - E_{\text{VBM}}^{\text{II-VI}}) - (E_{\text{CL}}^{\text{Zn}_3\text{P}_2} - E_{\text{VBM}}^{\text{Zn}_3\text{P}_2}) - \Delta E_{\text{CL},i}, \quad (5.11)$$

where the first two components of Equation 5.11 represent the energy differences between the core level (E_{CL}) and valence-band maximum (E_{VBM}) of the bulk II-VI compound and Zn_3P_2 , respectively, and $\Delta E_{\text{CL},i}$ represents the energy difference between the II-VI and Zn_3P_2 core levels of the II-VI/ Zn_3P_2 heterojunction interface. From the value of ΔE_V , the corresponding value of the conduction-band discontinuity (ΔE_C) can then be calculated from the

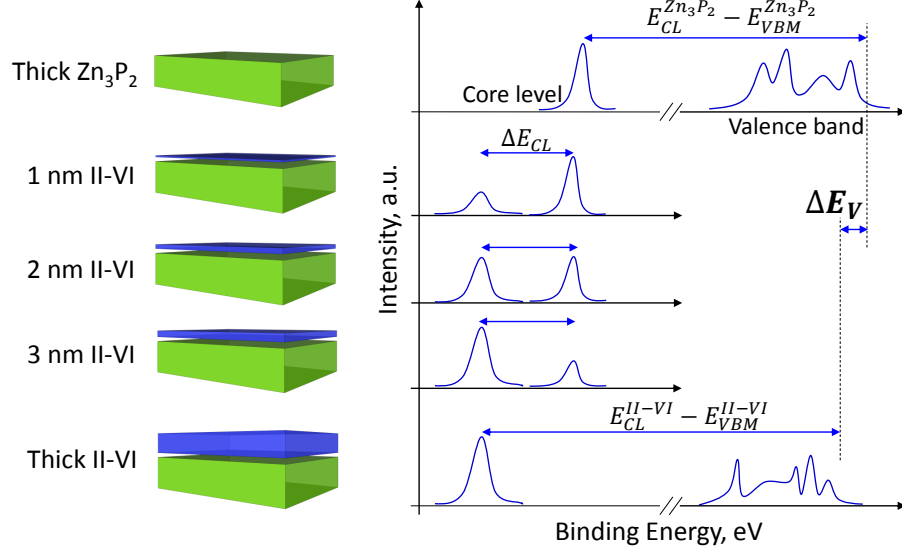


Figure 5.3: A schematic of the Kraut method of determining the ΔE_V of a heterojunction interface using x-ray photoelectron spectroscopy.

reported values for the band gaps of the materials, according to:

$$\Delta E_C (\text{II-VI}/\text{Zn}_3\text{P}_2) = E_g^{\text{II-VI}} - E_g^{\text{Zn}_3\text{P}_2} + \Delta E_V (\text{II-VI}/\text{Zn}_3\text{P}_2). \quad (5.12)$$

The experimental details of the Kraut method are summarized in Figure 5.3. First, the core level to valence-band maximum energy difference is determined for bulk films (~ 200 nm) of the II-VI and Zn_3P_2 material. Next, increasing thicknesses of the II-VI material (typically on the order of $0.1 \sim 3$ nm) are deposited on a bulk Zn_3P_2 film. Since the II-VI overlayers are thinner than the escape depth of electrons from most materials ($3 \sim 6$ nm), the core-level energy positions of both semiconductors can be measured simultaneously, giving $\Delta E_{CL,i}$. Finally, Equation 5.11 and Equation 5.12 can be applied to calculate ΔE_V and ΔE_C , respectively.

5.2.1 X-ray photoelectron spectroscopy measurement

High-resolution XPS measurements on the bulk semiconductors and on heterostructure interfaces were performed in a Kratos surface-science instrument

with a monochromatic Al K α (1486.7 eV) x-ray source and a background pressure of $< 1 \times 10^{-9}$ Torr. Excited photoelectrons were collected at 0° from the surface normal with a detection line width of < 0.26 eV.* All XPS measurements on the bulk semiconductor films were performed in duplicate. Reference measurements of the core-level and valence-band regions were collected on vacuum-cleaved (v.c.) single crystals of each bulk material, to minimize the contribution of surface contamination to the determination of the band offsets.

Interface measurements of $\Delta E_{\text{CL},i}$ were collected for several thicknesses of each II-VI compound deposited onto a thick (~ 200 nm) Zn₃P₂ epilayer. The thickness of the II-VI film typically ranged from 0.2 nm to 3.0 nm. The group-V and group-VI core levels were chosen for the band offset measurements due to the high intensity and narrow peak widths of these signals. However, in the case of the ZnO/Zn₃P₂ interface, the O 1s core level was particularly sensitive to even small amounts of contamination from adventitious H₂O and other surface hydroxide species. Therefore, the Zn 3d core level was used instead and was found to be less surface sensitive while also showing contributions from both Zn-P and Zn-O bonding.

Peak fitting was used to accurately and reproducibly determine the core-level binding energies for all samples. Prior to fitting, photoelectron spectra were processed using a “Shirley”-type baseline subtraction.¹¹³ Core levels were modeled as doublets of weighted Gaussian-Lorentzian (G-L) product functions. The doublet peak area ratio and peak separation for a given core level were constrained across all samples. The peak area ratio was fixed to the theoretically expected relative intensities of excited electrons for a given symmetry (i.e. *s*, *p*, *d*, and *f*).¹¹⁴ The doublet peak separation was constrained to the

*The Kratos’ detector line width was determined by measuring the FWHM of the Au 4f peak collected on a clean Au surface. The Au 4f peak has a known inherent line width of 0.317 eV. The measured Au 4f peaks had FWHM values of < 0.5 eV. The fitting can be found in Figure 5.4.

splitting value observed on the cleaved single crystals. The fitting parameters are summarized in Table 5.1. The average position of the fitted doublet peaks was used as the absolute core-level binding energy for the subsequent offset calculations.

5.2.2 DFT determination of the E_{VBM} position

The VBM positions ($E_{\text{VBM}} - E_{\text{F}}$) of bulk Zn_3P_2 and of the II-VI materials of interest were determined by fitting the measured XPS valence-band region to a calculated valence-band density of states (VB-DOS). This technique is considered more accurate than simple linear extrapolation of the leading edge of the valence-band region.¹¹² In this process, the partial electronic density of states (PEDOS) for each material was calculated ab initio using hybrid DFT. The DFT calculations were performed by my coworker, Prof. David Scanlon, at University College, London, using the VASP code.^{115,116} The projector-augmented wave approach was used to describe the interaction between the core (Zn:[Ar], Cd:[Kr], S:[Ne], and O:[He]) and valence electrons.¹¹⁷ The calculations implemented the screened hybrid functional as proposed by Heyd, Scuseria and Ernzerhof (HSE).¹¹⁸ A percentage of the exact nonlocal Fock exchange (α) was added to the Perdew, Burke and Ernzerhof (PBE) functional with a screening of $\omega = 0.11 \text{ bohr}^{-1}$ applied in order to partition the Coulomb potential into long range (LR) and short range (SR) terms.¹¹⁹ The exchange and correlation terms are:

$$E_{xc}^{\text{HSE}}(\omega) = E_x^{\text{HSE,SR}} + E_x^{\text{PBE,LR}} + E_C^{\text{PBE}}, \quad (5.13)$$

where

$$E_x^{\text{HSE,SR}} = \alpha E_x^{\text{Fock,SR}} + (1 - \alpha) E_x^{\text{PBE,SR}}. \quad (5.14)$$

Table 5.1: X-ray photoelectron spectroscopy core-level fitting parameters for the bulk Zn_3P_2 and II-VI semiconductors.

Material	Core level	Approx. B.E. [eV]	Peak fitting model	Doublet area ratio	Doublet separation [eV]	Measured $E_{\text{CL}} - E_{\text{VBM}}$ [eV]
Zn_3P_2	P $2p$	128.1	1:1 G-L	2:1	0.835	128.51 ± 0.02
	Zn $3d$	9.9	2:1 G-L	3:2	0.400	10.01 ± 0.02
ZnS	S $2p$	162.8	1:1 G-L	2:1	1.200	161.08 ± 0.01
ZnSe	Se $3d$	54.7	1:2 G-L	3:2	0.861	53.18 ± 0.04
CdS	S $2p$	162.2	1:2 G-L	2:1	1.200	160.45 ± 0.04
ZnO	Zn $3d$	9.9	Gaussian	3:2	0.810	7.60 ± 0.06

The Hartree-Fock and PBE exchanges are only mixed in the SR part, with the LR exchange interactions represented by the corresponding part of the range separated PBE functional.

To accurately reproduce the experimentally known band gaps and DOS features of Zn_3P_2 , ZnS , ZnSe , ZnO , and CdS , exchange values of 25%, 33%, 32.5%, 37.5%, and 30% were utilized, respectively. The HSE approach consistently produces structural and band gap data that are more accurate than standard density functional approaches, such as the local density approximation (LDA) or the generalized gradient approximation (GGA).^{120–125} A cut-off value of 600 eV and a k-point mesh of $4 \times 4 \times 3$, $6 \times 6 \times 6$, $6 \times 6 \times 6$, $8 \times 8 \times 6$, and $5 \times 5 \times 4$, all centered on the Γ point, were found to be sufficient for Zn_3P_2 , ZnS , ZnSe , ZnO , and CdS , respectively. All calculations were deemed to be converged when the forces on all atoms were less than $0.01 \text{ eV } \text{\AA}^{-1}$. Calculated band diagrams and DOS for each of the materials of interest can be found in Figure A.2 of Appendix A.3.

The PEDOS contributions were weighted by the known x-ray photoionization cross section of their respective atoms (see Table A.3 of Appendix A.4) and were then summed, resulting in the total VB-DOS.¹²⁶ The weighting was performed to accurately represent the processes that contributed to the experimental XPS data. The raw VB-DOS was then convoluted with an instrument-specific spectrometer response function and the results were then fit to the leading edge of the XPS data. The spectrometer response function was determined for the Kratos instrument by measurement of the Au $4f$ doublet. The Au spectrum was fit to a Voigt function assuming Gaussian broadening and an inherent Lorentzian linewidth of 0.317 eV. The details of the convolution and fitting procedure have been described previously.¹¹² Figure 5.4 shows the x-ray photoelectron spectrum of the Au $4f$ core level and the fitted Voigt function.

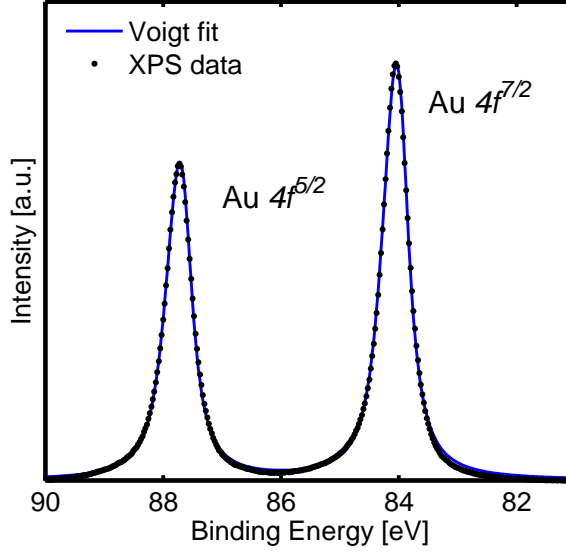


Figure 5.4: The X-ray photoelectron spectrum of the Au 4*f* core level fitted to a Voigt function in order to determine Kratos instrument specific response function.

5.3 Band alignment results

5.3.1 Bulk semiconductor valence-band region

The x-ray photoelectron spectra of the valence-band region of bulk Zn₃P₂ film and the four bulk II-VI compounds of interest are displayed in Figure 5.5 and Figure 5.6, respectively. For all of the materials studied, nearly identical spectra were obtained for the “bulk” films and the vacuum-cleaved wafers (data not shown), indicating that there was negligible contribution from surface contamination due to several minute’s exposure to air. Along with the experimental data, Figure 5.5 and Figure 5.6 also display the VB-DOS calculations after correction for the atomic scattering factors (Raw VB-DOS) as well as after convolution with the Kratos spectrometer response function (Conv. VB-DOS). Excellent qualitative agreement was observed between the structural features of the measurements and the calculations. The inset of each figure displays the fit to the leading edge of the XPS data with the convolved

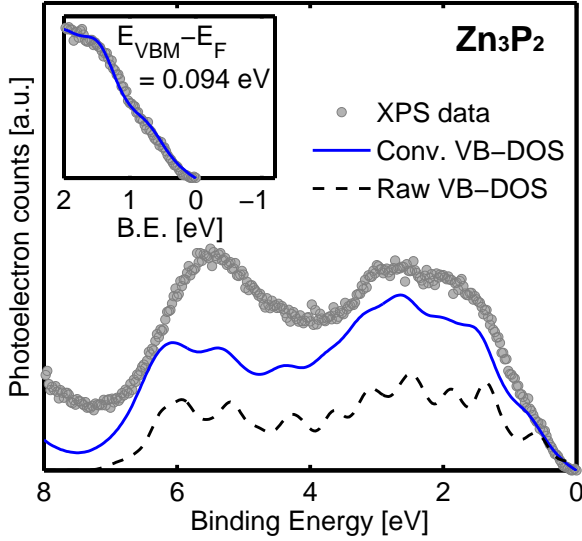


Figure 5.5: High-resolution x-ray photoelectron spectra of the valence-band region of a bulk Zn_3P_2 film. The calculated VB-DOS is also displayed before and after convolution with the spectrometer response function. The insets show the VBM position determined by fitting the convolved VB-DOS to the XPS data.

VB-DOS, resulting in a value for the position of the VBM. The absolute value of the VBM differed from sample to sample due to small variations in doping. This behavior was especially true for vacuum-cleaved samples, which typically had extremely intrinsic doping levels. Nevertheless, the relative position of the core-level binding energy to the VBM was very reproducible for each bulk material. Values of $E_{\text{CL}} - E_{\text{VBM}}$ measured for the bulk semiconductor compounds averaged over three samples, including the vacuum-cleaved wafers, can be found in Table 5.1.

It is important to note the difference between the VBM position as determined using conventional linear extrapolation of the valence-band leading edge versus that determined by the VB-DOS fitting procedure described above. For instance, a $\sim 0.24 \text{ eV}$ difference was observed in the position of the ZnS VBM determined by the VB-DOS fitting relative to the value obtained by linear

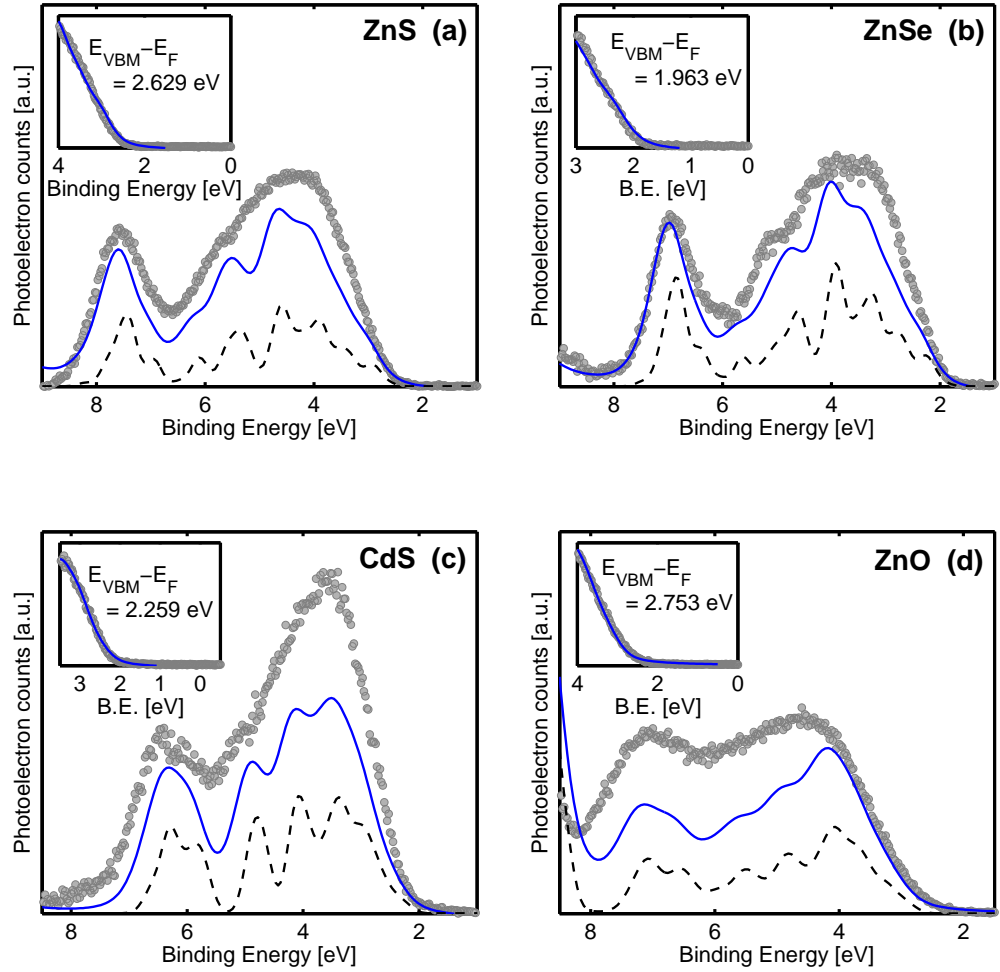


Figure 5.6: High-resolution x-ray photoelectron spectra of the valence-band regions of (a) ZnS, (b) ZnSe, (c) CdS, and (d) ZnO. The calculated VB-DOS is also displayed before and after convolution with the spectrometer response function. The insets show the VBM position determined by fitting the convoluted VB-DOS to the XPS data.

extrapolation. The difference was likely due to a low calculated DOS near the edge of the valence-band. The low DOS was captured by the tail of the leading edge of the XPS spectra which is not well represented by the linear extrapolation method, thus resulting in an overestimation of the VBM position. A > 0.2 eV discrepancy is rather large and points to the importance of using

the convolved VB-DOS fitting to improve the accuracy of the band alignment measurements.

5.3.2 ZnS/Zn₃P₂ band alignment

X-ray photoelectron survey spectra for bulk Zn₃P₂, bulk ZnS, and an ultrathin ZnS/Zn₃P₂ heterojunction were recorded in order to verify sample purity. Only peaks belonging to Zn, S, and P species were observed in addition to trace amounts of adventitious C and O. Oxides were not observed for the core-level Zn, S, or P peaks suggesting that all oxygen surface species were due to physisorbed water.

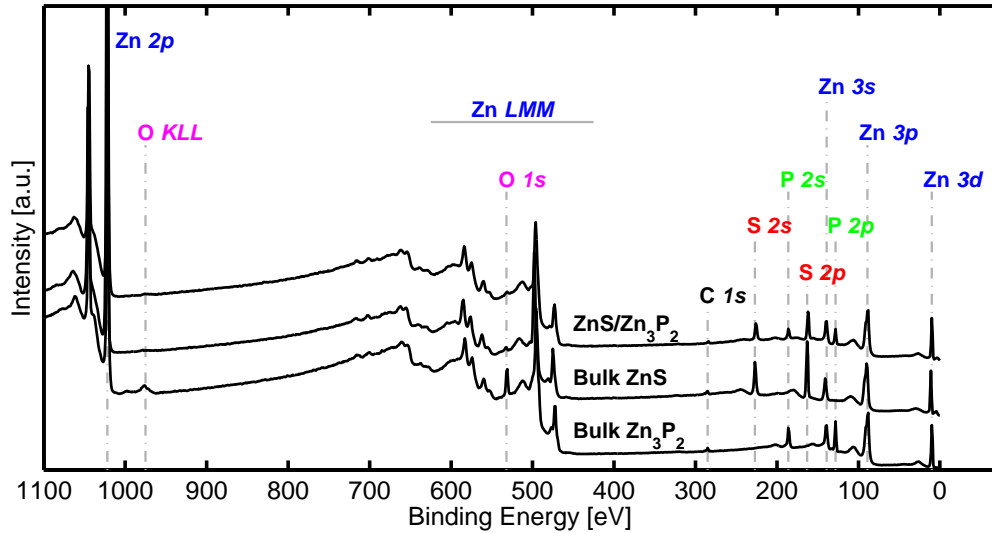


Figure 5.7: XPS surveys scan of (a) bulk Zn₃P₂, (b) bulk ZnS, and (c) an ultrathin ZnS/Zn₃P₂ heterojunction interface.

Figures 5.8a and 5.8b display the XPS data for the P 2*p* and S 2*p* core levels of bulk Zn₃P₂, bulk ZnS, and the 0.6 nm, 1.4 nm, and 2.2 nm ZnS/Zn₃P₂ heterojunctions. The fitted P 2*p*^{3/2} and S 2*p*^{3/2} core-level binding energies are reported in Table A.4 of Appendix A.5. The Zn₃P₂ P 2*p* core level was composed of two doublet pairs – an intense, low binding-energy doublet due

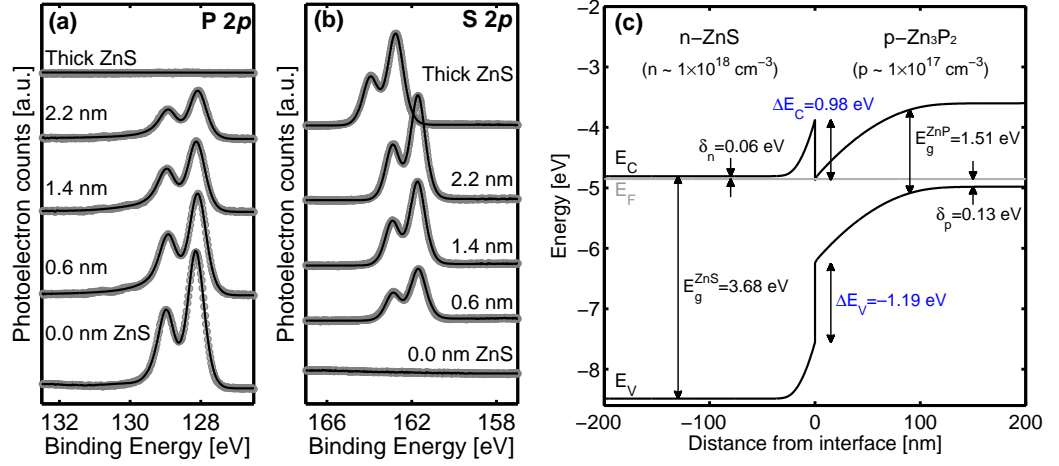


Figure 5.8: Fitted XPS data of the (a) P 2*p* and (b) S 2*p* core levels measured on ultrathin ZnS/Zn₃P₂ heterojunction interfaces of increasing ZnS overlayer thickness. (c) The energy-band alignment for an n-ZnS/p-Zn₃P₂ heterojunction interface calculated given the measured ΔE_V and assumed doping levels of $n = 1 \times 10^{18} \text{ cm}^{-3}$ and $p = 1 \times 10^{17} \text{ cm}^{-3}$ for ZnS and Zn₃P₂, respectively.

to bulk Zn–P bonding, and a low-intensity, higher binding-energy doublet that has previously been attributed to surface P–P bonding.²⁵ The spectra indicated a shift of $\sim 1.2 \text{ eV}$ in the S 2*p* binding energy upon formation of the heterojunction interface. However, little or no shift was observed for the P 2*p* binding energy. The core-level binding energy differences ($\Delta E_{CL,i}$) observed for all interface samples are displayed in Table A.4. An average value of $\Delta E_{CL,i} = 33.78 \pm 0.03 \text{ eV}$ was calculated for the five heterojunction samples.

From the core-level binding energies and VBM positions determined using the VB-DOS fitting, Equation 5.11 yielded $\Delta E_V = -1.19 \pm 0.07 \text{ eV}$. The ΔE_V was found to be independent of ZnS film thickness (see Table A.4), indicating minimal contributions due to any band bending near the interface. A direct determination of ΔE_V was also performed by fitting the measured valence-band spectrum of a heterojunction interface to a superposition of the valence

spectra of bulk ZnS and Zn₃P₂.¹⁰⁶ This process yielded excellent agreement between the fit and the XPS data. A value of ΔE_V was then directly calculated from the difference in the VBM positions of the superimposed bulk spectra. The fitted ΔE_V was similar across all heterojunction samples (see Table A.4 of Appendix A.5) and resulted in an average $\Delta E_V = -1.12 \pm 0.07$ eV, which is consistent with the value of ΔE_V determined from Equation 5.12. Use of the known band gaps for ZnS and Zn₃P₂ of 3.68 eV and 1.51 eV, respectively, yielded $\Delta E_C = 0.98 \pm 0.07$ eV.

Figure 5.8c displays the calculated band alignment of a proposed n-ZnS/p-Zn₃P₂ heterojunction under equilibrium conditions. The energy-bands were simulated using the AFORS-HET device modeling software package.¹²⁷ The energy differences between the Fermi level and the conduction and valence bands ($\delta n = E_C - E_F$, $\delta p = E_F - E_V$) in the quasi-neutral region of each semiconductor were calculated assuming realistic doping levels of $n = 1 \times 10^{18} \text{ cm}^{-3}$ and $p = 1 \times 10^{17} \text{ cm}^{-3}$ for the ZnS and Zn₃P₂, respectively. The simulations demonstrated the existence of a large conduction-band spike at the ZnS/Zn₃P₂ interface due to the type-I nature of the energy-band alignment. The conduction-band spike is likely to inhibit charge transfer at the heterojunction interface and indicates that ZnS is a non-optimal emitter layer for Zn₃P₂. However, these results suggest that ZnS can provide a good surface passivation layer for Zn₃P₂ and may be useful as a thin, intrinsic layer in metal-insulator-semiconductor (MIS) or semiconductor-insulator-semiconductor (SIS) photovoltaic devices.

5.3.3 ZnSe/Zn₃P₂ band alignment

Figures 5.9a and 5.9b display the fitted XPS spectra of the P 2*p* and Se 3*d* core levels obtained from samples of varying ZnSe overlayer thickness grown on thick Zn₃P₂. Similar to the ZnS/Zn₃P₂ heterojunction, the Zn₃P₂ P 2*p* core level again showed contributions from surface and/or interfacial P–P bonding. Upon heterojunction formation, little or no shift was observed in the bulk P 2*p*

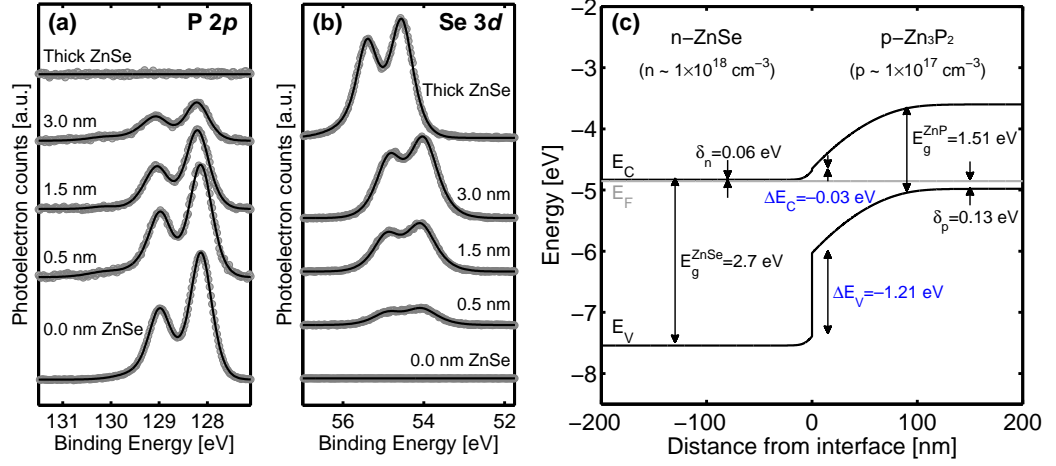


Figure 5.9: Fitted XPS data of the (a) P 2*p* and (b) Se 3*d* core levels measured on ultrathin ZnSe/Zn₃P₂ heterojunction interfaces of increasing ZnSe overlayer thickness. (c) The energy-band alignment for an n-ZnSe/p-Zn₃P₂ heterojunction interface calculated given the measured ΔE_V and assumed doping levels of $n = 1 \times 10^{18} \text{ cm}^{-3}$ and $p = 1 \times 10^{17} \text{ cm}^{-3}$ for ZnSe and Zn₃P₂, respectively.

binding energy, but a $\sim 0.7 \text{ eV}$ shift toward lower binding energy was observed for the Se 3*d* core level. Only a small variation in $\Delta E_{CL,i}$ was observed with increasing ZnSe thickness, indicating minimal band bending in the overlayer. An average $\Delta E_{CL,i}$ of $-74.12 \pm 0.05 \text{ eV}$ was calculated across five interface samples. Use of Equation 5.11 and Equation 5.12 yielded $\Delta E_V = -1.21 \pm 0.11 \text{ eV}$ and $\Delta E_C = -0.03 \pm 0.11 \text{ eV}$ for the ZnSe/Zn₃P₂ heterojunction. Figure 5.9c displays the energy-band diagram of an n-ZnSe/p-Zn₃P₂ heterojunction under equilibrium conditions, given the measured band discontinuities. The offset measurement indicated an alignment of the ZnSe and Zn₃P₂ conduction bands within a tenth of an eV, resulting in either a slightly type-I or type-II junction.

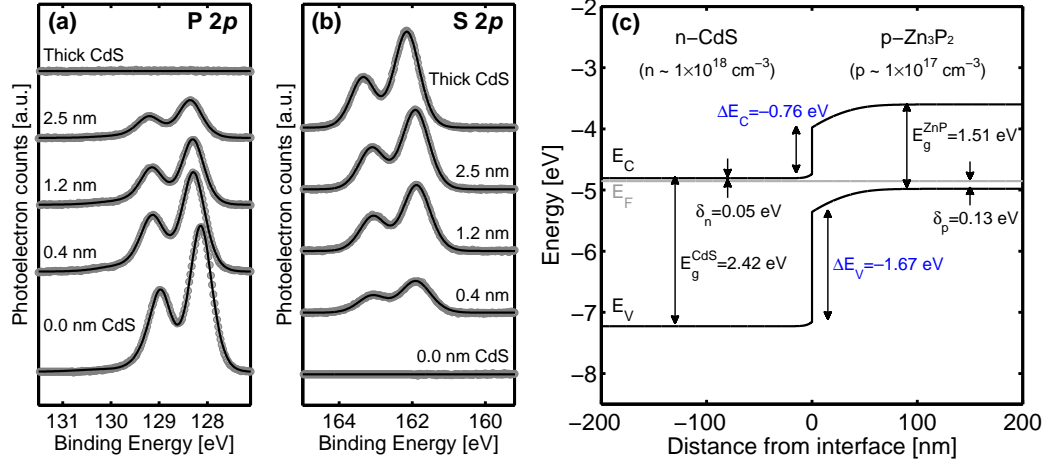


Figure 5.10: Fitted XPS data of the (a) P 2*p* and (b) S 2*p* core levels measured on ultrathin CdS/Zn₃P₂ heterojunction interfaces of increasing CdS overlayer thickness. (c) The energy-band alignment for an n-CdS/p-Zn₃P₂ heterojunction interface calculated given the measured ΔE_V and assumed doping levels of $n = 1 \times 10^{18} \text{ cm}^{-3}$ and $p = 1 \times 10^{17} \text{ cm}^{-3}$ for CdS and Zn₃P₂, respectively.

5.3.4 CdS/Zn₃P₂ band alignment

Figures 5.10a and 5.10b display the XPS data for the P 2*p* and S 2*p* core levels measured on thin CdS/Zn₃P₂ heterostructures having various CdS film thicknesses. Upon heterojunction formation, a $\sim 0.3 \text{ eV}$ shift towards lower binding energy was observed for the S 2*p* peaks, whereas a slight ($\sim 0.1 \text{ eV}$) shift toward higher binding energy was observed for the P 2*p* core level. The average value for $\Delta E_{CL,i}$ was $33.61 \pm 0.04 \text{ eV}$, resulting in ΔE_V and ΔE_C values of $-1.67 \pm 0.10 \text{ eV}$ and $-0.76 \pm 0.10 \text{ eV}$, respectively. The measured offsets yielded the calculated energy-band diagram of Figure 5.10c for the n-CdS/p-Zn₃P₂ heterojunction. The CdS/Zn₃P₂ interface demonstrated a clear type-II alignment with a much larger conduction-band offset than was observed for the ZnSe/Zn₃P₂ interface.

5.3.5 ZnO/Zn₃P₂ band alignment

Figure 5.11a displays the Zn 3*d* core level spectra measured on ZnO/Zn₃P₂ heterostructures. Upon interface formation, two separate contributions were observed in the Zn 3*d* peak due to the presence of phosphide and oxide phases. These peaks were reproducibly discriminated by use of the fitting procedure described earlier. Similar to the other heterojunctions studied, the binding energy of the phosphide peak remained constant as the thickness of the oxide layer increased. However, a shift of ~ 0.9 eV toward higher binding energy was observed for the interfacial oxide peak relative to the position of the bulk oxide peak. Additionally, a slow decrease in the separation of the core levels (equivalent to a decrease in the ΔE_V) was observed with increasing ZnO thickness, indicating that some band bending was present within the ZnO layer. The band bending resulted in a small decrease in the accuracy of the band-offset measurement. An average $\Delta E_{CL,i}$ of 1.10 ± 0.08 eV was measured across six interface samples, leading to calculated ΔE_V and ΔE_C values of -3.50 ± 0.16 eV and -1.61 ± 0.16 , respectively, for this interface.

Figure 5.11b displays the energy-band diagram for an n-ZnO/p-Zn₃P₂ heterojunction. Based on the measured band discontinuities, the position of the ZnO conduction-band minimum was located just below the Zn₃P₂ valence-band maximum, resulting in a slightly type-III or “staggered” alignment. The ZnO conduction and valence bands were bent sharply downward in energy at the interface, due to the abnormal staggered band alignment with Zn₃P₂. This behavior is in the opposite direction of the type-II alignment that was observed in the band diagrams for ZnSe/Zn₃P₂ and CdS/Zn₃P₂ heterojunctions. However, the calculated band bending qualitatively agreed with the trend in the XPS core-level separation that was observed for increasing oxide thickness.

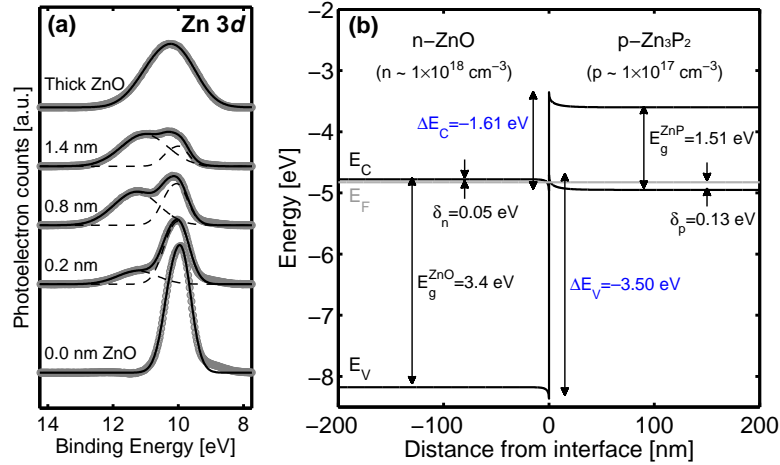


Figure 5.11: Fitted XPS data of the Zn 3d core level for sputter-deposited ZnO/Zn₃P₂ heterojunction interfaces with increasing ZnO thickness. The interface peaks show contributions from both the phosphide and oxide states. (c) The energy-band alignment for an n-ZnO/p-Zn₃P₂ heterojunction interface calculated given the measured ΔE_V and assumed doping levels of $n = 1 \times 10^{18} \text{ cm}^{-3}$ and $p = 1 \times 10^{17} \text{ cm}^{-3}$ for ZnO and Zn₃P₂, respectively.

5.4 Discussion

5.4.1 II-VI/Zn₃P₂ band offsets – measurement vs. prediction

In order to gain a better understanding of the II-VI/Zn₃P₂ heterojunction system, we compared the measured band alignments with the values predicted by various approaches including the Anderson electron affinity (EA) model,¹⁰⁵ the effective interface dipole model,¹⁰⁷ and available DFT calculations.¹¹⁰ The results of the comparison between prediction and experiment are summarized in Figure 5.12. In some cases, the observed band alignments for the II-VI/Zn₃P₂ heterojunction interfaces differ significantly from the alignments predicted by Anderson theory. Discrepancies of >0.4 eV between the EA model and the

measured ΔE_C indicate the presence of more complicated bulk and/or surface phenomena.

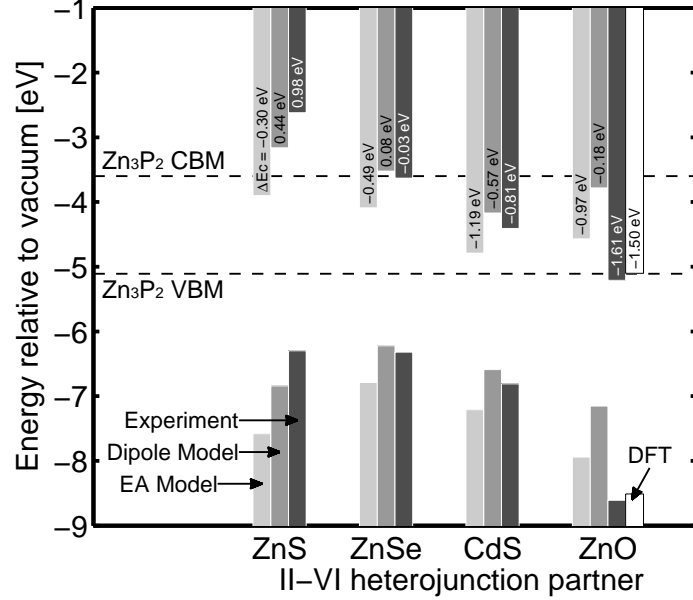


Figure 5.12: A comparison of experimentally measured II-VI/ Zn_3P_2 heterojunction band offsets with those predicted from the electron-affinity (EA) model,¹⁰⁵ an effective interface dipole model,¹⁰⁷ and universal hydrogen-level alignment calculations.¹¹⁰ The conduction-band minimum (CBM) of Zn_3P_2 was fixed at -3.6 eV with respect to the vacuum level based on the reported electron affinity.⁷⁸

Unlike devices comprised of III-V and II-VI compound semiconductors, the interfacial dipole that is expected to occur for a mixed valency II-VI/II-V heterojunction is currently not well elucidated. For example, the measured electronic structure of the $\text{ZnS}/\text{Zn}_3\text{P}_2$ heterojunction may reflect effects of interfacial crystalline strain as well as interfacial chemical reactions. The effect of interfacial strain is assumed to be less significant for the $\text{ZnSe}/\text{Zn}_3\text{P}_2$ heterojunction since the lattice mismatch between the two semiconductors is much smaller. On the other hand, in situ RHEED data indicated that the ZnS layers relaxed immediately upon film growth (see Figure 4.1), implying that

interfacial strain effects are minimal. Interfacial strain should also produce band offsets that depended on the thickness of the overlayer, in contrast to the experimental observations. Interfacial chemical reactions between P and S could produce deviations in the band alignment. Consistently, P–P bonding, or possibly P–VI bonding, was observed in the XPS measurements of the ultrathin heterostructure samples. Attempts to limit reactions by exposing the Zn_3P_2 surface to a Zn metal flux immediately prior to II-VI deposition had no detectable effect on the XPS measurements or on the observed band alignment.

As discussed earlier in subsection 5.1.2, the dipole model proposed by Ruan and Ching¹⁰⁷ is a first-order correction to the EA model and in general results in improved predictions of ΔE_C , especially for ZnS, ZnSe, and CdS heterojunctions. The model was used to estimate the offsets for all of the II-VI/ Zn_3P_2 interfaces. The value of χ and other fundamental properties for Zn_3P_2 and the II-VI materials used in the dipole-model calculations can be found in Table A.2 of Appendix A.3. The dipole model gives the best prediction for the ZnSe/ Zn_3P_2 heterojunction, which has the smallest lattice mismatch of all the systems and therefore is likely to have the lowest density of interfacial defects. The interface dipole model is also very sensitive to the value of the hole effective masses of Zn_3P_2 , which are poorly known. In this work, the Zn_3P_2 hole effective masses for each of the valence bands were approximated by fitting a parabolic function to the valence-band curvature that was calculated by DFT. The value of the Zn_3P_2 hole mass for each of the principal axis directions can be found in Table A.1 of Appendix A.3. The discrepancy between the prediction of the dipole model and the measured offsets is consistent with a possible inaccuracy in the effective masses or with a modification in the values of the effective masses upon interface formation.

Both the EA model and the effective interface dipole model failed to even qualitatively predict the ZnO/ Zn_3P_2 band offsets. However, the $\Delta E_V = -3.4$ eV calculated by Limpijumnong and coworkers using DFT is in excellent agree-

ment with the value of -3.5 eV measured herein.¹¹⁰ The calculation used the method described earlier assuming the universal alignment of the electronic transition levels of H interstitials in the two semiconductors.¹⁰⁹ The agreement between the DFT theory and experiment (as well as lack of agreement between the effective dipole model and experiment) suggests that the staggered band alignment observed for ZnO/Zn₃P₂ is not a result of an interface dipole or surface reconstruction, but is inherent to the bulk materials system.

5.4.2 Band alignment and photovoltaic device performance

The measured band discontinuities of the II-VI/Zn₃P₂ interfaces are well correlated with the previously reported device performance for these heterojunctions. For instance, the type-I alignment measured for the ZnS/Zn₃P₂ heterojunction should lead one to expect (1) electron transport across the ZnS/Zn₃P₂ interface would be impeded by the large conduction band spike and (2) the ZnS to be extremely passivating of the Zn₃P₂ surface. These expectations correlate well with our own device studies on ZnS/Zn₃P₂ heterojunctions where only very low current densities of < 0.05 mA cm⁻² could be obtained, whereas, record V_{oc} 's of > 800 mV were achieved, indicating very low recombination rates at the ZnS/Zn₃P₂ interface and hence excellent passivation (see subsection 6.1.1 for details).³⁷

On the other hand, the alignment of the ZnSe and Zn₃P₂ conduction bands suggests that a large barrier height should be attainable for a ZnSe/Zn₃P₂ solar cell. Bhushan et al. demonstrated V_{oc} 's as high as 810 mV and diffusion voltages (V_D) > 1.4 V for superstrate Zn₃P₂/ZnSe solar cells.³⁶ Under ideal conditions (i.e. removal of all non-radiative recombination pathways), the barrier height of these ZnSe/Zn₃P₂ heterojunctions approached the value of the band gap of Zn₃P₂. The ZnSe/Zn₃P₂ conduction-band alignment also implies facile electron transport across the junction as well as a hole-blocking

layer due to the large valence-band offset. Combined, these characteristics result in good carrier separation at the heterojunction interface, consistent with the relatively high reported V_{oc} 's for this system. The superstrate design ultimately limited the overall device performance because the solar cell was illuminated on the back side of the Zn_3P_2 , resulting in a large amount of carrier recombination at the back contact and therefore low J_{sc} 's. Thus, improved performance should be attainable with a substrate device in which the ZnSe is deposited directly onto the Zn_3P_2 surface.

Conversely, the measured $\Delta E_C = -0.76$ eV for the CdS/ Zn_3P_2 interface results in a maximum possible barrier height of ~ 700 mV. This value is in good agreement with the V_D of 640 mV for CdS/ Zn_3P_2 solar cells that had been reported by Suda and coworkers.³⁵ The low attainable barrier height of the CdS/ Zn_3P_2 heterojunction will therefore limit the maximum efficiency of these types of solar cells. One possible way to manipulate the conduction-band offset between CdS and Zn_3P_2 is to use a $Cd_{1-x}Zn_xS$ emitter. Since the ZnS/ Zn_3P_2 heterojunction has a conduction-band spike of ~ 1 eV, a $Cd_{1-x}Zn_xS$ alloy should facilitate tuning of the position of the conduction band to closely match that of Zn_3P_2 , in accord with reports in the literature.³⁶ Alloying would also increase the band gap of the emitter over that of CdS and in principle create a better lattice match with Zn_3P_2 as compared to either CdS or ZnS alone, resulting in better collection efficiency at shorter wavelengths of light and a lower density of interfacial defects.

Based on the measured energy-band alignment, the conduction band of ZnO forms a tunnel junction with the Zn_3P_2 valence band. This prediction is not in accord with the observation that ZnO/ Zn_3P_2 heterojunction photovoltaic devices reported by Nayar et al. showed V_{oc} 's as high as 300 mV.³⁰ Their devices were fabricated on freshly etched Zn_3P_2 ($p \sim 2 \times 10^{15} \text{ cm}^{-3}$) followed by several minutes of sputter cleaning, with the ZnO films deposited by co-sputtering of ZnO and Zn metal using pure Ar. Possible mechanisms for creation of a barrier include:

- (1) Formation of a $\text{Zn}_x(\text{PO}_3)_y$ interfacial layer during sputter deposition. A layer of ill-defined oxide composition could produce a significantly altered band alignment with Zn_3P_2 and thus a measurable barrier height in a photovoltaic device.
- (2) Formation of a rectifying Schottky contact with metal precipitates at the $\text{ZnO}/\text{Zn}_3\text{P}_2$ interface.
- (3) Formation of an n-type inversion layer at the surface of the Zn_3P_2 resulting in a buried homojunction.

Mechanism (1) is not likely to be the cause of the barrier height in the $\text{ZnO}/\text{Zn}_3\text{P}_2$ heterojunction because little to no oxidation was observed for the Zn_3P_2 P 2*p* core level after ZnO deposition under a 10% O_2 partial pressure used herein. A $\text{Zn}_x(\text{PO}_3)_y$ layer of significant thickness is therefore unlikely to have formed under the less-oxidizing sputtering conditions used by Nayar and Catalano. Furthermore, Zn metal has been reported to form an ohmic contact with Zn_3P_2 ,³⁸ eliminating the prospect of mechanism (2), Schottky barrier formation at this interface. Mechanism (3) therefore represents a more likely explanation for the observed barrier height. The formation of an inversion layer at the Zn_3P_2 surface is not apparent from the band diagram of the $\text{ZnO}/\text{Zn}_3\text{P}_2$ heterostructure. The tunnel junction formation instead favors hole accumulation at the Zn_3P_2 surface, which has been proposed as an alternative mechanism for the p-type conductivity in P-doped ZnO films.¹¹⁰ However, fixed positive charge at the $\text{ZnO}/\text{Zn}_3\text{P}_2$ interface could induce an inversion layer in weakly p-type Zn_3P_2 , in accord with suggestions of such behavior at oxidized Zn_3P_2 surfaces.¹²⁸

5.5 Conclusions

The energy-band alignments have been established for heterojunctions of ZnS, ZnSe, CdS, and ZnO n-type semiconductors grown on Zn_3P_2 . The ZnS/ Zn_3P_2

heterojunction demonstrated a type-I band alignment with a large conduction band spike indicating that ZnS is non-ideal as an emitter for Zn_3P_2 , but should make an excellent surface passivation layer. The $\text{ZnSe}/\text{Zn}_3\text{P}_2$ interface had a negligible conduction-band offset and a large hole-blocking barrier, demonstrating an optimal alignment for a heterojunction solar cell. This ideal alignment is reflected in the significant open-circuit photovoltages and large barrier heights reported for $\text{ZnSe}/\text{Zn}_3\text{P}_2$ solar cells. The $\text{CdS}/\text{Zn}_3\text{P}_2$ heterojunction was type-II, with a much larger conduction-band offset than for $\text{ZnSe}/\text{Zn}_3\text{P}_2$. This behavior accounts for the inferior V_{oc} observed for $\text{CdS}/\text{Zn}_3\text{P}_2$ heterojunctions relative to $\text{ZnSe}/\text{Zn}_3\text{P}_2$ heterojunctions. However, the offset can potentially be modified by the use of $\text{Cd}_{1-x}\text{Zn}_x\text{S}$ ternary alloys, which should result in a more ideal band alignment and a larger emitter band gap. The $\text{ZnO}/\text{Zn}_3\text{P}_2$ interface was found to have an unusual type-III alignment that resulted in a tunnel junction between the ZnO and Zn_3P_2 . The offset was poorly predicted by electron affinity and interface dipole models, but was well described by universal H-level alignment theory, which suggests the band alignment is intrinsic to the bulk semiconductors. The barrier heights reported for $\text{ZnO}/\text{Zn}_3\text{P}_2$ heterojunction solar cells therefore likely arise from mixed composition or surface states at the interface.

CHAPTER 6

Zn₃P₂ photovoltaic devices

The following chapter describes our experiences with the fabrication and evaluation of various Zn₃P₂ thin-film solar cells. We have explored several device designs including: substrate and superstrate architectures, metal-insulator-semiconductor (MIS) devices, and gated field-effect device structures. All devices were tested using current versus voltage (I-V) measurements under simulated Air Mass (AM) 1.5 1-sun illumination and evaluated based on their efficiency as well as operating parameters such as V_{oc} , J_{sc} , and FF .

6.1 Substrate devices

We began our efforts with the simplest thin-film heterojunction design possible – a typical substrate device, a schematic of which is displayed in Figure 6.1. The substrate device architecture is comprised of (from bottom to top) a conductive substrate, p-type photovoltaic absorber layer, n-type emitter layer, and emitter front contact busbar and finger grid. *Many* variations of this general design are possible, particularly regarding the choice of emitter and

intermediate layers, the details of which are also described in the following sections.

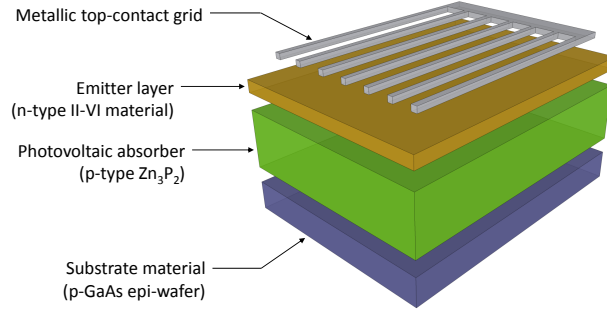


Figure 6.1: Schematic of a substrate II-VI/ Zn_3P_2 heterojunction solar cell.

6.1.1 $\text{ZnS}/\text{Zn}_3\text{P}_2$ heterojunction solar cell

Despite the type-I energy-band alignment observed for a $\text{ZnS}/\text{Zn}_3\text{P}_2$ heterojunction, it was proposed that high enough doping ($n \geq 1 \times 10^{18} \text{ cm}^{-3}$) in the ZnS emitter would mitigate the conduction band spike at the interface by allowing electron tunneling to occur. Epitaxial $\text{ZnS}/\text{Zn}_3\text{P}_2$ heterojunction devices were grown on heavily-doped p-GaAs substrates ($p \geq 1 \times 10^{18} \text{ cm}^{-3}$). The ZnS and Zn_3P_2 film thicknesses were 120 nm and 1 μm , respectively, with nominal dopant densities of $n \sim 1 \times 10^{18} \text{ cm}^{-3}$ and $p \sim 1 \times 10^{15} \text{ cm}^{-3}$, respectively. The total junction area was 0.35 cm^2 and an Al busbar with fingers was used as a top contact to the ZnS. The contact was deposited using electron-beam evaporation through a laser-cut physical mask. An alternative design with an ITO transparent, conductive contact instead of an Al finger grid was also attempted. However, the ITO failed to make sufficient ohmic contact to the ZnS emitter making those devices difficult to evaluate. A multilayer Pt-Ti-Pt (10 nm/ 20 nm/ 30 nm) metal structure was used to make low resistivity ohmic contact to the p-GaAs substrate for all devices.¹²⁹ The Pt-Ti-Pt contact demonstrated a contact resistance of $< 7 \times 10^{-5} \Omega\text{-cm}^2$ based on transmission

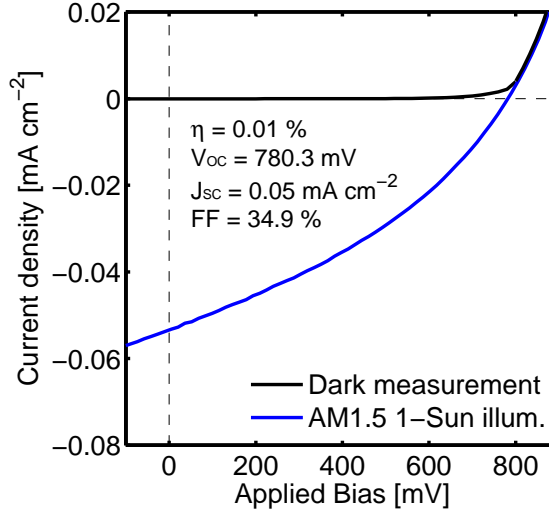


Figure 6.2: I-V response of the ZnS/Zn₃P₂ heterojunction device under dark and AM1.5 1-sun illumination.

line measurements.

The I-V properties of the ZnS/Zn₃P₂ heterojunction under dark and illuminated conditions are displayed in Figure 6.2. The device exhibited a J_{sc} of $< 0.1 \text{ mA cm}^{-2}$, indicating severely high series resistance across the junction. The high series resistance is in agreement with the conduction-band spike inhibiting charge transfer at the heterojunction interface, as proposed earlier in subsection 5.3.2. This occurred despite the high doping levels achieved in the ZnS emitter. Band bending calculations conducted in AFORS-HET demonstrated that the FWHM of the conduction-band spike was $\sim 10 \text{ nm}$ for an electron concentration of 10^{18} cm^{-3} , large enough to block electron tunneling. However, the devices consistently demonstrated V_{oc} 's of $> 750 \text{ mV}$, indicating improved passivation of the Zn₃P₂ surface, as was expected for the type-I alignment. The observed V_{oc} 's were much larger than those previously observed for heterojunctions implementing Zn₃P₂ as an absorber layer (see Table 1.1 in section 1.3) and are an indication that the epitaxial II-VI/Zn₃P₂ heterojunction design shows major potential.

An alternative approach to take advantage of the electronic passivation

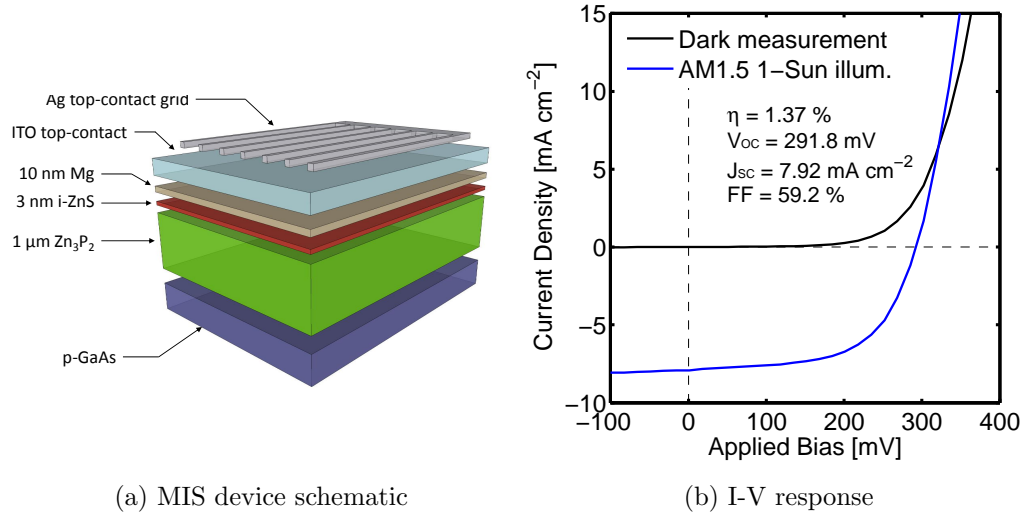


Figure 6.3: (a) Schematic and (b) I-V response of the Mg/ $\text{ZnS}/\text{Zn}_3\text{P}_2$ metal-insulator-semiconductor (MIS) device under dark and AM1.5 1-sun illumination.

offered by the type-I band alignment between ZnS and Zn_3P_2 is a metal-insulator-semiconductor (MIS) device architecture. Here, a thin, intrinsic layer of ZnS acts only as a passivating layer between the Zn_3P_2 surface and metal Schottky contact. The assumption is that the $\text{ZnS}/\text{Zn}_3\text{P}_2$ interface will have a much lower surface recombination velocity (SRV) than the direct metal/ Zn_3P_2 interface. Electron transport across the ZnS insulator must occur via tunneling. Therefore the layer has to be extremely thin, on the order of $2 \sim 5$ nm. A Mg/ $\text{ZnS}/\text{Zn}_3\text{P}_2$ MIS device was fabricated in the same fashion as the $\text{ZnS}/\text{Zn}_3\text{P}_2$ device described above. A 3 nm thick ZnS layer was grown directly on top of the Zn_3P_2 absorber. Afterward, a semi-transparent Mg layer (10 nm thick) and a 100 nm thick ITO transparent contact were deposited by magnetron sputtering. A schematic of the final device is shown in Figure 6.3a.

The I-V properties of the Mg/ $\text{ZnS}/\text{Zn}_3\text{P}_2$ MIS solar cell under dark and illuminated conditions are displayed in Figure 6.3b. A remarkable increase in current is observed with the MIS device compared to the ZnS heterojunction. A J_{sc}

of 7.92 mA cm^{-2} was obtained. Even higher J_{sc} 's are likely possible by optimizing the absorber thickness and minimizing metal contact reflection losses. However, the V_{oc} of $\sim 300 \text{ mV}$ for the MIS device is nowhere near as high as the $> 750 \text{ mV}$ observed for the ZnS heterojunction. In this case, the V_{oc} is limited by the intrinsic barrier height between Mg and Zn_3P_2 which is in return limited by the electron affinity of Mg metal. The MIS structure, while improved, is still limited in similar ways to a normal Schottky device. Hence, we continued our efforts on heterojunction designs.

6.1.2 ZnSe/ Zn_3P_2 solar cells

Unlike the ZnS/ Zn_3P_2 heterojunction, the type-II band alignment observed for the ZnSe/ Zn_3P_2 heterojunction was determined to be nearly ideal for solar cell operation. Epitaxial ZnSe/ Zn_3P_2 solar cells were grown by MBE in a similar fashion to the ZnS devices. Typical devices were composed of a $2 \sim 3 \text{ }\mu\text{m}$ Zn_3P_2 layer on top of which a 200 nm Al-doped ZnSe emitter was deposited. Finally, either an ITO transparent top contact or Ag busbar and finger grid were deposited on the ZnSe emitter. Final device areas were 0.35 cm^2 or 0.5 cm^2 . The I-V response of a ZnSe/ Zn_3P_2 solar cell is displayed in Figure 6.4. The dark response of the device showed excellent diode behavior. Under illumination the device demonstrated photogenerated current and a clear power-producing region in the I-V curve. However, both the observed J_{sc} and V_{oc} were substantially lower than expected for the given band alignment. One would expect a J_{sc} of $\sim 20 \text{ mA cm}^{-2}$ and a V_{oc} of $> 800 \text{ mV}$ for a properly functioning device.

The low photocurrent combined with the low voltage made us suspect that the doping in ZnSe was lower than intended. Therefore, additional Hall effect measurements were performed on Al:ZnSe films grown on thin Zn_3P_2 films. For these samples, intrinsic GaAs wafers were used as growth substrates. The Hall effect measurements were inconclusive due to the fact that ohmic contact could not be made to the ZnSe layer, indicating that the film was indeed

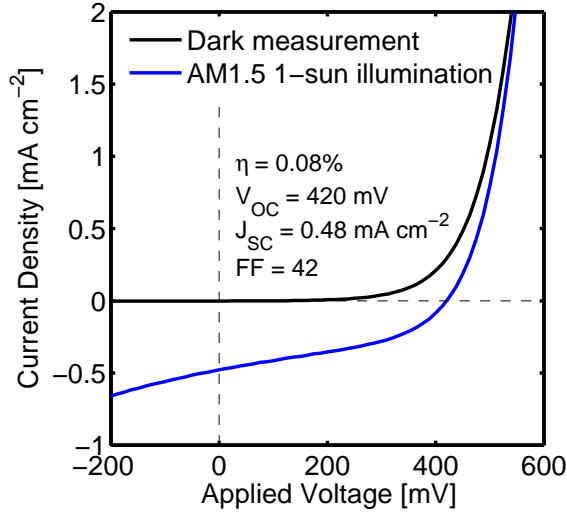


Figure 6.4: I-V response of the ZnSe/Zn₃P₂ heterojunction device under dark and AM1.5 1-sun illumination.

poorly doped or even intrinsic. It was later determined that the drastically reduced dopant activation of the Al:ZnSe grown on Zn₃P₂ initiated from the presence of an amorphous overlayer that remained on freshly-grown Zn₃P₂ surfaces. The presence of the overlayer was discovered in transmission electron micrographs of the ZnSe/Zn₃P₂ interface. Figures 6.5a and 6.5b display low-resolution and high-resolution micrographs of an interface grown at 200 °C. A 2 ~ 3 nm thick amorphous layer is clearly present at the interface. The composition of the overlayer was later determined by XPS analysis to be primarily elemental phosphorus (Figure 6.5c). Clearly, the phosphorus overlayer observed previously in the STM and XPS studies discussed in section 3.2 persists despite exposure of the surface to a Zn and Se vapor flux during ZnSe film growth.

In an attempt to improve the ZnSe doping, several alternative growth strategies were investigated. Those strategies are summarized in Figure 6.6 and include:

- (i) Exposure of the freshly grown Zn₃P₂ surface prior to either atomic Zn metal flux or atomic H flux at elevated temperatures in order to remove

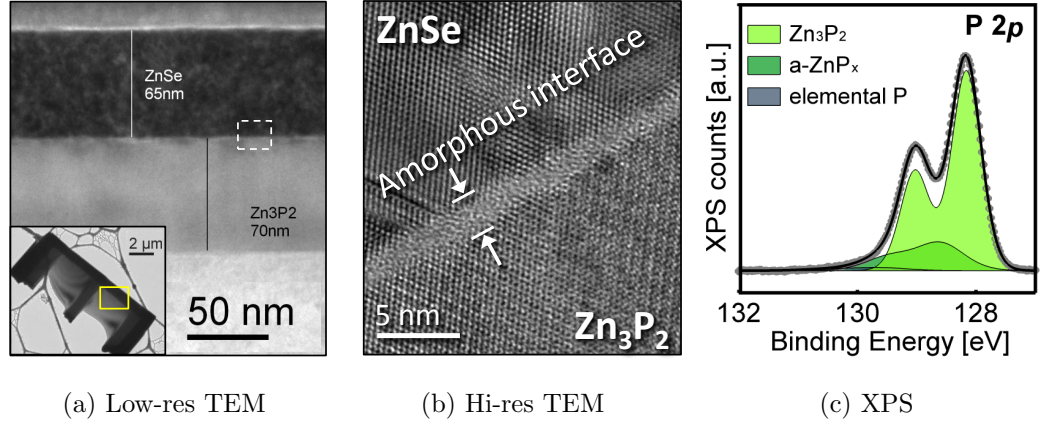


Figure 6.5: (a) Low-resolution and (b) high-resolution transmission electron micrographs and (c) XPS of the untreated ZnSe/Zn₃P₂ heterojunction interface.

the amorphous phosphorus layer, leaving behind a crystalline Zn₃P₂ surface for subsequent ZnSe growth.

- (ii) Growth of a ZnS buffer layer prior ZnSe deposition, possibly improving ZnSe epitaxy and increasing Al-dopant activation.
- (iii) Switch to a “superstrate” device configuration thereby completely avoiding any issue with the growth and doping of ZnSe on the Zn₃P₂ surface.

While strategies (i) and (ii) did appear to have some effect on the crystallinity of the ZnSe layer when grown on Zn₃P₂ (as observed by HRXRD), they had little impact on the Al-dopant activation. The implementation and results of strategy (iii) are discussed in detail in section 6.2.

6.2 Superstrate ZnSe devices

The decision to fabricate a Zn₃P₂/ZnSe superstrate device was motivated by the difficulty in growing heavily-doped ZnSe on the Zn₃P₂ surface. A superstrate device allows one to avoid these issues by growing doped, pseudomorphic

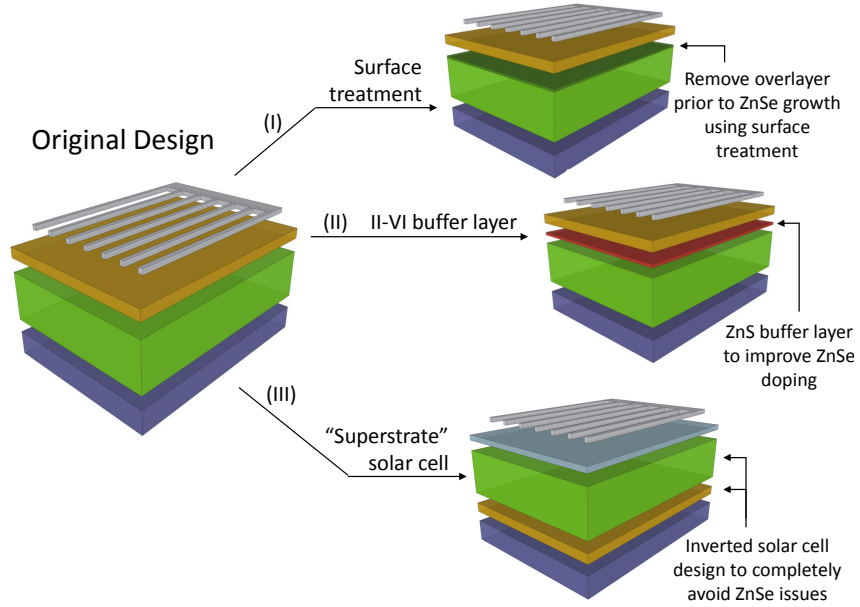


Figure 6.6: Alternative strategies for improving the growth and doping of the ZnSe emitter, including: (i) surface treatments prior to growth, (ii) a ZnS buffer layer, and (iii) a superstrate configuration.

ZnSe films directly on GaAs followed by the deposition of epitaxial Zn_3P_2 . The devices can then be evaluated for photovoltaic performance using back-side illumination. While back-side illuminated devices will be limited in efficiency due to the non-ideal location of the photogenerated carriers near the back surface, they offer a chance to probe the electronic properties of the $\text{Zn}_3\text{P}_2/\text{ZnSe}$ interface. There is also the potential for front-side characterization by removing the GaAs substrate from the rest of the device via either chemical etching or epitaxial lift-off techniques.

6.2.1 $\text{Zn}_3\text{P}_2/\text{ZnSe}$ film characterization

The first step in producing a superstrate device was to study the growth of Zn_3P_2 films on the ZnSe(001) surface. A procedure identical to that used for the growth of Zn_3P_2 on GaAs(001) surface (as described in subsection 2.4.3) was adopted. The thickness of the initial ZnSe film was limited to 300 nm

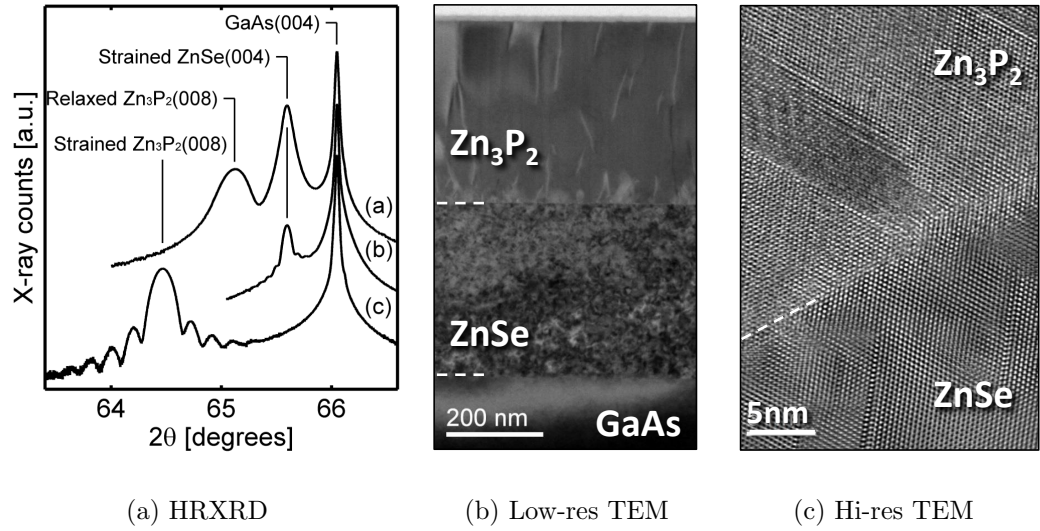


Figure 6.7: (a) High-resolution XRD and (b) low-resolution and (c) high-resolution transmission electron micrographs of the superstrate Zn₃P₂/ZnSe heterojunction interface.

in order to avoid relaxation and the surface was unmodified prior to Zn₃P₂ growth. A substrate temperature of 200 °C and Zn₃P₂ BEP of $\sim 1 \times 10^{-6}$ Torr was employed for all growths.

Figure 6.7 displays high-resolution XRD and TEM of a 400 nm Zn₃P₂ film grown on a pseudomorphic ZnSe film. The XRD displays a comparison of the Zn₃P₂/ZnSe stack with individual pseudomorphic ZnSe and Zn₃P₂ films grown directly on GaAs(001). The Zn₃P₂ grown on ZnSe was found to be crystalline and oriented along the (001) direction, similar to the growth on GaAs. However, the Zn₃P₂ was in a relaxed state and was not strained by the ZnSe in-plane lattice parameter as observed by the (008) peak position. The FWHM of the Zn₃P₂(008) peak was also broader, indicating lower crystalline quality likely due to a higher concentration of microscopic defects.

The TEM images displayed in Figures 6.7b and 6.7c verified the growth of oriented Zn₃P₂ on ZnSe(001). High-resolution images of the area between the two materials showed a relatively clean, smooth growth interface which

was void of any amorphous material. There were a large number of crystalline defects in the film which initiated near the growth interface. These defects included crystalline twins, stacking faults, and threading dislocations. The defects support the XRD observation that the Zn_3P_2 film relaxed almost immediately to its native lattice constant. It remains to be studied whether or not the higher number of defects has any major effect on the electronic properties of the Zn_3P_2 films.

6.2.2 Contact measurements

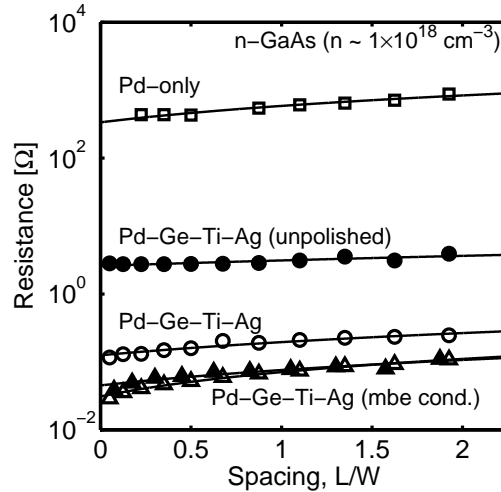
Before superstrate devices could be fully fabricated, it was necessary to test the ohmic contact between n-ZnSe and n-GaAs. In order to do so, transmission line measurements (TLM) were first performed to verify metallic ohmic contacts to both n-ZnSe and n-GaAs. Fortunately, ohmic contacts to both materials have been reported previously.^{130,131} Afterward, the ohmic contact at the n-ZnSe/n-GaAs interface could be assessed.

Pd metal and Pd-Ge alloy contacts were tested as ohmic contacts to heavily-doped GaAs substrates ($n \sim 3 \times 10^{18} \text{ cm}^{-3}$). A Ti diffusion barrier (30 nm) and thick Ag layer (1 μm) were incorporated into the Pd-Ge contact in order to decrease oxidation and parasitic resistances. All contacts were annealed at the MBE conditions for the atomic-H treatment (450 °C for 5 min under ultra-high vacuum). TLM data as well as specific contact resistances for the various contact recipes are displayed in Figure 6.8a and Table 6.8b, respectively. Pd metal alone made poor ohmic contact to n-GaAs, even after annealing. However, contact resistances of $\sim 1 \times 10^{-4} \Omega\text{-cm}^2$ could be reproducibly achieved with the Pd-Ge alloyed contact.

Pt metal (with and without a Ni adhesion layer), Ag metal, and ITO contacts were tested on ZnSe epilayers grown with varying Al-dopant incorporation. Once again, a thick layer of Ag metal was added to all of the transmission lines. Contact resistances were measured as is, as well as after a 200 °C anneal under vacuum for specific samples. TLM data and specific

contact resistances for the various contact recipes are displayed in Figure 6.9a and Table 6.9b, respectively. Ag, Pt, and Ni-Pt all demonstrated contact resistances of $\lesssim 1 \times 10^{-2} \Omega\text{-cm}^2$ to ZnSe films with doping of $> 1 \times 10^{18} \text{ cm}^{-3}$ (the medium- and highly-doped samples). The vacuum anneal did little or nothing to improve the metal contact resistance to ZnSe films. On the other hand, the as-deposited ITO contacts to ZnSe were considerably more resistive ($\rho_c > 1 \Omega\text{-cm}^2$) but improved drastically upon anneal at 200 °C. The resulting contact resistances were on the order of $10^{-2} \Omega\text{-cm}^2$ for heavily-doped ZnSe samples. Annealing any of the contacts at temperatures > 250 °C resulted in deactivation of the ZnSe doping and therefore increased the contact resistance.

The contact resistance between n-ZnSe epilayers and n-GaAs wafers was estimated by measuring the resistance through contact pads of known area. 1 mm \times 1 mm contact pads of Ni-Pt-Ag were deposited on doped ZnSe epilayers grown directly on n-GaAs substrates. The n-GaAs had a Pd-Ge contact prior



(a) n-GaAs TLM data

Contact recipe	Resistance, ρ_c [$\Omega\text{-cm}^2$]
Pd-only	$1.2 (\pm 0.3)$
Pd-Ge-Ti-Ag (unpolish. surf.)	$3.9 (\pm 2.9) \times 10^{-5}$
Pd-Ge-Ti-Ag	$2.9 (\pm 1.3) \times 10^{-4}$
Pd-Ge-Ti-Ag [†] (unpolish. surf.)	$1.4 (\pm 0.4) \times 10^{-4}$
Pd-Ge-Ti-Ag [†]	$1.3 (\pm 0.5) \times 10^{-4}$

[†] Annealed under MBE conditions.

(b) Contact resistance

Figure 6.8: (a) Transmission line measurements for Pd and Pd-Ge contacts to heavily doped n-GaAs substrates. (b) A table of specific contact resistance for each contact recipe tested. All contacts were annealed at 425 °C under vacuum.

to ZnSe deposition. Dark I-V curves measured across the devices as well as estimated contact resistances are displayed in Figure 6.10a and Table 6.10b, respectively. Unfortunately, none of the ZnSe/GaAs interfaces tested were completely ohmic. The measured I-V curves demonstrated rectifying behavior across the interface. Estimated contact resistances even for very heavily-doped ZnSe epilayers were $\sim 100 \Omega\text{-cm}^2$ or greater. Such a high contact resistance would be detrimental to the performance of a PV device.

6.2.3 Mesa device characterization

Since the contact resistance between n-ZnSe epilayers and the n-GaAs substrate was too high to fabricate superstrate devices with an emitter contact through the GaAs wafer, a mesa device architecture was adopted. A schematic

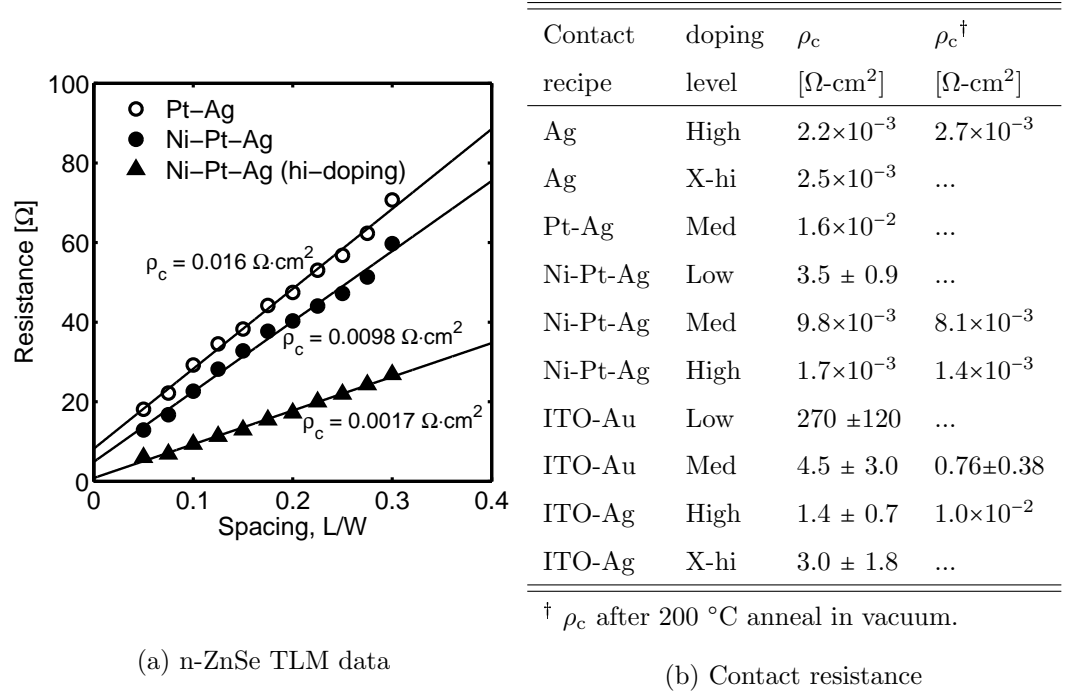
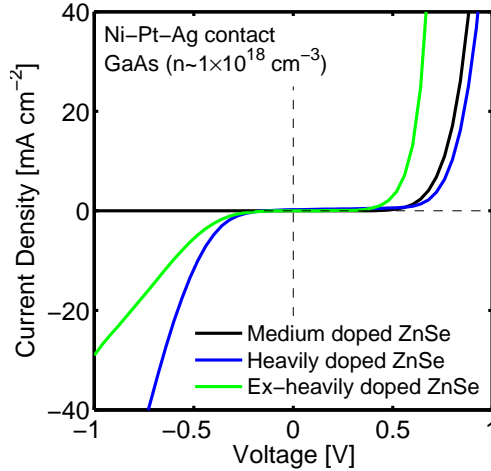


Figure 6.9: (a) Transmission line measurements for Pt, Ni-Pt, and ITO contacts to n-ZnSe epilayers with variable Al-dopant incorporation. (b) A table of specific contact resistance for each contact recipe tested, before and after a 200 °C anneal.

of the mesa architecture is displayed in Figure 6.11. An emitter contact is made directly to the ZnSe film surface in exposed areas outside of the active absorber area. The Zn_3P_2 absorber layer is contacted using a transparent ITO layer.

Two different methods were implemented to fabricate ITO/ Zn_3P_2 /ZnSe mesa devices. First, an etch-thru process was used to remove the ITO and Zn_3P_2 layers from a full device stack. The complete device stack prior to etching included a 1 μm thick, heavily-doped ZnSe layer, a 1.5 ~ 2 μm Zn_3P_2 absorber layer, and 100 nm of ITO. The ZnSe epilayers were found to be indefinitely stable in aqueous H_2SO_4 solutions of up to 1.0 M concentration whereas both ITO and Zn_3P_2 were rapidly dissolved. A 0.1 M H_2SO_4 solution was used for the final etch-thru process since it was found to result in better defined mesa areas. An additional etch solution was attempted with 2% H_2O_2 added to 0.1 M H_2SO_4 . Post-etching, Ni-Pt contacts were deposited onto the exposed ZnSe emitter, completing the device.



(a) n-ZnSe/n-GaAs I-V curves

Growth temp. [°C]	ZnSe doping	Device resistance [Ω]	Est. ρ_c [$\Omega\text{-cm}^2$]
200	Low	$>1 \times 10^7$...
200	Med	$\sim 1 \times 10^6$	$\sim 1 \times 10^4$
200	High	$\sim 1 \times 10^4$	~ 100
200	X-High	$\sim 3 \times 10^4$	~ 300
250	High	$>1 \times 10^7$...

(b) Contact resistance

Figure 6.10: Current-voltage measurements for estimating the contact resistance between n-ZnSe/n-GaAs for various ZnSe dopant incorporation. 1 mm \times 1 mm Pt-Ni contact pads were deposited on the ZnSe layer to define the contact area.

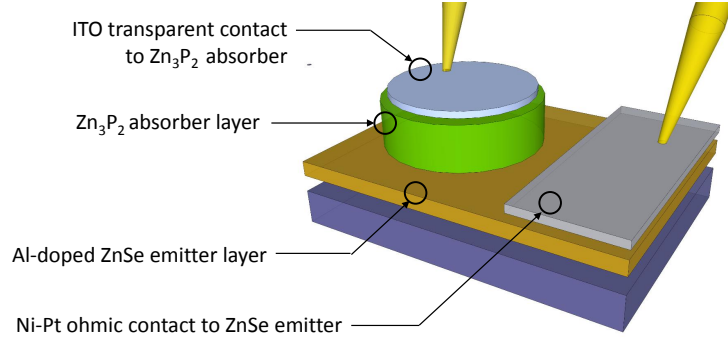


Figure 6.11: Schematic of the mesa architecture for a superstrate $\text{Zn}_3\text{P}_2/\text{ZnSe}$ heterojunction PV device with ITO transparent back contact for back-side illumination measurements.

The second fabrication method involved using a physical mask to define the active absorber area during film growth. After the ZnSe emitter layer was grown, the sample was removed from the MBE chamber and a $0.5 \text{ cm} \times 1.0 \text{ cm}$ stainless steel mask was placed over the film. The Zn_3P_2 epilayer was then deposited through the mask. An additional mask with smaller active area was placed over the Zn_3P_2 mesa prior to ITO sputter deposition in order to avoid electrical contact between the ITO and ZnSe emitter. All active layer thicknesses for the masked devices were identical to those of the etched devices.

The current-voltage characteristics of the mesa devices tested under dark and 1-sun illumination are displayed in Figure 6.12. All of the devices were found to be badly shunted with lower shunt resistance observed under illumination. Furthermore, none of the devices demonstrated any photogenerated current under illumination. However, the masked-growth device displayed slight diode behavior, but it was far from ideal. It was presumed that the shunting for the etched mesa devices was due to either metal precipitates or oxide on the surface of the etched Zn_3P_2 providing a conductive path for current flow. It is less clear what caused shunting in the masked-growth devices. It is possible that a ZnO layer formed at the ZnSe surface during placement of the Zn_3P_2 growth mask which resulted in a shunt.

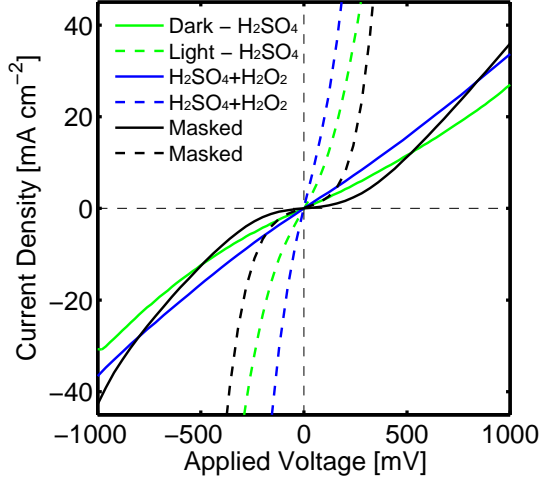


Figure 6.12: Current-voltage (I-V) measurements for etched-thru and masked-growth $\text{Zn}_3\text{P}_2/\text{ZnSe}$ mesa devices under dark conditions and AM1.5 1-sun illumination. All devices were heavily shunted, however, the masked devices showed some diode behavior.

6.3 Alternative: Graphene/ Zn_3P_2 Field-effect solar cell

In addition to II-VI/ Zn_3P_2 heterojunction devices, an alternative Zn_3P_2 device with a field-effect gated, graphene Schottky contact was explored.¹³² This work was done in collaboration with Oscar Vazquez-Mena of the Zettl research group at the University of California, Berkeley. Our contribution was the thick Zn_3P_2 epitaxial film. The Zettl group performed all subsequent device fabrication and testing. The principle of the field-effect solar cell is to use a transparent top gate to modulate the work function of the graphene Schottky contact. By tuning the graphene Fermi-level via the applied gate voltage, the built-in voltage between the graphene and Zn_3P_2 absorber layer is modified.

A schematic of the graphene/ Zn_3P_2 device is displayed in Figure 6.13. The device is fabricated on a 7 μm thick Zn_3P_2 film grown on a semi-insulating GaAs substrate. A single layer of graphene was transferred using conventional

techniques onto the Zn_3P_2 . The contact area of the graphene was determined by an insulating oxide with a $400\text{ }\mu\text{m} \times 400\text{ }\mu\text{m}$ window. An additional oxide layer was deposited above the graphene in addition to a semi-transparent Au gate contact (Au-G). Ohmic contacts were made to the graphene and Zn_3P_2 layers using Au and Ag pads, respectively.

Capacitance-voltage (C-V) measurements were performed in order to determine the band alignment between the graphene contact and Zn_3P_2 absorber under different gating conditions. Prior to equilibrium, the graphene has a work function of $\sim 4.5\text{ eV}$, whereas the Zn_3P_2 has a work function of nearly 5.1 eV assuming p-type conductivity (Figure 6.14a). Once contacted, the Zn_3P_2 surface becomes slightly depleted, resulting in a built-in potential between the graphene and Zn_3P_2 of $V_{\text{bi}} = 0.32\text{ V}$ (Schottky band-bending shown in Figure 6.14b). When a positive bias is applied to the gate, the work function of graphene increases which causes greater depletion of the Zn_3P_2 surface. A positive gate bias of $V_{\text{G}} = 1\text{ V}$ resulted in a measured built-in potential of $V_{\text{bi}} = 0.55\text{ V}$ (Figure 6.14c). Finally, when a negative gate bias ($V_{\text{G}} = -1\text{ V}$) is applied to the graphene, the graphene work function is instead decreased and the Zn_3P_2 bands are flattened resulting in a smaller device potential of $V_{\text{bi}} = 0.04\text{ V}$ (band-bending not shown).

The trends in the barrier height of the graphene/ Zn_3P_2 Schottky observed by C-V measurements were reproduced in the device's photovoltaic performance. An image of the active area and contact pads of the $400\text{ }\mu\text{m} \times 400$

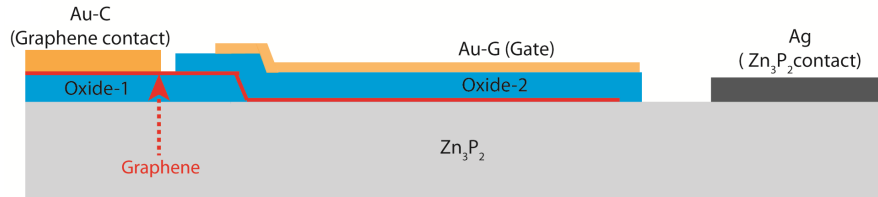


Figure 6.13: Cross-sectional schematic of the gated graphene/ Zn_3P_2 Schottky device.

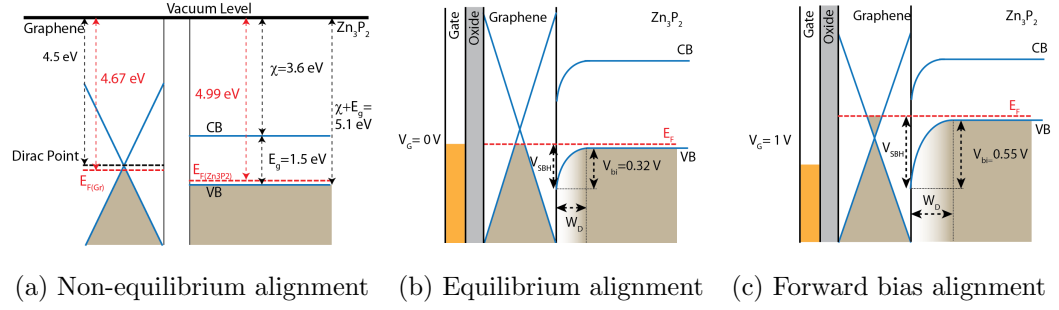


Figure 6.14: Band diagrams for the gated graphene- Zn_3P_2 Schottky device under (a) ideal - unbiased, (b) measured - unbiased, and (c) measured - forward biased conditions.

μm photovoltaic device is displayed in Figure 6.15 (a). The I-V response of the device under AM1.5 1-sun solar illumination at different gate biases is displayed in Figure 6.15 (b). An increase in V_{oc} up to 0.53 V was observed with a 2 V gate bias. A solar conversion efficiency of 1.9% was obtained under these conditions. Increases in efficiency could be obtained by optimizing the absorber thickness as well as reducing reflection losses from the top gate contact. However, the graphene/ Zn_3P_2 field-effect solar cell is an excellent proof-of-principle demonstration of an alternative PV device design.

6.4 Conclusions

We have demonstrated several different device architectures incorporating an epitaxial Zn_3P_2 absorber layer. The $\text{ZnS}/\text{Zn}_3\text{P}_2$ device performance corroborated the band alignment measurements made earlier, demonstrating record V_{oc} 's but limitations in current collection due to transport issues. An alternative $\text{Mg}/\text{ZnS}/\text{Zn}_3\text{P}_2$ MIS device was proposed, which alleviated the current limitations of the ZnS heterojunction, but was also limited in attainable voltage. Major challenges were faced with the ZnSe heterojunction devices. Doping in the ZnSe emitter was extremely difficult to control when grown di-

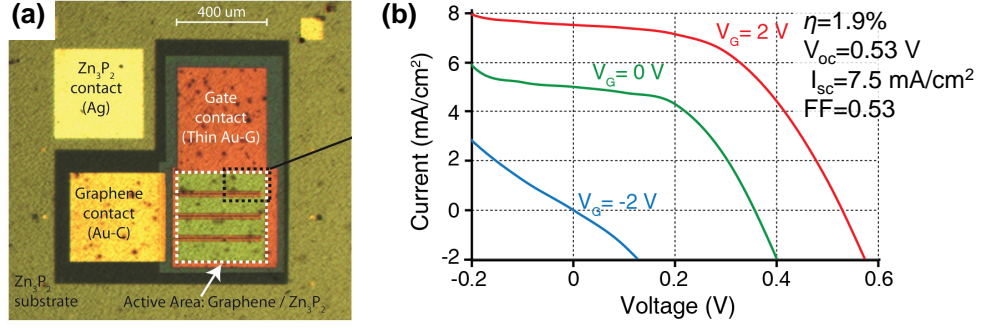


Figure 6.15: (a) Top-view image of the 400 μm × 400 μm active-area graphene/Zn₃P₂ photovoltaic device with gate, emitter, and back contacts. (b) Current-voltage (I-V) characteristics of the graphene/Zn₃P₂ device under AM1.5 1-sun illumination with different applied gate biases.

rectly on the Zn₃P₂ surface. Several attempts were made to solve the ZnSe doping issue, including surface treatments, buffer layers, and an alternative superstrate device architecture. While none of these solutions were successful, there is still a large amount of work to be done on the ZnSe/Zn₃P₂ heterojunction PV device. Finally, an alternative device design incorporating a field-effect gated, graphene/Zn₃P₂ Schottky contact was proposed and successfully demonstrated.

CHAPTER 7

Final remarks

The goal of this work was to develop a thin-film, heterojunction photovoltaic device incorporating a α - Zn_3P_2 absorber. We identified Zn_3P_2 as an excellent candidate material for earth-abundant photovoltaic applications based on its bulk electronic properties as well as abundance of its constituents elements. We also identified several key challenges regarding Zn_3P_2 as a photovoltaic material, in particular the fact that the material demonstrates intrinsic p-type conductivity, limiting devices to either Schottky or heterojunction designs, and exhibits surfaces and interfaces with poor electronic quality. For these reasons, we targeted a heterojunction structure with a surface passivating II-VI semiconductor as the n-type emitter.

Our first goal was to develop a process for growing extremely high-quality thin films of Zn_3P_2 . This was done using compound-source molecular-beam epitaxy. The source material for the epitaxial growth was synthesized from the elements using a physical-vapor transport process developed previously. Subliming the synthesized material in the molecular-beam epitaxy process, we succeeded in growing epitaxial Zn_3P_2 films with controlled orientation and

optoelectronic properties. In fact, this was the first demonstration of pseudomorphic growth of Zn_3P_2 on $\text{GaAs}(001)$, allowing us to study the effects of strain relaxation within the material.

Once we obtained high-quality Zn_3P_2 epilayers, our next goal was to search for a suitable n-type emitter. We chose a small group of wide band gap II-VI semiconductors with favorable electronic properties, including ZnS , ZnSe , CdS , and ZnO . Similar to Zn_3P_2 , the growth and doping of the II-VI materials was studied using molecular-beam epitaxy as well as magnetron sputtering. We then employed high-resolution x-ray photoelectron spectroscopy to determine the energy-band alignment for each heterojunction partner with Zn_3P_2 using the established method of Kraut et al. From these measurements, we were able to explain a number of previously reported device results for Zn_3P_2 heterojunction solar cells. In addition, we identified the $\text{ZnSe}/\text{Zn}_3\text{P}_2$ interface as having the optimal band alignment for a heterojunction photovoltaic device.

The final step in our work was to study the device properties of epitaxial II-VI/ Zn_3P_2 heterojunctions and how their performance correlates to the measured band alignments. Focus was given to ZnS and ZnSe emitters based on their interesting band alignments. They were implemented in two different device architectures: superstrate and substrate designs. The substrate designs were found to be limited by several factors, including ambiguity in the quality of the back contact between GaAs and the Zn_3P_2 absorber and difficulty in growing well-doped ZnSe on the Zn_3P_2 surface. Nevertheless, we were able to demonstrate a record open-circuit voltage for a $\text{ZnS}/\text{Zn}_3\text{P}_2$ device, despite the fact that it was severely limited in current due to its type-I band alignment. We also showed that the current issue could be overcome by employing a metal-insulator-semiconductor structure, at the sacrifice of some voltage. Alternative device designs, such as a gated graphene Schottky, were also demonstrated as proof of concept.

We have laid the groundwork for developing efficient thin-film photovoltaic devices comprised of II-VI/ Zn_3P_2 heterojunctions. However, there are still

many unknowns that require investigation. Our understanding of the bulk properties and heterojunction interfaces of Zn_3P_2 , as well as a variety of other potential earth-abundant semiconductors, is still in its infancy compared to more advanced semiconductors like Si and GaAs. Much remains to be studied regarding the doping of Zn_3P_2 . Our attempts to produce n-type conductivity in Zn_3P_2 using Al and S dopants were not successful. More advance methods of compound doping may be necessary. n-type doping would not only allow for fabrication of a Zn_3P_2 homojunction device, but would also provide information about the properties of electron carriers within Zn_3P_2 , which are at the moment poorly understood.*

Further work also needs to be performed on the development of ZnSe heterojunction devices. Our band alignment measurements clearly show that the energetics of the ZnSe/ Zn_3P_2 interface are ideal for photovoltaic applications. Only engineering of the ZnSe growth and doping remains an obstacle. More advanced surface preparation techniques and greater control over the heterojunction growth interface using a separate source growth would likely result in a functional device. If these issues can be resolved, it is likely that Zn_3P_2 could become an efficient, inexpensive, and extremely scalable alternative to current photovoltaic technologies like Si.

*For instance, we only have estimates of the electron mobility of Zn_3P_2 , the consensus being that it is $\sim 1000 \text{ cm}^2 \text{ V}^{-1} \text{ s}^{-1}$. However, no concrete measurements of this value are available.

Bibliography

- [1] *Annual Energy Review 2011*. Energy Information Administration, Bernan Association, 2012. (U S).
- [2] V. Smil, *General energetics: energy in the biosphere and civilization*. Wiley, 1991.
- [3] “PV Facts: What is the energy payback for PV?,” 2004.
- [4] C. Honsberg and S. Bowden, “Photovoltaic Educator Network,” March 5, 2014 2014.
- [5] S. Sze and K. Ng, *Physics of Semiconductor Devices*. Wiley, 2006.
- [6] M. A. Green, K. Emery, Y. Hishikawa, W. Warta, and E. D. Dunlop, “Solar cell efficiency tables (version 43),” *Progress in Photovoltaics: Research and Applications*, vol. 22, no. 1, pp. 1–9, 2014.
- [7] A. Luque and S. Hegedus, *Handbook of Photovoltaic Science and Engineering*. Wiley, 2003.
- [8] M. T. Winkler, W. Wang, O. Gunawan, H. J. Hovel, T. K. Todorov, and D. B. Mitzi, “Optical designs that improve the efficiency of

- $\text{Cu}_2\text{ZnSn}(\text{S,Se})_4$ solar cells,” *Energy and Environmental Science*, vol. 7, no. 3, pp. 1029–1036, 2014.
- [9] M. E. Schlesinger, “The thermodynamic properties of phosphorus and solid binary phosphides,” *Chemical Reviews*, vol. 102, no. 11, pp. 4267–4302, 2002.
- [10] J. L. Deiss, B. Elidrissi, M. Robino, and R. Weil, “Amorphous thin films of Zn_3P_2 : Preparation and characterization,” *Applied Physics Letters*, vol. 49, no. 15, pp. 969–970, 1986.
- [11] A. Weber, P. Sutter, and H. von Kanel, “Growth of amorphous zinc phosphide films by reactive radio frequency sputtering,” *Journal of Non-Crystalline Solids*, vol. 164166, Part 1, no. 0, pp. 79–82, 1993.
- [12] A. Weber, P. Sutter, and H. von Kanel, “Optical, electrical, and photo-electrical properties of sputtered thin amorphous Zn_3P_2 films,” *Journal of Applied Physics*, vol. 75, no. 11, pp. 7448–7455, 1994.
- [13] M. von Stackelberg, “XRD of Zn_3P_2 ,” *Zeitschrift fuer Physikalische Chemie, Abteilung B: Chemie der Elementarprozesse, Aufbau der Materie*, vol. 28, pp. 427–460, 1935.
- [14] I. E. Zanin, K. B. Aleinikova, M. M. Afanasiev, and M. Y. Antipin, “Structure of Zn_3P_2 ,” *Journal of Structural Chemistry*, vol. 45, no. 5, pp. 844–848, 2004.
- [15] R. C. Schoonmaker, A. R. Venkitaraman, and P. K. Lee, “The vaporization of zinc phosphide,” *Journal of Physical Chemistry*, vol. 71, no. 8, pp. 2676–2683, 1967.
- [16] H. W. Hilton and W. H. Robison, “Fate of zinc phosphide and phosphine in the soil–water environment,” *Journal of Agricultural and Food Chemistry*, vol. 20, no. 6, pp. 1209–1213, 1972.

- [17] E. A. Fagen, “Optical properties of Zn_3P_2 ,” *Journal of Applied Physics*, vol. 50, no. 10, pp. 6505–6515, 1979.
- [18] W. Shockley and H. J. Queisser, “Detailed balance limit of efficiency of pn junction solar cells,” *Journal of Applied Physics*, vol. 32, no. 3, pp. 510–519, 1961.
- [19] J. P. Bosco, D. O. Scanlon, G. W. Watson, N. S. Lewis, and H. A. Atwater, “Energy-band alignment of II-VI/ Zn_3P_2 heterojunctions from x-ray photoemission spectroscopy,” *Journal of Applied Physics*, vol. 113, no. 20, 2013.
- [20] J. Pawlikowski, J. Misiewicz, and N. Mirowska, “Direct and indirect optical transitions in Zn_3P_2 ,” *Journal of Physics and Chemistry of Solids*, vol. 40, no. 12, pp. 1027–1033, 1979.
- [21] B. O. Sundström, “A determination of the band gap of Zn_3P_2 ,” *Physica Scripta*, vol. 24, no. 2, p. 444, 1981.
- [22] G. M. Kimball, A. M. Miller, N. S. Lewis, and H. A. Atwater, “Photoluminescence-based measurements of the energy gap and diffusion length of Zn_3P_2 ,” *Applied Physics Letters*, vol. 95, p. 112103, 2009.
- [23] N. Wyeth and A. Catalano, “Spectral response measurements of minority carrier diffusion length in Zn_3P_2 ,” *Journal of Applied Physics*, vol. 50, no. 3, pp. 1403–1407, 1979.
- [24] M. Bhushan and A. Catalano, “Polycrystalline Zn_3P_2 schottky barrier solar cells,” *Applied Physics Letters*, vol. 38, no. 1, pp. 39–41, 1981.
- [25] G. M. Kimball, J. P. Bosco, A. M. Muller, S. F. Tajdar, B. S. Brunschwig, H. A. Atwater, and N. S. Lewis, “Passivation of Zn_3P_2 substrates by aqueous chemical etching and air oxidation,” *Journal of Applied Physics*, vol. 112, no. 10, p. 106101, 2012.

- [26] G. Brown, V. Faifer, A. Pudov, S. Anikeev, E. Bykov, M. Contreras, and J. Wu, “Determination of the minority carrier diffusion length in compositionally graded Cu(In,Ga)Se₂ solar cells using electron beam induced current,” *Applied Physics Letters*, vol. 96, no. 2, 2010.
- [27] A. LastrasMartnez, P. M. Raccach, and R. Triboulet, “Minority carrier diffusion length measurements in CdTe by a photocurrent technique,” *Applied Physics Letters*, vol. 36, no. 6, pp. 469–471, 1980.
- [28] T. Suda, K. Kakishita, H. Sato, and K. Sasaki, “N-type zinc phosphide grown by molecular beam epitaxy,” *Applied Physics Letters*, vol. 69, no. 16, pp. 2426–2428, 1996.
- [29] M. S. Casey, A. L. Fahrenbruch, and R. H. Bube, “Properties of zinc phosphide junctions and interfaces,” *Journal of Applied Physics*, vol. 61, no. 8, pp. 2941–2946, 1987.
- [30] P. S. Nayar and A. Catalano, “Zinc phosphide - zinc oxide heterojunction solar-cells,” *Applied Physics Letters*, vol. 39, no. 1, pp. 105–107, 1981.
- [31] S. B. Demers and A. Van de Walle, “Intrinsic defects and dopability of zinc phosphide,” *Physical Review B*, vol. 85, no. 19, p. 195208, 2012.
- [32] W. Yin and Y. Yan, “The electronic properties of point defects in earth-abundant photovoltaic material Zn₃P₂: A hybrid functional method study,” *Journal of Applied Physics*, vol. 113, no. 1, p. 013708, 2013.
- [33] M. Bhushan, “Schottky solar cells on thin polycrystalline Zn₃P₂ films,” *Applied Physics Letters*, vol. 40, no. 1, pp. 51–53, 1982.
- [34] T. Suda, M. Suzuki, and S. Kurita, “Polycrystalline Zn₃P₂/indium-tin oxide solar-cells,” *Japanese Journal of Applied Physics part 2*, vol. 22, no. 10, pp. L656–L658, 1983.

- [35] T. Suda, A. Kuroyanagi, and S. Kurita, “Photovoltaic and electrical properties of $\text{Zn}_3\text{P}_2/\text{CdS}$ heterojunctions,” *Technical Digest, International PVSEC-1, Kobe, Japan*, pp. 381–384, 1984.
- [36] M. Bhushan and J. D. Meakin, “ Zn_3P_2 as an improved semiconductor for photovoltaic solar cells: Final report, April 1983 – March 1984,” report, University of Delaware, Institute of Energy Conversion; Solar Energy Research Institute, 1985.
- [37] J. P. Bosco, S. B. Demers, G. M. Kimball, N. S. Lewis, and H. A. Atwater, “Band alignment of epitaxial $\text{ZnS}/\text{Zn}_3\text{P}_2$ heterojunctions,” *Journal of Applied Physics*, vol. 112, no. 9, p. 093703, 2012.
- [38] N. C. Wyeth and A. Catalano, “Barrier heights of evaporated metal contacts on Zn_3P_2 ,” *Journal of Applied Physics*, vol. 51, no. 4, pp. 2286–2288, 1980.
- [39] L. L. Kazmerski, P. J. Ireland, and A. Catalano, “Surface and interface properties of Zn_3P_2 solar cells,” *Journal of Vacuum Science and Technology*, vol. 18, no. 2, pp. 368–371, 1981.
- [40] G. M. Kimball, N. S. Lewis, and H. A. Atwater, “Mg doping and alloying in Zn_3P_2 heterojunction solar cells,” in *Photovoltaic Specialists Conference (PVSC), 2010 35th IEEE*, pp. 001039–001043.
- [41] A. Catalano and R. B. Hall, “Defect dominated conductivity in Zn_3P_2 ,” *Journal of Physics and Chemistry of Solids*, vol. 41, no. 6, pp. 635–640, 1980.
- [42] S. Fuke, S. Kawarabayashi, K. Kuwahara, and T. Imai, “Some properties of Zn_3P_2 polycrystalline films prepared by hot-wall deposition,” *Journal of Applied Physics*, vol. 60, no. 7, pp. 2368–2371, 1986.
- [43] S. Fuke, T. Imai, S. Okuyama, and K. Kuwahara, “Properties of zinc phosphide (Zn_3P_2) thin films prepared by hotwall technique under high

Sb vapor pressure,” *Journal of Applied Physics*, vol. 62, no. 3, pp. 1127–1129, 1987.

- [44] S. Fu, T. Imai, K. Kawasaki, and K. Kuwahara, “Substrate effect on the deposition of Zn_3P_2 thin films prepared by a hot-wall method,” *Journal of Applied Physics*, vol. 65, no. 2, pp. 564–566, 1989.
- [45] V. S. Babu, P. R. Vaya, and J. Sobhanadri, “Doping of Zn_3P_2 thin films during growth using the hot wall deposition technique and some properties of the grown films,” *Semiconductor Science and Technology*, vol. 4, no. 7, p. 521, 1989.
- [46] J. L. Deiss, B. Eli-Drissi, M. Robino, M. Tapiero, J. P. Zielinger, and R. Weil, “Amorphous thin films of Zn_3P_2 ,” *Physica Scripta*, vol. 37, no. 4, p. 587, 1988.
- [47] S. Sudhakar and K. Baskar, “Influence of cooling rate on the liquid-phase epitaxial growth of Zn_3P_2 ,” *Journal of crystal growth*, vol. 310, no. 11, pp. 2707–2711, 2008.
- [48] T. L. Chu, S. S. Chu, K. Murthy, E. D. Stokes, and P. E. Russell, “Deposition and properties of zinc phosphide films,” *Journal of Applied Physics*, vol. 54, no. 4, pp. 2063–2068, 1983.
- [49] E. Papazoglou and T. W. F. Russell, “Chemical vapor deposition of zinc phosphide thin films,” *Journal of Vacuum Science and Technology A*, vol. 5, no. 6, pp. 3378–3382, 1987.
- [50] T. Suda and K. Kakishita, “Epitaxial growth of zinc phosphide,” *Journal of applied physics*, vol. 71, no. 6, pp. 3039–3041, 1992.
- [51] K. Kakishita, K. Aihara, and T. Suda, “ Zn_3P_2 photovoltaic film growth for $\text{Zn}_3\text{P}_2/\text{ZnSe}$ solar-cell,” *Solar Energy Materials and Solar Cells*, vol. 35, no. 1-4, pp. 333–340, 1994.

- [52] D. Smith, *Thin-Film Deposition: Principles and Practice*. McGraw-Hill Education, 1995.
- [53] A. Catalano, “The growth of large Zn_3P_2 crystals by vapor transport,” *Journal of Crystal Growth*, vol. 49, no. 4, pp. 681–686, 1980.
- [54] F. C. Wang, A. L. Fahrenbruch, and R. H. Bube, “Electrical properties of Zn_3P_2 single crystals,” *Journal of Electronic Materials*, vol. 11, no. 1, pp. 75–88, 1982.
- [55] D. Decroix, V. Muoz, and A. Chevy, “Growth and electrical properties of Zn_3P_2 single crystals and polycrystalline ingots,” *Journal of Materials Science*, vol. 22, no. 4, pp. 1265–1270, 1987.
- [56] G. M. Kimball, *Zn_3P_2 and Cu_2O substrates for solar energy conversion*. Thesis, 2012.
- [57] W. S. Holmes, “Heat of combustion of phosphorus and the enthalpies of formation of P_4O_{10} and H_3PO_4 ,” *Transactions of the Faraday Society*, vol. 58, no. 0, pp. 1916–1925, 1962.
- [58] X. J. Liu, X. Cai, J. S. Qiao, H. F. Mao, and N. Jiang, “The design of $\text{ZnS}/\text{Ag}/\text{ZnS}$ transparent conductive multilayer films,” *Thin Solid Films*, vol. 441, no. 1-2, pp. 200–206, 2003.
- [59] S. K. Hong, E. Kurtz, J. H. Chang, T. Hanada, M. Oku, and T. Yao, “Low stacking-fault density in ZnSe epilayers directly grown on epi-ready GaAs substrates without GaAs buffer layers,” *Applied Physics Letters*, vol. 78, no. 2, pp. 165–167, 2001.
- [60] Y. Ide and M. Yamada, “Role of Ga_2O in the removal of GaAs surface oxides induced by atomic hydrogen,” *Journal of Vacuum Science and Technology A*, vol. 12, no. 4, pp. 1858–1863, 1994.

- [61] C. M. Rouleau and R. M. Park, “GaAs substrate cleaning for epitaxy using a remotely generated atomic hydrogen beam,” *Journal of applied physics*, vol. 73, no. 9, pp. 4610–4613, 1993.
- [62] M. Yamada, Y. Ide, and K. Tone, “Effect of atomic hydrogen on GaAs (001) surface oxide studied by temperature-programmed desorption,” *Japanese journal of applied physics*, vol. 31, no. 8, pp. L1157–L1160, 1992.
- [63] M. Yamada and Y. Ide, “Direct observation of species liberated from GaAs native oxides during atomic hydrogen cleaning,” *Japanese Journal of Applied Physics*, vol. 33, no. 5A, p. L671, 1994.
- [64] J. M. Zuo, “Web Electron Microscopy Applications Software (WebE-MAPS),” 01 March, 2011. 2011.
- [65] Z. Zhu, T. Nomura, M. Miyao, and M. Hagino, “MBE growth mechanisms of ZnSe: Flux ratio and substrate temperature,” *Journal of Crystal Growth*, vol. 95, no. 14, pp. 529–532, 1989.
- [66] J. P. Bosco, S. F. Tajdar, and H. A. Atwater, “Molecular beam epitaxy of n-type ZnS: A wide band gap emitter for heterojunction PV devices,” in *Proc. IEEE Photovolt. Spec. Conf.*, 2012.
- [67] C. L. McCabe, “Equilibrium pressure measurements above ZnS from 680 °C to 825 °C,” *Journal of Metals*, vol. 6, no. 9, pp. 969–971, 1954.
- [68] M. Birkholz, P. Fewster, and C. Genzel, *Thin film analysis by X-ray scattering*. Vch Verlagsgesellschaft MbH, 2006.
- [69] S. Jeon, J. P. Bosco, S. S. Wilson, S. J. Rozeveld, H. Kim, and H. A. Atwater, “Growth mechanism and electronic structure of Zn₃P₂ on the Ga-rich GaAs(001) surface,” *Journal of Physical Chemistry C*, 2014.

- [70] S. Jeon, *Structure, Chemistry, and Energetics of Organic and Inorganic Adsorbates on Ga-rich GaAs and GaP(001) Surfaces*. Ph.d., 2013.
- [71] L. C. Cai, H. Chen, C. L. Bao, Q. Huang, and J. M. Zhou, “Transport properties of InAs epilayers grown on GaAs substrates by using the prelayer technique,” *Journal of Materials Science*, vol. 39, no. 7, pp. 2637–2640, 2004.
- [72] S. Kalem, “Transport properties of InAs epilayers grown by molecular beam epitaxy,” *Semiconductor Science and Technology*, vol. 5, p. S200, 1990.
- [73] T. Zhang, M. Debnath, S. K. Clowes, W. R. Branford, A. Bennett, C. Roberts, L. F. Cohen, and R. A. Stradling, “InSb epilayers on GaAs (100) for spintronic and magneto-resistive sensor applications,” *Physica E*, vol. 20, no. 3-4, pp. 216–219, 2004.
- [74] W. K. Fong, C. F. Zhu, B. H. Leung, and C. Surya, “High-mobility GaN epilayer grown by RF plasma-assisted molecular beam epitaxy on intermediate-temperature GaN buffer layer,” *Journal of Crystal Growth*, vol. 233, no. 3, pp. 431–438, 2001.
- [75] R. Jaszek, “Carrier scattering by dislocations in semiconductors,” *Journal of Materials Science - Materials in Electronics*, vol. 12, no. 1, pp. 1–9, 2001.
- [76] K. Jug, I. P. Gloriov, and B. Heidberg, “Miscibility of zinc sulfide and zinc phosphide,” *The Journal of Physical Chemistry B*, vol. 109, no. 46, pp. 21922–21927, 2005.
- [77] A. L. Fahrenbruch and R. H. Bube, *Fundamentals of solar cells: Photovoltaic Solar Energy Conversion*. Academic Press, 1983.
- [78] A. J. Nelson, L. L. Kazmerski, M. Engelhardt, and H. Hochst, “Valence-band electronic-structure of Zn_3P_2 as a function of annealing as studied

- by synchrotron radiation photoemission,” *Journal of Applied Physics*, vol. 67, no. 3, pp. 1393–1396, 1990.
- [79] R. K. Swank, “Surface properties of II-VI compounds,” *Physical Review*, vol. 153, no. 3, p. 844, 1967.
- [80] M. Kitagawa, Y. Tomomura, A. Suzuki, and S. Nakajima, “Homoepitaxial growth of low-resistivity Al-doped ZnS single-crystal films by molecular-beam epitaxy,” *Journal of Crystal Growth*, vol. 95, no. 1-4, pp. 509–511, 1989.
- [81] S. Yamaga, A. Yoshikawa, and H. Kasai, “Growth and properties of iodine-doped ZnS films grown by low-pressure MOCVD using ethyliodide as a dopant source,” *Journal of Crystal Growth*, vol. 106, no. 4, pp. 683–689, 1990.
- [82] G. A. Landis, J. J. Loferski, R. Beaulieu, P. A. Sekulamoise, S. M. Vernon, M. B. Spitzer, and C. J. Keavney, “Wide-bandgap epitaxial heterojunction windows for silicon solar-cells,” *IEEE Transactions on Electronic Devices*, vol. 37, no. 2, pp. 372–381, 1990.
- [83] Y. H. Kim, S. Y. An, J. Y. Lee, I. Kim, K. N. Oh, S. U. Kim, M. J. Park, and T. S. Lee, “Photoluminescence study on the effects of the surface of CdTe by surface passivation,” *Journal of Applied Physics*, vol. 85, no. 10, pp. 7370–7373, 1999.
- [84] T. Nakada, M. Mizutani, Y. Hagiwara, and A. Kunioka, “High-efficiency Cu(In,Ga)Se₂ thin-film solar cells with a CBD-ZnS buffer layer,” *Solar Energy Materials and Solar Cells*, vol. 67, no. 14, pp. 255–260, 2001.
- [85] J. M. Woodall, G. D. Pettit, T. Chappell, and H. J. Hovel, “Photoluminescent properties of GaAs-GaAlAs, GaAs-oxide, and GaAs-ZnS heterojunctions,” *Journal of Vacuum Science and Technology*, vol. 16, no. 5, pp. 1389–1393, 1979.

- [86] A. Pudov, J. Sites, and T. Nakada, “Performance and loss analyses of high-efficiency chemical bath deposition (CBD)-ZnS/Cu(In_{1-x}Ga_x)Se₂ thin-film solar cells,” *Japanese Journal of Applied Physics Part 2-Letters*, vol. 41, no. 6B, pp. L672–L674, 2002.
- [87] L. C. Olsen, R. C. Bohara, and D. L. Barton, “Vacuum-evaporated conducting ZnS films,” *Applied Physics Letters*, vol. 34, no. 8, pp. 528–529, 1979.
- [88] M. Yokoyama, K. Kashiro, and S. Ohta, “Molecular-beam epitaxial-growth of ZnS on a (100)-oriented Si substrate,” *Journal of Crystal Growth*, vol. 81, no. 1-4, pp. 73–78, 1987.
- [89] J. Kleiman, R. M. Park, and H. A. Mar, “On epilayer tilt in ZnSe/Ge heterostructures prepared by molecular-beam epitaxy,” *Journal of Applied Physics*, vol. 64, no. 3, pp. 1201–1205, 1988.
- [90] T. Yasuda, K. Hara, and H. Kukimoto, “Low resistivity Al-doped ZnS grown by MOVPE,” *Journal of Crystal Growth*, vol. 77, no. 1-3, pp. 485–489, 1986.
- [91] I. P. McClean and C. B. Thomas, “Conductive ZnS:Zn thin-films grown by molecular-beam deposition,” *Journal of Applied Physics*, vol. 72, no. 10, pp. 4749–4752, 1992.
- [92] Y. Takafumi, M. Yoichi, M. Yunosuke, and M. Shigeru, “Growth rate and sticking coefficient of ZnSe and ZnTe grown by molecular beam epitaxy,” *Japanese Journal of Applied Physics*, vol. 16, no. 2, p. 369, 1977.
- [93] T. Yao, Y. Makita, and S. Maekawa, “Molecular beam epitaxial growth of lowresistivity ZnSe films,” *Applied Physics Letters*, vol. 35, no. 2, pp. 97–98, 1979.

- [94] R. M. Park, H. A. Mar, and N. M. Salansky, “Molecular beam epitaxy growth of ZnSe on (100)GaAs by compound source and separate source evaporation: A comparative study,” *Journal of Vacuum Science and Technology B: Microelectronics and Nanometer Structures*, vol. 3, no. 2, pp. 676–680, 1985.
- [95] D. Abou-Ras, G. Kostorz, A. Romeo, D. Rudmann, and A. N. Tiwari, “Structural and chemical investigations of CBD- and PVD-CdS buffer layers and interfaces in Cu(In,Ga)Se₂-based thin film solar cells,” *Thin Solid Films*, vol. 480, no. 0, pp. 118–123, 2005.
- [96] A. Deneuve, D. B. Tanner, R. M. Park, and P. H. Holloway, “Determination of the carrier concentration of doped ZnSe from infrared measurements,” *Journal of Vacuum Science and Technology A: Vacuum, Surfaces, and Films*, vol. 9, no. 3, pp. 949–953, 1991.
- [97] G. N. Ivanova, D. D. Nedeoglo, N. D. Negeoglo, V. P. Sirkeli, I. M. Tiginyanu, and V. V. Ursaki, “Interaction of intrinsic defects with impurities in Al doped ZnSe single crystals,” *Journal of Applied Physics*, vol. 101, no. 6, p. 063543, 2007.
- [98] Y. C. Lin, C. H. Chiu, W. C. Fan, C. H. Chia, S. L. Yang, D. S. Chuu, M. C. Lee, W. K. Chen, W. H. Chang, and W. C. Chou, “Raman scattering of longitudinal-optical-phonon-plasmon coupling in Cl-doped ZnSe under high pressure,” *Journal of Applied Physics*, vol. 102, no. 12, p. 123510, 2007.
- [99] M. Aven and B. Segall, “Carrier mobility and shallow impurity states in ZnSe and ZnTe,” *Physical Review*, vol. 130, no. 1, pp. 81–91, 1963.
- [100] D. Noda, T. Aoki, Y. Nakanishi, and Y. Hatanaka, “Preparation of heavily n-type ZnSe doped by iodine in remote plasma enhanced metal organic chemical vapor deposition,” *Japanese Journal of Applied Physics*, vol. 36, p. 6302, 1997.

- [101] D. C. Oh, T. Takai, I. H. Im, S. H. Park, T. Hanada, T. Yao, J. S. Song, J. H. Chang, H. Makino, C. S. Han, and K. H. Koo, “Optical properties and electrical properties of heavily Al-doped ZnSe layers,” *Journal of Vacuum Science and Technology A: Vacuum, Surfaces, and Films*, vol. 26, no. 2, pp. 259–264, 2008.
- [102] B. Jobst, D. Hommel, U. Lunz, T. Gerhard, and G. Landwehr, “ E_0 , bandgap energy, and lattice constant of ternary $\text{Zn}_{1-x}\text{Mg}_x\text{Se}$ as functions of composition,” *Applied Physics Letters*, vol. 69, no. 1, pp. 97–99, 1996.
- [103] R. Inoue, M. Kitagawa, T. Nishigaki, K. Ichino, H. Kobayashi, M. Ohishi, and H. Saito, “Optical band gap of $\text{Zn}_x\text{Mg}_{1-x}\text{S}$ thin films with composition x between 0.14 and 1.0,” *Journal of Crystal Growth*, vol. 184185, no. 0, pp. 1076–1080, 1998.
- [104] F. El Haj Hassan, A. Bleybel, A. Hijazi, A. Alaeddine, B. Beydoun, and M. Zoaeter, “Structural and electronic properties of $\text{Zn}_{1-x}\text{Mg}_x\text{S}_y\text{Se}_{1-y}$ alloys,” *Materials Letters*, vol. 61, no. 45, pp. 1178–1182, 2007.
- [105] R. L. Anderson, “Experiments on Ge-GaAs heterojunctions,” *Solid State Electronics*, vol. 5, no. 5, pp. 341–351, 1962.
- [106] A. Franciosi and C. Van de Walle, “Heterojunction band offset engineering,” *Surface Science Reports*, vol. 25, no. 1-4, p. 1, 1996.
- [107] Y. C. Ruan and W. Y. Ching, “An effective dipole theory for band lineups in semiconductor heterojunctions,” *Journal of Applied Physics*, vol. 62, no. 7, pp. 2885–2897, 1987.
- [108] A. Franciosi, L. Sorba, G. Bratina, and G. Biasiol, “Modification of heterojunction band offsets at III–V/IV/III–V interfaces,” vol. 11, pp. 1628–1637, AVS.
- [109] C. G. Van de Walle and J. Neugebauer, “Universal alignment of hydrogen

levels in semiconductors, insulators and solutions,” *Nature*, vol. 423, no. 6940, pp. 626–628, 2003.

- [110] S. Limpijumnong, L. Gordon, M. Miao, A. Janotti, and C. G. Van de Walle, “Alternative sources of p-type conduction in acceptor-doped ZnO,” *Applied Physics Letters*, vol. 97, no. 7, p. 072112, 2010.
- [111] E. A. Kraut, R. W. Grant, J. R. Waldrop, and S. P. Kowalczyk, “Precise determination of the valence-band edge in x-ray photoemission spectra: Application to measurement of semiconductor interface potentials,” *Physical Review Letters*, vol. 44, no. 24, pp. 1620–1623, 1980.
- [112] E. A. Kraut, R. W. Grant, J. R. Waldrop, and S. P. Kowalczyk, “Semiconductor core-level to valence-band maximum binding-energy differences: Precise determination by x-ray photoelectron-spectroscopy,” *Physical Review B*, vol. 28, no. 4, pp. 1965–1977, 1983.
- [113] D. A. Shirley, “High-resolution x-ray photoemission spectrum of valence bands of gold,” *Physical Review B*, vol. 5, no. 12, p. 4709, 1972.
- [114] D. Briggs and P. Seah, *Practical surface analysis: Auger and X-ray photoelectron spectroscopy*. Wiley, 1990.
- [115] G. Kresse and J. Hafner, “Ab-initio molecular-dynamics simulation of the liquid-metal amorphous-semiconductor transition in germanium,” *Phys. Rev. B*, vol. 49, no. 20, p. 14251, 1994.
- [116] G. Kresse and J. Furthmüller, “Efficiency of ab-initio total energy calculations for metals and semiconductors using a plane-wave basis set,” *Computational Materials Science*, vol. 6, no. 1, pp. 15–50, 1996.
- [117] P. E. Blochl, “Projector augmented-wave method,” *Physical Review B*, vol. 50, no. 24, p. 17953, 1994.

- [118] A. V. Krukau, O. A. Vydrov, A. F. Izmaylov, and G. E. Scuseria, “Influence of the exchange screening parameter on the performance of screened hybrid functionals,” *Journal of Chemical Physics*, vol. 125, no. 22, p. 5, 2006.
- [119] J. P. Perdew, K. Burke, and M. Ernzerhof, “Generalized gradient approximation made simple,” *Physical Review Letters*, vol. 77, no. 18, pp. 3865–3868, 1996.
- [120] J. P. Allen, D. O. Scanlon, and G. W. Watson, “Electronic structure of mixed-valence silver oxide AgO from hybrid density-functional theory,” *Physical Review B*, vol. 81, no. 16, 2010.
- [121] M. Burbano, D. O. Scanlon, and G. W. Watson, “Sources of conductivity and doping limits in CdO from hybrid density functional theory,” *Journal of the American Chemical Society*, vol. 133, no. 38, pp. 15065–15072, 2011.
- [122] A. B. Kehoe, D. O. Scanlon, and G. W. Watson, “Nature of the band gap of Tl_2O_3 ,” *Physical Review B*, vol. 83, no. 23, 2011.
- [123] D. O. Scanlon, A. Walsh, and G. W. Watson, “Understanding the p-type conduction properties of the transparent conducting oxide CuBO_2 : A density functional theory analysis,” *Chemistry of Materials*, vol. 21, no. 19, pp. 4568–4576, 2009.
- [124] D. O. Scanlon and G. W. Watson, “Conductivity limits in CuAlO_2 from screened-hybrid density functional theory,” *Journal of Physical Chemistry Letters*, vol. 1, no. 21, pp. 3195–3199, 2010.
- [125] D. O. Scanlon and G. W. Watson, “Band gap anomalies of the $(\text{ZnM}_2\text{O}_4)\text{-O-III}$ ($\text{M-III} = \text{Co, Rh, Ir}$) spinels,” *Physical Chemistry Chemical Physics*, vol. 13, no. 20, pp. 9667–9675, 2011.

- [126] J. J. Yeh and I. Lindau, “Atomic subshell photoionization cross sections and asymmetry parameters: $1 < z < 103$,” *Atomic Data and Nuclear Data Tables*, vol. 32, no. 1, pp. 1–155, 1985.
- [127] R. Stangl, M. Kriegel, S. Kirste, M. Schmidt, and W. Fuhs, “AFORS-HET, a numerical PC program for simulation of heterojunction solar cells, version 1.2 (open-source on demand), to be distributed for public use.,” 2005.
- [128] S. Hava, “Surface effects and grain-boundary domination in thin-film Zn_3P_2 photoconductivity,” *Journal of Applied Physics*, vol. 59, no. 12, pp. 4097–4102, 1986.
- [129] H. Okada, S. Shikata, and I. Hayashi, “Electrical characteristics and reliability of Pt/Ti/Pt/Au ohmic contacts to p-type GaAs,” *Japanese Journal of Applied Physics*, vol. 30, no. 4A, p. L558, 1991.
- [130] A. G. Baca, F. Ren, J. C. Zolper, R. D. Briggs, and S. J. Pearton, “A survey of ohmic contacts to III-V compound semiconductors,” *Thin Solid Films*, vol. 308309, no. 0, pp. 599–606, 1997.
- [131] T. Miyajima, H. Okuyama, and K. Akimoto, “Ti/Pt/Au ohmic contacts to n-type ZnSe,” *Japanese Journal of Applied Physics*, vol. 31, no. 12B, p. L1743, 1992.
- [132] O. Vazquez-Mena, J. P. Bosco, O. Ergen, H. I. Rasool, A. Fathalizadeh, M. Tosun, M. Crommie, A. Javey, H. Atwater, and A. Zettl, “Performance enhancement using the field-effect in a graphene-zinc phosphide junction solar cell,” *In revision, Nanoletters*, 2014.
- [133] J. M. Pawlikowski, “Absorption edge of Zn_3P_2 ,” *Physical Review B*, vol. 26, no. 8, p. 4711, 1982.

APPENDIX A

A.1 Comparison of potential heteroepitaxial templates

Figure A.1 displays the thermal expansivity for a large number of elemental and semiconductor crystals versus their calculated lattice mismatch with tetragonal Zn_3P_2 .

A.2 E_g and χ calculations for $\text{Zn}_x\text{Mg}_{1-x}\text{S}_y\text{Se}_{1-y}$ quaternary alloys

The lattice parameter and band gap over the entire range of the $\text{Zn}_x\text{Mg}_{1-x}\text{S}_y\text{Se}_{1-y}$ quaternary alloy was calculated by linearly extrapolating the values of the four

linearly between ZnS and ZnSe, the electron affinity of the entire system can be determined from the calculated band gap and the ZnS and ZnSe electron affinities.

A.3 Calculated DFT band structures for II-VI semiconductors

Figure A.2 displays the band structures calculated by Density Functional Theory for zinc-blende ZnS, zinc-blende ZnSe, wurtzite-CdS, and wurtzite-ZnO.¹⁹ The band structures are courtesy of Dr. David Scanlon of University College, London. These band structures were used to determine the partial effective density of states (PEDOS) for each material which was then employed to calculate a total valence-band density of states (VB-DOS).

In addition to calculating the VB-DOS, the band structure of Zn₃P₂ was used to determine the effective masses along each of the principal axes in the Zn₃P₂ tetragonal lattice. The values are summarized in Table A.1. These values were later used to calculate an effective hole mass for Zn₃P₂ (found in Table A.2) that was later used in the effective dipole model calculations. The effective mass was calculated using the expression:⁵

$$m_i^*/m_o = [(m_{\Gamma \rightarrow Z})(m_{\Gamma \rightarrow X})(m_{\Gamma \rightarrow M})]_{\nu_i}^{1/3}. \quad (\text{A.3})$$

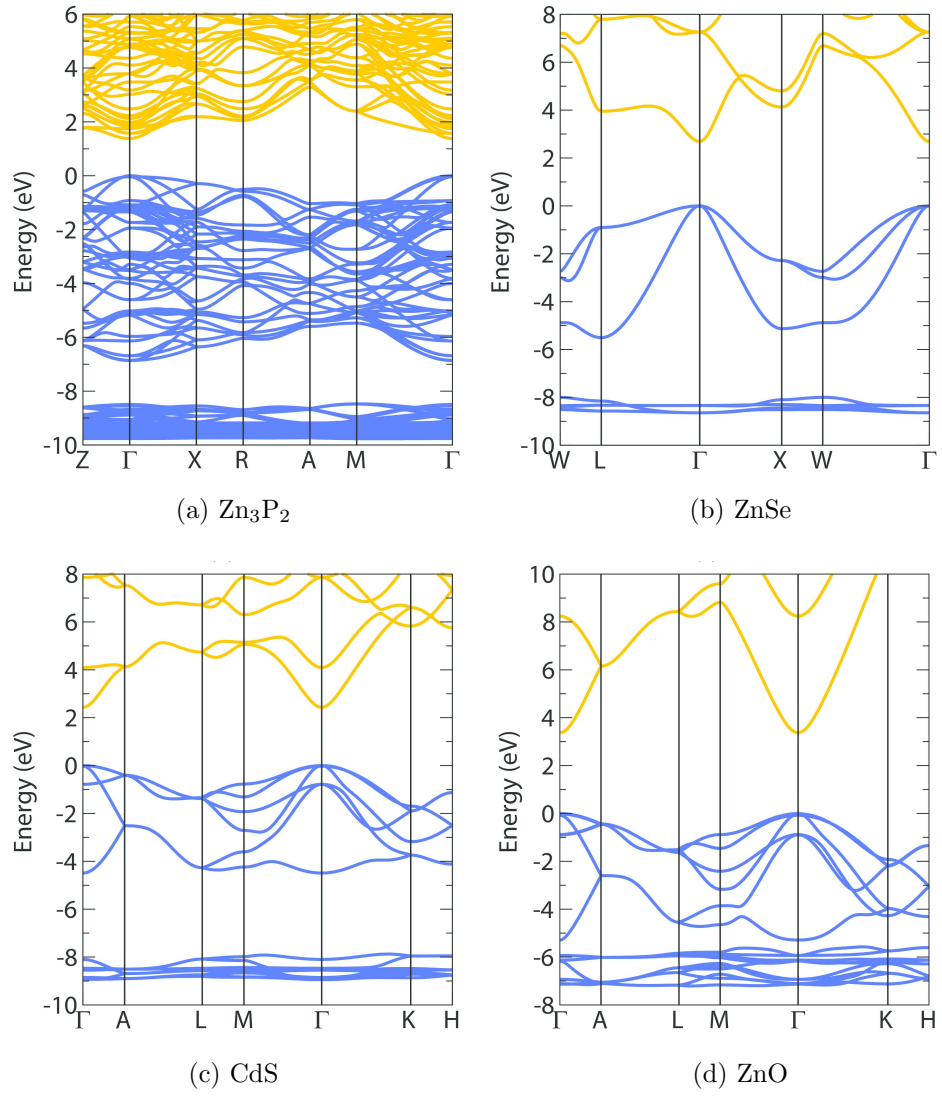


Figure A.2: DFT calculated band diagrams for Zn_3P_2 and II-VI compounds

Table A.1: Calculated effective mass values (m_h/m_o) for the three uppermost valence bands of Zn_3P_2 as determined by parabolic fitting of the Zn_3P_2 band diagram. ν_1 corresponds to the highest energy, or heavy hole, valence band.¹⁹

Principal Axis	ν_1	ν_2	ν_3
$\Gamma \longrightarrow \text{Z}$	0.255	0.760	0.761
$\Gamma \longrightarrow \text{X}$	0.407	3.770	0.109
$\Gamma \longrightarrow \text{M}$	0.415	0.410	0.141

Table A.2: The relevant band properties for Zn_3P_2 used in the effective dipole calculation. The Zn_3P_2 hole effective masses were calculated from the DFT effective masses in Table A.1.

Property	Zn_3P_2	Reference
ϵ	$11\epsilon_o$	[20]
Δ_{CF}	0.04 eV	[133]
Δ_{SO}	0.11 eV	[133]
m_1^*/m_o	0.351	
m_2^*/m_o	1.055	
m_3^*/m_o	0.2270	

A.4 X-ray photoionization cross sections for group II, V, and VI elements

The PEDOS calculated for each atom of a given compound were weighted by the x-ray photoionization cross section of that element before summation in order to obtain a total VB-DOS for that particular compound. Table A.3 lists the photoionization cross sections of the group II, V, and II atoms of interest as a function of the orbital.¹²⁶ These cross sections are for an x-ray energy of 1486.6 eV which is representative of the Al K α emission used in all experiments described in this work.

Table A.3: X-ray photoionization cross sections of group II, V, and VI atoms for 1486.6 eV (Al K α) x-rays. All values are reported in units of cm².

Element	Atomic number (Z)	s	p	d	f
O	8	1.9×10^{-3}	2.4×10^{-4}	0	0
P	15	1.4×10^{-3}	5.0×10^{-4}	0	0
S	16	1.9×10^{-3}	1.0×10^{-3}	0	0
Zn	30	7.8×10^{-4}	3.7×10^{-2}	1.2×10^{-2}	0
Se	34	2.1×10^{-3}	2.6×10^{-3}	3.1×10^{-2}	0
Cd	48	7.0×10^{-4}	3.0×10^{-2}	2.6×10^{-2}	0

A.5 XPS data for II-VI/ Zn_3P_2 heterojunctions

The following tables provide all of the collected binding energy peak positions for group V and group VI anions as a function of II-VI film thickness for the II-VI/ Zn_3P_2 heterointerfaces studied.

Table A.4: A complete list of P $2p^{3/2}$ and S $2p^{3/2}$ binding energies for all ZnS/Zn₃P₂ samples studied. Calculated $E_{\text{CL}} - E_{\text{VBM}}$ for bulk samples and $\Delta E_{\text{CL},i}$ and ΔE_{V} for heterojunction samples are also included. All values are reported in eV.

Sample	P $2p^{3/2}$	S $2p^{3/2}$	$\Delta E_{\text{CL},i}$	$E_{\text{CL}} - E_{\text{VBM}}$	$\Delta E_{\text{V}}^{\dagger}$	$\Delta E_{\text{V}}^{\ddagger}$
Bulk Zn ₃ P ₂	128.17(4)	128.46(9)
Bulk Zn ₃ P ₂	128.13(6)	128.51(5)
0.6 nm ZnS/Zn ₃ P ₂	128.08(2)	161.69(2)	33.79(2)	...	-1.20	-1.01
1.0 nm ZnS/Zn ₃ P ₂	128.20(1)	161.79(3)	33.77(5)	...	-1.19	-1.15
1.4 nm ZnS/Zn ₃ P ₂	128.12(0)	161.72(3)	33.78(5)	...	-1.20	-1.12
1.8 nm ZnS/Zn ₃ P ₂	128.20(8)	161.76(2)	33.73(6)	...	-1.15	-1.18
2.2 nm ZnS/Zn ₃ P ₂	128.07(9)	161.70(6)	33.80(9)	...	-1.22	-1.15
Bulk ZnS	...	162.89(1)	...	161.07(1)
Bulk ZnS	...	162.75(7)	...	161.08(7)

[†] The heterojunction ΔE_{V} as determined by the Kraut method using Equation 5.11.

[‡] The heterojunction ΔE_{V} as determined by the direct superposition fitting.

Table A.5: A complete list of P $2p^{3/2}$ and Se $3d^{5/2}$ binding energies for all ZnSe/Zn₃P₂ samples studied. Calculated $E_{\text{VBM}} - E_{\text{F}}$ and $E_{\text{CL}} - E_{\text{VBM}}$ for bulk samples and $\Delta E_{\text{CL},i}$ and ΔE_{V} for heterojunction samples are also included. All values are reported in eV.

Sample	P $2p^{3/2}$	Se $3d^{5/2}$	$\Delta E_{\text{CL},i}$	$E_{\text{VBM}} - E_{\text{F}}$	$E_{\text{CL}} - E_{\text{VBM}}$	ΔE_{V}
Thick Zn ₃ P ₂	128.16(8)	0.09(4)	128.49(2)	...
Thick Zn ₃ P ₂	128.12(9)	0.04(1)	128.50(5)	...
v.c.-Zn ₃ P ₂	128.19(3)	0.08(8)	128.52(3)	...
0.5 nm ZnSe/Zn ₃ P ₂	128.13(7)	54.05(6)	-74.06(8)	-1.26
1.0 nm ZnSe/Zn ₃ P ₂	128.09(3)	53.99(8)	-74.08(2)	-1.25
1.5 nm ZnSe/Zn ₃ P ₂	128.20(5)	54.07(2)	-74.12(0)	-1.21
2.0 nm ZnSe/Zn ₃ P ₂	128.13(3)	54.00(4)	-74.11(6)	-1.22
3.0 nm ZnSe/Zn ₃ P ₂	128.21(3)	54.00(6)	-74.19(4)	-1.14
Thick ZnSe	...	54.74(2)	...	1.96(3)	53.20(9)	...
Thick ZnSe	...	54.57(1)	...	1.81(4)	53.18(7)	...
v.c.-ZnSe	...	60.76(7)	...	8.06(8)	53.13(0)	...

Table A.6: A complete list of P $2p^{3/2}$ and S $2p^{3/2}$ binding energies for all CdS/Zn₃P₂ samples studied. Calculated $E_{\text{VBM}} - E_{\text{F}}$ and $E_{\text{CL}} - E_{\text{VBM}}$ for bulk samples and $\Delta E_{\text{CL},i}$ and ΔE_{V} for heterojunction samples are also included. All values are reported in eV.

Sample	P $2p^{3/2}$	S $2p^{3/2}$	$\Delta E_{\text{CL},i}$	$E_{\text{VBM}} - E_{\text{F}}$	$E_{\text{CL}} - E_{\text{VBM}}$	ΔE_{V}
Thick Zn ₃ P ₂	128.16(8)	0.09(4)	128.49(2)	...
Thick Zn ₃ P ₂	128.12(9)	0.04(1)	128.50(5)	...
v.c.-Zn ₃ P ₂	128.19(3)	0.08(8)	128.52(3)	...
0.4 nm CdS/Zn ₃ P ₂	128.28(6)	161.90(5)	33.61(9)	-1.68
0.7 nm CdS/Zn ₃ P ₂	128.21(1)	161.86(8)	33.65(7)	-1.72
1.2 nm CdS/Zn ₃ P ₂	128.14(8)	161.73(2)	33.58(4)	-1.64
1.8 nm CdS/Zn ₃ P ₂	128.22(1)	161.83(4)	33.62(3)	-1.68
2.5 nm CdS/Zn ₃ P ₂	128.35(2)	161.91(3)	33.56(1)	-1.62
Thick CdS	...	162.15(0)	...	2.25(9)	160.49(1)	...
Thick CdS	...	162.16(5)	...	2.33(1)	160.43(4)	...
v.c.-CdS	...	162.27(1)	...	2.45(3)	160.41(8)	...

Table A.7: A complete list of fitted Zn $3\tilde{d}^{5/2}$ binding energies for all ZnO/Zn₃P₂ samples studied. Calculated $E_{\text{VBM}} - E_{\text{F}}$ and $E_{\text{CL}} - E_{\text{VBM}}$ for bulk samples and $\Delta E_{\text{CL},i}$ and ΔE_{V} for heterojunction samples are also included. All values are reported in eV.

Sample	Zn $3\tilde{d}^{5/2}$ (<i>phosphide</i>)	Zn $3\tilde{d}^{5/2}$ (<i>oxide</i>)	$\Delta E_{\text{CL},i}$	$E_{\text{VBM}} - E_{\text{F}}$	$E_{\text{CL}} - E_{\text{VBM}}$	ΔE_{V}
Thick Zn ₃ P ₂	9.88(8)	0.09(4)	9.99(4)	...
Thick Zn ₃ P ₂	9.84(3)	0.04(1)	10.00(2)	...
v.c.-Zn ₃ P ₂	9.91(8)	0.08(8)	10.03(0)	...
0.2 nm ZnO/Zn ₃ P ₂	9.90(2)	10.84(5)	1.14(8)	-3.55
0.4 nm ZnO/Zn ₃ P ₂	9.89(5)	10.81(6)	1.12(6)	-3.53
0.6 nm ZnO/Zn ₃ P ₂	9.97(6)	10.91(1)	1.14(0)	-3.54
0.8 nm ZnO/Zn ₃ P ₂	9.94(1)	10.88(0)	1.14(4)	-3.55
1.0 nm ZnO/Zn ₃ P ₂	9.91(2)	10.79(9)	1.09(2)	-3.50
1.4 nm ZnO/Zn ₃ P ₂	9.89(8)	10.62(7)	0.93(4)	-3.34
Thick ZnO	...	9.96(9)	...	2.75(3)	7.62(1)	...
Thick ZnO	...	9.90(5)	...	2.65(7)	7.65(3)	...
v.c.-ZnO	...	10.64(8)	...	3.51(4)	7.53(9)	...